SALT DISPERSION IN DELAWARE BAY ESTUARY

by

MARIA F. ARISTIZABAL

A dissertation submitted to the

Graduate School-New Brunswick

Rutgers, The State University of New Jersey

In partial fulfillment of the requirements

For the degree of

Doctor of Philosophy

Graduate Program in Oceanography

Written under the direction of

Robert Chant

and approved by

_____

_____

_____

_____

New Brunswick, New Jersey

OCTOBER, 2013

ABSTRACT OF THE DISSERTATION

Salt Dispersion in Delaware Bay Estuary

By MARIA F. ARISTIZABAL

Dissertation Director:

Robert Chant

Delaware Bay is a coastal plain estuary located in the east coast of the United States and provides recreation, transportation, fishery and water resources. The physical characteristics of an estuary significantly influence the function and value of these resources. For example increased salt intrusion associated with channel deepening may be a threat to potable water supplies and increase diseases to shelf-fish. It is then relevant to understand these physical characteristics and the processes that govern them. This graduate work focused on some hydrodynamic aspects of Delaware Bay, in particular, the transport of salt, stratification and the role of the cross-channel dynamics.

Numerical simulations and observations were the tools employed to develop this work. The Regional Ocean Modeling System (ROMS) was used to set up a model of the bay. The observations consisted of a mooring array in the middle reach of the bay, equipped with ADCPs and CT sensors at different depths. Additionally, four cross-channel tidal surveys were performed in the same location of the mooring array.

The results indicate that the net salt transport due to tidal flows (F_t) is of the same order of magnitude as the salt transport due to the estuarine exchange flow (F_e). Furthermore, F_t is intensified during neap periods, presenting a spring-neap variability that is opposite to previous parameterizations. We concluded that this spring-neap

variability is caused by the action of the cross-channel flows on the salinity field that enhances the tidal period variability of salinity (s_t) during neap tides, and brings the along-channel velocity and salinity out of quadrature.

The lateral flows, acting on the cross-channel salinity gradient, tend to stratify the water column on the flood and destratify the water column during the ebb. This tidal period variability competes, and often overcomes, the along-channel straining. Consequently stratification in Delaware Bay is often enhanced during the flood and reduced during the ebb, contrary to the classic model of tidal straining.

This demonstrates that the cross-channel dynamics has an important influence on the salt transport and stratification in this system and may have other important consequences on processes such as sediment transport.

Acknowledgements

I am deeply thankful to my advisor Robert Chant for supporting me, believing in me and for always putting a smile on my face.

I am also very thankful to John Wilkin for all his attention, willingness to respond all my questions and for all his personal advise.

I would also like to express my gratitude to Dove Guo and Joe Jurisa for their friendship and their unconditional help with the fieldwork, to Eli Hunter for being always so kind, helpful and efficient and to Jack McSweeney for her friendship and cheerful spirit.

I would like to show my appreciation for Josh Kohut and Parker MacCready for kindly accepting to be part of my thesis committee.

I am grateful to Rocky Geyer and, again, Parker MacCready for inviting me to the Friday Harbor class, 2012, and embrace me as one of their students.

Finally I would like to acknowledge all the faculty and stuff in IMCS that made of my stay in this institute a very pleasant experience.

Dedication

I dedicate this work to my mother, who has unconditionally helped me through my life and has encouraged me to follow my bliss.

To my husband, who believed I could pursue this Ph.D program and has supported me in all my endeavors.

To my children, for the happiness they bring to my life everyday and for helping me to keep my perspective.

Table of Contents

Chapter 1

Introduction

Estuaries are one of the most productive marine ecosystems on earth and about 60% of human population lives close to estuaries and coast. They also provide people with recreation, transportation and water resources. Most estuaries are formed by the confluence of rivers and the costal ocean, so they are characterized by a strong longitudinal salinity gradient that has important consequences for the hydrodynamics of these systems. This longitudinal salinity gradient has also practical consequences in that it determines where the water is available for thermoelectric, industrial and agricultural uses among others. In particular, the salt line that is how far upstream the salt coming from the ocean can penetrate, regulates the position of water intake for human consumption. The plants and animals that live in estuaries have also adapted to tolerate certain range of salinities, and any disruption to the salinity field can affect the productivity of a number of species. It is then quite relevant to understand what are the main controls of salinity gradients in estuaries.

In addition, these systems have been significantly impacted by human activities such as deforestation, discharge of contaminants and wastewater, all these affecting water quality. Through the clean water act in the 1970s, the water quality of many estuaries in the USA have considerably improved, but the loss of forest to urban development, relic contaminants and eutrophication are still issues. Dredging of the main navigational channel in the waterway is also a standard practice, but it can disrupt the habitat of benthic species and affect the salt and sediment balance, which can potentially alter the supply of sediments to tidal salt marshes. Coastal wetlands provide important ecosystem services such as protection against flooding, nutrient removal and carbon sequestration and are currently at risk due to dredging (Pringle and Phillips 1989),

nutrient enrichment (Deegan *et al.* 2012) and sea level rise (van Wijnen and Bakker 2001, Reed 1995 and Day *et al.* 1999).

In this graduate work, I focused on the hydrodynamics of Delaware Bay. In particular I studied the salt fluxes, the response of the salinity field to river discharge and mechanisms driving stratification in this system.

Delaware Bay is a coastal plain estuary and is one of the most important navigational channels in the east coast of the United States. Its main tributary is the Delaware River, and accounts for approximately 50% of the total fresh water discharge into the estuary, with an annual mean river discharge of 330 m^3/s. The bathymetry of this system is characterized by shallow flanks and a deep channel. The channel has multiple branches in the lower estuary/bay, and the upper reaches have been dredged since 1885 (USACE 1974). The salt intrusion has been monitored daily by U.S. Geological Survey since 1963 and is usually located between 80 and 140 km from the mouth of the bay.

Delaware Bay is a very valuable resource for the states of New Jersey, Delaware, New York and Pennsylvania. About 9 million people live in its basin, and it provides drinking water for approximately 15 million people (Adkins 2012). One of the major water uses, thermoelectric generation, accounts for about 66% of the total water withdrawal in the basin, followed by public water supply (17%), industrial (8%) and hydroelectric (5%) uses. Delaware Bay also provides habitat for the largest breeding population of horseshoe crabs in the world, which attracts tens of thousands of migratory birds every spring (Niles *et al.* 2012). In addition, the bay sustains eastern oysters and blue crab fishery industries that were valued about 3.5 and 14 million dollars respectively during 2010 (Adkins 2012).

1.1 Previous studies in Delaware Bay

There have been a number of studies in Delaware Bay that have tried to understand the salt structure and circulation in this system. One of the first studies about physical aspects of Delaware Bay was the work by Paulson (1970). He solved the one-dimensional,

tidal average diffusion equation for steady state and assumed that the along channel dispersion coefficient K_H was constant with along-channel distance. Using an hourly data record of specific conductance at five different stations and different river discharges at Trenton, he concluded that K_H had to increase with river discharge in the upper reach of Delaware Bay in order to reproduce the salinity data.

A later study by Garvine *et al.* (1992) used a long term salinity data that expanded a wide range of river discharges and found that the mean axial salinity distribution varies linearly in most of the extent of the estuary. They also found that the response of the along-channel salinity structure to river discharge was very weak. For instance, they estimated that the response of the 13.7 isohaline to a doubling of the annual mean flow at Trenton was only 7.7 km oceanward. They concluded that for the salt field to be so insensitive, the along-channel dispersion coefficient had to increase with river discharge, as it was suggested by Paulson (1970). They proposed that there must exist a buffering mechanism in Delaware Bay, in such a way that the oceanward advective salt flux is almost balanced regardless of the river flow.

Wong (1994), Wong (1995) and Wong and Moses-Hall (1998) suggested that the cross-channel bathymetry variations have an important effect on the subtidal circulation and salinity structure. They found that the gravitational circulation was characterized by a fresher layer of water directed oceanward on top of a saltier layer of water directed landward over the main channel, consistent with the classical view of exchange flow, but was laterally sheared over the flanks.

In addition to observational studies, there have been a number of attempts to model the salinity field in Delaware Bay. McCarthy (1991) developed a two dimensional model, but it failed to predict the along-channel structure of salinity because the salt field intruded much further upstream and was twice as responsive to changes in river discharge than observations. Galperin and Mellor (1990) developed a three dimensional model that reproduced the overall spatial structure of the salinity and velocity fields, but the along-channel salinity structure was three times more responsive to river discharge than the observations by Garvine *et al.* (1992).

Later, Whitney and Garvine (2006) modeled the Delaware estuary and river outflow

using a three dimensional model and obtained a salinity field that responded according with observations in the lower bay but responded more weakly in the upper estuary. Finally, a two dimensional numerical model developed by MacCready (2007) overpredicts the location of the head of the salt as well as the response of the salt intrusion length to river input in Delaware Bay, yet performed much more favorably in both San Francisco Bay and the Hudson River Estuary.

All these previous studies have provided a hint about the physical characteristics of this system, yet they suggest that there is much more that we need to know. For example, the failure of the different theoretical and numerical models to predict the the salt intrusion length and the response of the salt field to river discharge suggest that there are some physical processes that have been neglected in these models but are quite important in Delaware Bay. Additionally, most of the observational studies have consisted of long-term surface salinity data sets along the main axis and cross-channel tidal surveys at the lower bay. These data, even though quite valuable, are of limited scope since they do not provide us with velocity measurements, and therefore, can not be used to get insights into the dynamics of the system. In addition, the data lacks the spatial and temporal resolution that would enable us to capture the tidal and spring-neap variability in quantities, such as stratification and pressure gradients, that are also important to quantify the bay's dynamics.

It is then the main objective of this work to contribute to a more complete picture of the physical characteristics of the bay. In particular, we described the spatial structure and time variability of the subtidal flows, subtidal salinity field and salt fluxes in the bay. We identified a mechanism that drives the salt flux at tidal time scales in this system and provided a scaling for the along-channel dispersion coefficient. We diagnosed the cross-channel dynamics and their effect on the tidal variability of stratification. Lastly, we gave insights into the reasons why the along-channel salt field in Delaware Bay is relatively insensitive to changes in river discharge. In order to develop this work, we set up a 3D numerical model of the bay using Regional Ocean Modeling System (ROMS), deployed moored ADCP and CT sensors, and performed shipboard surveys in the middle reach of Delaware Bay.

1.2 Physics of estuaries

1.2.1 Subtidal along-channel momentum and salinity balance

The underlying physics behind the response of an estuary to external forcing, e.g. changes in river discharge, is contained in the momentum balance equations. Pritchard (1956) first proposed an along-channel momentum balance at subtidal time scale that explains the gravitational circulation in estuaries. This momentum balance consists of an along-channel pressure gradient, divided into a barotropic part and a baroclinic part, created by density differences between the fresh water input and oceanic waters, and friction produced by the shear in the tidally average velocity field u. If u is divided into a depth average and depth dependent part: $u = \bar{u} + u'$, where $\bar{u} = Q/A$, Q is river discharge and A is the cross-sectional area, then the along-channel momentum balance is expressed as:

$$0 = -g\frac{\partial \eta}{\partial x} + g\beta\frac{\partial \bar{s}}{\partial x}z + K_M\frac{\partial^2 u'}{\partial z^2}, \tag{1.1}$$

where K_M is the vertical eddy viscosity, β is the haline contraction coefficient, g is the gravitational acceleration and $\partial\bar{s}/\partial x$ is the along-channel gradient of the depth average salinity, which is assumed to be known. Integrating Eq. (1.1) twice with respect to z, Hansen and Rattray (1965) provided an analytical expression for the subtidal along-channel velocity for a rectangular channel of constant depth H and width B:

$$u = \bar{u}\left(\frac{3}{2} - \frac{3}{2}\zeta^2\right) + u_E(1 - 9\zeta^2 - 8\zeta^3), \tag{1.2}$$

$$\zeta = \frac{z}{H}, \qquad u_E = \frac{g\beta\frac{\partial \bar{s}}{\partial x}H^3}{48K_M}, \tag{1.3}$$

where u_E is the scale of the estuarine exchange flow, ζ is a non-dimensional parameter for depth and H is the total depth of the water column.

Pritchard (1954) also proposed the main salt balance at subtidal time scales, which is given by:

$$\frac{\partial s}{\partial t} + \frac{\partial (us)}{\partial x} + \frac{\partial (ws)}{\partial z} = \frac{\partial (K_H\frac{\partial s}{\partial x})}{\partial x} + K_s\frac{\partial^2 s}{\partial z^2}, \tag{1.4}$$

where s is the tidally average salinity, u and w are the tidally average along-channel and vertical velocity. K_s is the vertical eddy diffusivity and K_H is the along-channel

diffusivity. If s is divided into a depth average and depth dependent part: $s = \bar{s} + s'$, and Eq. 1.4 is depth averaged, we obtain an expression for the evolution of the depth average salinity field $\bar{s}$:

$$\frac{\partial \bar{s}}{\partial t} + \frac{\partial(\bar{u}\bar{s})}{\partial x} + \frac{\partial \overline{u's'}}{\partial x} = \frac{\partial(K_H \frac{\partial \bar{s}}{\partial x})}{\partial x}. \tag{1.5}$$

We can also obtain an equivalent equation for s', but Pritchard (1954) stated, for partially mixed and well mixed estuaries, that at subtidal time scales the leading order balance for s' is between the along-channel advection of salinity by the exchange flow, which acts to maintain stratification, and vertical mixing which acts to destroy it:

$$u' \frac{\partial \bar{s}}{\partial x} \simeq K_s \frac{\partial}{\partial z} \frac{\partial \bar{s}'}{\partial z}. \tag{1.6}$$

A solution for s' is found by directly integrating Eq. 1.6 and using the solution for the along-channel subtidal flow u (Eq. 1.3):

$$s' = \frac{H^2}{K_s} \frac{\partial \bar{s}}{\partial x} \left(\bar{u} \left(-\frac{7}{120} + 14\zeta^2 - \frac{1}{8}\zeta^4 \right) + u_E \left(-\frac{1}{12} + \frac{1}{2}\zeta^2 - \frac{3}{4}\zeta^4 - \frac{2}{5}\zeta^5 \right) \right). \tag{1.7}$$

More recently, MacCready (2004) developed a similar set of equations as Hansen and Rattray, but he extended the model by allowing along-channel variations in the width and depth of the channel and in the vertical mixing and along-channel dispersion parameters. In a subsequent work, MacCready (2007) further generalized his model by including a time-dependent salt flux and by using parameterizations for vertical mixing and along-channel dispersion, in terms of channel parameters (e.g. channel depth), and state variables (e.g. tidally averaged stratification).

All these previous studies have been based on the subtidal classical momentum balance of Pritchard (1952). The other terms in the subtidal momentum equations have been neglected, with the implicit argument that they are several orders of magnitude smaller than the pressure gradient and the vertical stress divergence at subtidal time scales. The reason for the wide use of this momentum balance is that it seems to work fairly well for estuaries such as the James River (Pritchard 1952), the Mersey Estuary (Oey 1984) and the Hudson River (Geyer *et al.* 2000; MacCready 2007; Ralston *et al.* 2008).

More recently, some researches have questioned if this subtidal classical momentum balance actually holds in real estuaries. An idealized modeling study by Lerczak and Geyer (2004), in a straight channel with parabolic bathymetry, showed that in the tidal-averaged, along-channel momentum balance, the lateral advection term can be as large as the along-channel pressure gradient. Therefore, the lateral advection term is a driving mechanism for the along-channel gravitational circulation. Furthermore, Scully *et al.* (2009a) developed a 3D numerical simulation of the Hudson River Estuary and found very similar results to Lerczak and Geyer (2004): the lateral advection term has a leading order contribution on the subtidal along-channel momentum balance. So far there has not been an observational study that confirms the importance of the advection terms in the subtidal momentum balance. This remains a topic of active research in estuarine physics.

1.2.2 Along-channel salt fluxes

If we integrate Eq. 1.5 from an arbitrary location in the estuary to the head of the salt, it is obtained (MacCready 1999, 2004) that the time rate of change of the salt content in that portion of the estuary is controlled by three mechanisms:

$$\frac{d}{dt}\int \bar{s}dx = \underbrace{-\bar{u}\bar{s}}_{\text{(i)}} + \underbrace{(-\overline{u's'})}_{\text{(ii)}} + \underbrace{K_H\frac{\partial \bar{s}}{\partial x}}_{\text{(iii)}}. \tag{1.8}$$

The first mechanism,(i), is the advective salt flux that brings salt out of the estuary and is driven by river discharge. The other two mechanisms bring salt into the system and consist of: (ii) the steady shear dispersion, controlled by the estuarine exchange flow, and (iii)the tidal oscillatory salt flux that is driven by the tidal flows.

Hansen and Rattray (1965) solved Eq. 1.8 for the steady state case and applied the approximation $\bar{u} \ll u_E$. They assumed a functional form for the along-channel dispersion coefficient, such that, it increased linearly seaward. Under this approach, the increase of the tidal salt flux towards the mouth is balanced by the oceanward salt flux by river output. There is no observational evidence that shows that K_H has such functional dependence in real systems. In this solution, the along-channel gradient of

$\bar{s}$ is constant and therefore the exchange flow, stratification, and salt flux due to the exchange flow are constant too, in the middle portion of the estuary. Chatwin (1976) also solved the steady state case of Eq. 1.8 but assumed $K_H = 0$, which corresponds to systems where the salt fluxes are dominated by the exchange flow. In this case, the along-channel gradient of $\bar{s}$, the exchange flow and stratification increase towards the mouth. Another possible solution to Eq. 1.8 is one in which $s' = 0$, which conforms with systems that are vertically well-mixed. In this instance, the salt flux due to the exchange flow is zero, $-\overline{u's'}$=0, and the solution of $\bar{s}$ is an exponential function of the along-channel distance, with increasing values towards the mouth (MacCready and Geyer 2010). Finally, MacCready (2004) solved Eq. 1.8 numerically and allowed variations in the width and depth of the channel. With this approach, he easily introduced parameterizations for the mixing coefficients, K_M and K_S, and for the along-channel dispersion coefficient K_H.

In systems where the dominant salt flux mechanism is steady shear dispersion (Chatwin's solution) and assuming $\bar{u} \ll u_E$, a scaling for the salt intrusion length is given by (Monismith *et al.* 2002; Ralston *et al.* 2008):

$$L \propto \frac{(\beta g S_{oc})^{2/3} A^{1/3} H^{5/3}}{(a_0 C_d Sc^{-1/3}) Q^{1/3} U_t}, \tag{1.9}$$

where S_{oc} is oceanic salinity, Q is river discharge and U_t is amplitude of the tidal velocity. $(a_0 C_d Sc^{-1/3})$ comes from a vertical mixing parametrization where a_0 is a tuning coefficient, C_d is a drag coefficient and Sc is a Schmidt number defined as the ration between eddy viscosity and eddy diffusivity. This scaling states that the salt intrusion length is proportional to $Q^{-1/3}$. This proportionality has served as a reference frame for the response of the salinity field to river discharge for a number of systems.

Lerczak *et al.* (2006) calculated the area integrated salt fluxes in the Hudson River using observations. It was concluded that the dominant mechanism of downgradient salt flux was the steady shear dispersion, being an order of magnitude larger than the tidal oscillatory salt flux. Other studies have confirmed, that the response of the salt intrusion length to river discharge in the Hudson River, approximately follows the $Q^{-1/3}$ dependence (Abood 1974; Ralston *et al.* 2008). This is consistent with the theoretical

prediction for exchange dominated systems.

However, there are systems where the tidal oscillatory salt flux represents a significant portion of the total downgradient salt fluxes (San Francisco Bay (Conomos 1979), Mersey Estuary (Oey 1984), Merrimack River (Chen *et al.* 2012)). It is then very relevant to understand the mechanisms that control salt fluxes at tidal time scales. Among these mechanisms is the oscillatory shear dispersion (Fisher *et al.* (1979)), where a vertical or cross-channel shear in an oscillatory flow differentially advects fluid parcels that are subsequently dispersed through vertical or cross-channel mixing. The magnitude of the dispersion depends on the relation between the mixing time scale and the period of the oscillatory motion. For example, shear dispersion due to tidal flows is maximum when the mixing time is of the order of a tidal cycle and is negligible when the mixing time is much larger than the tidal period.

A different mechanism for tidal dispersion was proposed by Zimmerman (1986). He suggested that the large along-channel dispersion observed inside estuaries was the result of the complex bathymetry inducing highly irregular velocity fields and, therefore, producing greatly variable residual flows. Under this mechanism, Zimmerman says, a parameterization for a dispersion coefficient K_H is difficult to attempt. Nonetheless, Banas *et al.* (2004) hypothesized that $K_H = c_k U_T B$, where c_k is a proportionality constant, U_T is the root mean square of the tidal velocity and B is the channel width. Physically, this parameterization may be interpreted as a dispersion process that is carried out by residual eddies with amplitude of a fraction of the residual currents: $c_k U_T$, and with a maximum length equal to the width of the channel B. Later, MacCready (2007) adopted the same parameterization as Banas *et al.* (2004) but included the tidal excursion length scale as a possible limiting factor for the size of the residual eddies: $K_H = c_k U_T min(B, L_t)$. In addition, MacCready (2007), based on the ideas of Stommel and Farmer (1952), provided an expression for K_H such that it is enhanced within a tidal excursion of the mouth due to the efficient exchange between oceanic and estuarine waters.

In general it should not be expected that the response of the salt field to river discharge conforms with $Q^{-1/3}$ dependence. In fact, the solution for the steady state case

of Eq. 1.8, predicts that the salt intrusion length shows a functional dependence of the form, $L \propto Q^{-\alpha}$, where α can range from 1, for estuaries dominated by the tidal dispersion, and 1/3 for the exchange dominated systems (MacCready and Geyer 2010). However, Monismith *et al.* (2002), in San Francisco Bay, found a dependance of salt intrusion distance with river discharge: $L \propto Q^{-1/7}$, that is ever weaker than $Q^{-1/3}$ response. They concluded that this weak response was due to the effect of stratification on suppressing vertical mixing with increasing river discharge. Ralston *et al.* (2008), using a theoretical model for salinity and estuarine circulation, found a similar dependance but concluded that the weak response was due to the bathymetry of San Francisco Bay: when river discharge increases, the salinity field is pushed downstream to sections of the bay where depth and channel cross-sectional area are greater. Greater depth enhances the the salt flux due to the subtidal flow ($\propto H^8$) and greater area decreases the advective salt flux ($\propto Q/A$).

1.2.3 Mechanisms driving stratification

Stratification in estuaries is driven by a competition between vertical mixing, induced by wind and tides, and the fresh water buoyancy input. These processes together establish the observed along-channel and vertical density gradients.

At subtidal time scales the estuarine exchange flow always promotes a stable water column, but the intensity of the stratification depends on the mixing strength controlled by the spring-neap cycle (Simpson *et al.* 1990; Chant *et al.* 2007).

On top of this background stratification, there is a tidal variability in stratification. Simpson *et al.* (1990) proposed the tidal straining mechanism to explain the periodic stratification observed in the Region Of Fresh water Influence (ROFI) of Liverpool Bay (Sharple and Simpson 1995, Rippeth *et al.* 2001). According to this mechanism, changes in stratification are caused by differential advection, due to the vertical shear of the tidal velocities, acting on the horizontal density gradient. These variations are such that the water column is well mixed at the end of flood and reaches maximum stability at the end of ebb. Semidiurnal changes in stratification have also been observed in a variety of estuaries (Jay and Smith 1990, Sharples *et al.* 1994, Nepf and Geyer 1996,

Stacey *et al.* 1999, Chant and Stoner 2001, Cheng *et al.* 2009).

Nevertheless, there have been observational studies in a number of systems that have shown that this tidal variability in stratification is not always apparent. For example, observations in a channel in northern San Francisco Bay (Lacy *et al.* 2003) showed that vertical stratification can develop during spring flood-tides. This is because the lateral density gradient,during these periods, far exceeded the longitudinal density gradient, and therefore the onset of stratification was caused by the lateral baroclinic forcing that surpassed turbulent mixing. More recently, Scully and Geyer (2012) also showed that in the upper Hudson tidal variations in stratification are not consistent with the along-channel straining mechanism. They attributed this to a competition between the along-channel and cross-channel advection of vertical salinity gradients ($\partial s/\partial z$) and tidal asymmetries in vertical mixing. These processes are likely to be negligible during well mixed conditions because as ($\partial s/\partial z$) becomes small, both longitudinal advection of stratification and cross-channel density gradients are reduced. This implies that a periodic stratification agreeing with longitudinal tidal straining is more likely to manifest during well mixed periods.

1.2.4 Cross-channel dynamics

The classical theory of estuaries focused on the along-channel momentum balance. Later on, a number of researches started to recognize the importance of the three dimensional character of estuaries. For example, Fisher (1972) and Zimmerman (1986) proposed that it was the richness of the bathymetry in estuaries that caused the large dispersion observed in these systems, although the mechanisms they introduced were of very different nature. Wong (1994, 1995), using a conceptual model and observations, concluded that cross-channel variations in depth accounted for an exchange flow that had two oceanward branches in the shallow flanks and a landward branch in deepest part of the channel, contrary to the classical two layer exchange flow.

More recently, investigators have started to recognize the importance of the cross-channel dynamics. As it has been mentioned in this introductory chapter, lateral flows can be a source of non-linearities for the along-channel momentum balance (Lerczak

and Geyer 2004; Scully *et al.* 2009a; Lacy *et al.* 2003), and a controlling mechanism for stratification at tidal time scales (Lacy *et al.* 2003; Scully and Geyer 2012). Additionally, lateral flows shape the cross-channel bathymetry, and in turn, lateral variations in depth reinforce lateral flows through differential advection (Nunes and Simpson 1985).

Several mechanism that drive cross-channel flows have been proposed in the literature. One of these mechanisms is differential advection (Nunes and Simpson 1985) that is caused by the difference in the magnitude of the depth-average along-channel flows in a cross-sectional area: currents are weaker in the shallow parts and stronger in the deepest part of the channel. Consequently, the main channel becomes saltier than the flanks during the flood tide, while the opposite occurs during the ebb tide. This creates a cross-channel density gradient that produces converging flows at the surface during the flood and diverging flows during the ebb.

Channel curvature (Chant 2002) can also generate lateral flows by inducing a cross-channel barotropic pressure gradient. This pressure gradient is created when the flow piles up against the outer wall of the channel, due to the inertia of the flow, when trying to go around the bend. Because the along-channel flow is vertically sheared, with faster currents at the surface and weaker currents at depth, the surface flow moves towards the outer wall and downwells when it reaches the boundary. Then, the bottom flow, in response to the acceleration created by the cross-channel barotropic pressure gradient, moves towards the inside of the bend. This produces a counterclockwise cell when looking in the same direction as the along-channel flow.

The effect of Coriolis can be important in estuaries, regardless of the width of the system (Chant 2010). Coriolis, acting on the along-channel flows, accelerates the fluid towards the right of the channel (in the northern hemisphere), where they accumulate. This creates a cross-channel barotropic pressure gradient that balances the depth average Coriolis $f\bar{u}$, where u is the along-channel flow. It is ultimately the shear in the along-channel flows, which create a depth-dependent Coriolis, that drives the lateral flows.

The observed behaviour of the lateral flows seem to differ from system to system depending on the dominant forces in the cross-channel momentum balance. Stratification

appears to play a significant role on the temporal variability of the flows as well. Previous observational (Chant 2002) and modeling (Lerczak and Geyer 2004) studies have shown that the cross-channel flows are enhanced during periods of low stratification and shut down during periods of high stratification. But observations in the Hudson River (Lerczak and Geyer 2004) and a modeling study in the Passaic River (Cheng *et al.* (2009)) showed that the intensity of the lateral flows was not hindered during stratified conditions. They suggested that this enhancement was due to the inclusion of a turbulence closures scheme, in contrast to the constant eddy viscosity used in the modeling study of Lerczak and Geyer (2004).

1.3 Overview of the thesis

This thesis comprises of 5 chapters. This chapter, the introduction, provides an overview of previous studies of the hydrodynamics of Delaware Bay. The chapter also discusses the classic theory of estuarine dynamics and as well as more contemporary topics in this field.

The second chapter presents the results for the area-integrated salt fluxes from numerical simulations. It introduces a driving mechanism for the tidal oscillatory salt flux, and based on this, a scaling for the along-channel dispersion coefficient is proposed. Additionally it discusses the reasons for the observed insensitivity of the salt field to river discharge in this system.

The third chapter uses the field data to investigate the cross-channel dynamics and its influence on stratification at tidal time scales, The Fourth chapter uses observations to test the numerical results in the first chapter on the area-integrated salt fluxes. In general the results are consistent with those from the 3D simulations. In addition, the along-channel dispersion coefficient is calculated and used to test the scaling proposed in chapter two.

Finally, the concluding chapter summarizes the main findings of chapters two, three and four.

Chapter 2

A Numerical Study of Salt Fluxes in Delaware Bay Estuary

2.1 Abstract

The results of a numerical study of Delaware Bay using the Regional Ocean Modeling System (ROMS) are presented. The simulations are run over a range of steady river inputs and used $M2$ and $S2$ tidal components to capture the spring-neap variability. Results provide a description of the spatial and temporal structure of the estuarine exchange flow and the salinity field as well the along-channel salt flux in the estuary. The along-channel salt flux is decomposed into an advective term associated with the river flow, a steady shear dispersion (F_e) associated with the estuarine exchange flow and a tidal oscillatory salt flux (F_t). Time series of F_e and F_t show that both are larger during neap tide than during spring. This time variability of F_t, which is contrary to existing scalings, is caused by the lateral flows that bring velocity and salinity out of quadrature and the stronger stratification during neap tide, which causes F_t to be enhanced relative to spring tide. A fit for the salt intrusion length L with river discharge Q for a number of isohalines is performed. The functional dependences of L with Q are significantly weaker than $Q^{-1/3}$ scaling. It is concluded that the response of the salt field with river discharge is due to the dependence of F_e and F_t with Q and the relative importance of F_t to the total upstream salt flux: as river discharge increases, F_e becomes the dominant mechanism. Once F_e dominates, the salt field stiffens due to a reduction of the vertical eddy viscosity with increasing Q.

2.2 Introduction

The along-channel salinity structure in estuaries is the result of two competing processes: the advection of fresh water oceanward due to river output and the flux of salt into the estuary due to processes such as steady shear dispersion and tidal oscillatory salt flux (Hansen and Rattray 1965; Zimmerman 1986; Lerczak *et al.* 2006). The vertical salinity structure is maintained by a competition between the straining of the horizontal salinity gradient, which is caused by a steady vertical shear and tidal oscillatory shear, and vertical mixing.

The along-channel and vertical salinity structure are not independent, but on the contrary, are linked to each other (Hansen and Rattray 1965). For instance, Monismith *et al.* (2002) hypothesized that as the river discharge increases, stratification increases and in turn turbulent mixing is suppressed. This allows for the salt to travel further upstream and therefore decreases the sensitivity of the salt intrusion length to river discharge.

Using the classical results of Hansen and Rattray (1965) for the exchange flow and subtidal salinity and assuming that the main mechanism responsible for the down-gradient along-channel salt fluxes is advection due to the exchange flow (steady shear dispersion), the salt intrusion length scales with river discharge as $Q^{-1/3}$ (Monismith *et al.* 2002; Ralston *et al.* 2008). This proportionality has served as a reference frame for the response of the salinity field to river discharge for a variety of systems (Oey 1984; Bowen 2000; Zahed *et al.* 2008).

This $Q^{-1/3}$ scaling is based on dynamics that only consider steady shear dispersion as the mechanism driving upstream salt flux. However, tidal oscillatory salt flux also plays a role in systems that are both weakly and strongly stratified (Chen *et al.* (2012)). While parameterizations exist for tidal oscillatory salt flux (Zimmerman 1986; Banas *et al.* 2004), they are poorly constrained (MacCready 2007). However, they are central to the classic scaling of estuarine salt field. Hansen and Rattray (1966) defined the quantity $\nu = F_t/(F_e + F_t)$, where is F_e and F_t are the salt fluxes due to the exchange flow and tidal currents respectively, and assume that F_t decreases monotonically from

the mouth to the head of salt. In reality, while one may expect increased F_t near the mouth (Stommel and Farmer 1952; MacCready 2004), there is no physical reason for such structure in the interior of the estuary. Chatwin's (1976) solution requires no F_t but rather curvature in the salinity field and an increase of F_e towards the mouth. MacCready (2007) abandoned an analytical approach to include more complex structure in both F_t and bathymetry, a methodology that we exploit here.

In Delaware Bay, Garvine *et al.* (1992) using long term salinity data, found that the response of the along-channel salinity structure to river discharge was very weak, similar to the response found by Monismith *et al.* (2002) in San Francisco Bay. For instance, they estimated that the response of the 13.7 isohaline to an increase in river discharge at Trenton of 338 m^3/s, which represents a doubling of the mean river discharge, was only 7.7 km oceanward. They suggested that for the salt field to be so insensitive to river discharge there must exist a buffering mechanism in Delaware Bay in such a way that the oceanward advective salt flux is almost balanced regardless of river flow. Whitney and Garvine (2006), based on long-term observations and numerical simulations, suggested that this buffering mechanism was due to lateral mixing generated by the down-estuary widening of the bay.

Several attempts have been made to model the salinity field in Delaware bay. Paulson (1970) solved the one-dimensional, tidally averaged diffusion equation for steady state and concluded that the along-channel dispersion coefficient had to increase with river discharge in the upper reach of Delaware Bay in order to reproduce the salinity data. Other models are the two dimensional model by McCarthy (1991) and the three dimensional model by Galperin and Mellor (1990), but both models were two to three times more responsive than the observations.

Later Whitney and Garvine (2006) modeled the Delaware estuary and river outflow using a three dimensional model and obtained a salinity field that responds according with observations in the lower bay but responds more weakly in the upper estuary. Finally, a two dimensional numerical model developed by MacCready (2007) significantly overpredicts the response of the salt intrusion length with river input in Delaware Bay yet performs much more favorably in both San Francisco Bay and the Hudson River

Estuary.

The above studies motivated us to study the salt flux mechanisms in Delaware Bay and to gain insights into the processes that control the salt intrusion length in this system. For this purpose, we developed a 3D model of the bay using the Regional Ocean Modeling System (ROMS). In this study we characterize the subtidal flow, subtidal salinity and calculate the temporal and spatial variation of salt fluxes. The temporal variation of the tidal oscillatory salt flux does not conform with the expectation from previous parameterizations, and so we discuss a mechanism responsible for its time variability and develop a scaling for the along channel dispersion coefficient due to tidal processes, K_t. Additionally, we obtain a scaling of the salt intrusion length with river discharge and explore possible causes for the insensitivity of the salt field with river input in this system. Finally, we provide insights into the causes behind the failure of the MacCready model to accurately estimate salt intrusion length in Delaware Bay.

2.3 Study site

Delaware Bay is a large coastal plain estuary located on the east coast of the U.S. Its main tributary is the Delaware River that accounts for approximately 50% of the total fresh water discharge into the estuary with a annual mean river input of $330 m^3/s$. The bay is one of the most important navigational channels in the United States. This system presents shallow flanks and a deep channel that was dredged for the first time in 1885 (USACE 1974). The mean depth of the estuary is 8 m and has a maximum depth of about 45 m. The mouth of the bay is approximately 18 km wide, then the estuary widens to a maximum of about 40 km from where it narrows in a funnel shape (Fig. 4.3). The salt intrusion has been monitored daily by U.S. Geological Survey since 1963 and it is usually located between 80 and 120 km from the mouth of the bay.

While a number of studies have suggested that Delaware Bay is a well-mixed estuary (Beardsley and Boicourt 1981; Garvine *et al.* 1992), observations made by our group and model simulations show that this system can present a vertical stratification as high as 10 psu in the main channel and is consistently well mixed in the flanks. Lateral

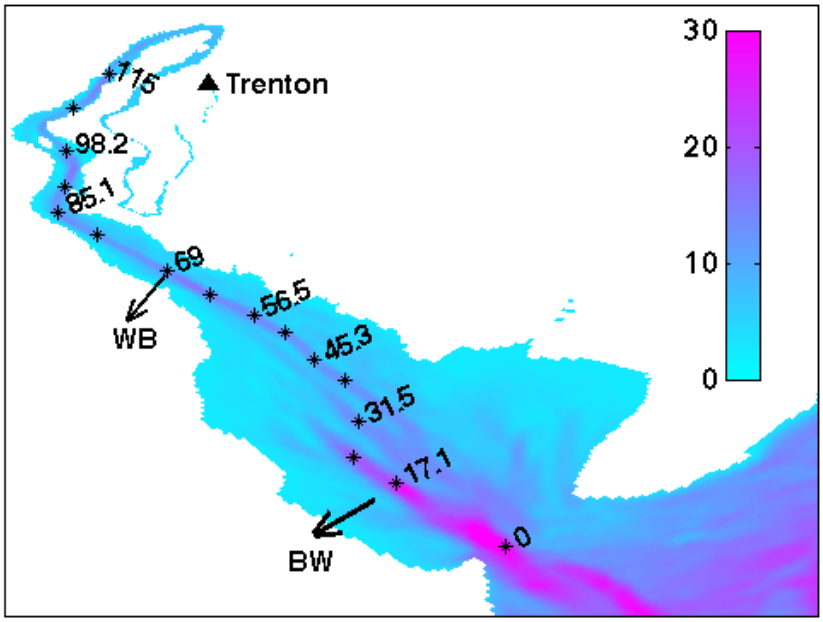

Figure 2.1: Map of Delaware Bay. The color scale represents depth in meters. The stars indicate the 16 stations defined along the estuary and the numbers next to the stars are kilometer marks along the main channel. BW and WB mark Brandywine Shoal and Woodland Beach stations. The location of Trenton (NJ) is also shown.

variations of salinity are significant in the lower bay where a high salinity inflow is concentrated in the deeper parts of the channel, while a low salinity outflow occurs in the shallow flanks (Wong 1994). Results of this paper show that the freshest water is generally located on the southern shore of the estuary consistent with a coastal current. The subtidal gravitational circulation consists of a fresher layer of water directed oceanward on top of a saltier layer of water directed landward over the main channel in agreement with a classical exchange flow, but is laterally sheared over the flanks.

2.4 Methods

2.4.1 Model setup

In this numerical study we used the Regional Ocean Modeling System (ROMS) (Shchepetkin and McWilliams 2009). The model grid has a horizontal resolution that varies

from 1.5 km near the shelf break down to several hundred meters in the upper parts of the bay. In the z direction we use 20 terrain following vertical levels. The forcing consists of M2 and S2 tidal constituents at the boundaries from the Eastcoast 2001 database of computed tidal elevation and velocity constituents (Mukai *et al.* 2002) and a constant river input imposed at the head of the tides at Trenton, New Jersey. The M2 and S2 components of tides constitute about 96% of the total tidal energy into the bay. The river input for the six different runs is: 350, 650, 1000, 1300 , 1700 and 3000 m^3/s, covering from low flow to high flow conditions, with 650 m^3/s representing the annual mean. The river input in the 3D model represents the total river input into the bay, which includes the Delaware river at Trenton that accounts for approximately 50% of the total fresh water input into the bay, and the rest 50% comes from numerous tributaries, most of them consisting of small streams. The Schuylkill River and Christina river are the second and third biggest rivers and account for about 15% and 8% of the total input to the bay respectively (Cook *et al.* 2007), both of which lie upstream of the salt intrusion. Therefore we assume that with only the river input at Trenton the model can capture the main dynamics in the bay.

We imposed a constant temperature of 5^oC in the whole domain. The turbulent closure scheme used was the Generic Length Scale mixing scheme (GLS) with K-Kl closure parameters (Warner *et al.* 2005). We run the model until it exhibited a steady spring-neap cycle in the salinity field for various locations along the estuary. Then the model was run for approximately 40 days in order to capture two spring-neap cycles.

A different application of Delaware Bay using the same set up and grid but with more realistic forcing showed significant skill (Hofmann *et al.* 2009). The purpose of this semi-idealized application is to isolate the influence of river discharge and the spring-neap cycle on controlling the salt fluxes and the salt intrusion length in this system.

2.4.2 Definition of coordinate system

We chose 16 stations along the estuary located on the deepest part of the channel (Fig. 4.3). The along-channel distance is defined as the sum of the distances between the

different stations and is consistent with the definition used by Garvine *et al.* (1992). The u, v and w components of velocity, vertical eddy viscosity and diffusivity are averaged on the middle point of each grid cell where salinity is calculated by ROMS. For the calculation of the area integrated salt fluxes, we choose 16 cross-sectional areas that follow the native grid and include the stations previously mentioned. For each cross-sectional area, the cross-channel direction is positive towards the right flank looking into the bay (NJ side) and the along-channel direction is positive landward. The along-channel velocity and salinity were low passed using a 32 hours Lanczos filter with a 70 hours half window in order to obtain the exchange flow and subtidal salinity structure.

2.4.3 Calculation of salt fluxes

We decomposed the salt fluxes into three components following Lerczak *et al.* (2006): an advective term due to river input that brings salt out of the estuary, a steady shear dispersion term which is the advection of salt due to the estuarine exchange flow and brings salt into the estuary and a tidal oscillatory salt flux which arises when the salinity and velocity fields are out of quadrature and also tends to bring salt inside the system. The area integrated, total along-channel salt flux are calculated as

$$F_s = \left\langle \int \int vs \; dA \right\rangle \tag{2.1}$$

where the brackets indicate a subtidal low pass filter. $dA = dx \; ds$ where dx and ds are determined by the size of the grid cells on the cross-sectional areas and ds, being s a vertical terrain following coordinate, is time dependent because of changes in surface height. To separate the contribution of the different processes to the salt fluxes, requires decomposing the along-channel velocity and salinity fields into three different components: a tidally and cross-sectional area average, a tidally average but cross-sectional area varying and a tidally and cross-sectional area varying. The velocity components are calculated as follows Lerczak *et al.* (2006)

$$v_0(t) = \frac{1}{A_0} \left\langle \int \int v(x,z,t) \; dA \right\rangle \tag{2.2}$$

$$v_e(x,z,t) = \frac{\langle v \; dA \rangle}{dA_0} - v_0 \tag{2.3}$$

$$v_t(x,z,t) = v - v_e - v_0 \tag{2.4}$$

where $A_0 = \left\langle \int dA \right\rangle$ and $dA_0 = \langle dA \rangle$. There is a corresponding set of equations for salinity. The physical interpretation of each term in this decomposition, for instance in the case of velocity, is: v_0 is the net outflow due to river input, v_e is the estuarine exchange flow and v_t is tidal currents. Then the total along-channel salt flux is given by

$$\begin{aligned} F_s &= \left\langle \int_{-H}^{0} \int_{0}^{W} (v_0 + v_e + v_t)(s_0 + s_e + s_t) dx dz \right\rangle \\ &= \left\langle \int_{-H}^{0} \int_{0}^{W} (v_0 s_0 + v_e s_e + v_t s_t + \text{cross terms}) dx dz \right\rangle \\ &= -Q_0 s_0 + F_e + F_t \end{aligned} \tag{2.5}$$

where $Q_0 s_0$ is the salt flux due to river outflow, F_e is the salt flux due to steady shear dispersion and F_t is the tidal oscillatory salt flux. The cross terms are approximately zero because they are largely uncorrelated by definition (MacCready 2011).

2.5 Results

2.5.1 Exchange flow and subtidal salinity structure for mean river discharge conditions $Q = 650\ m^3/s$

In the lower bay at Brandywine Shoal (17 km from the entrance of the bay and shown in Fig. 4.3 as BW), the exchange flow is vertically sheared and concentrated above the main channel and weak on the flanks during neap tides (Fig. 2.2). In contrast, during spring tides the exchange flow becomes mostly laterally sheared. In the upper estuary at Woodland Beach (69 km from the entrance of the bay and shown in Fig. 4.3 as WB) where the channel considerably narrows, vertically sheared two layer flow persists during both spring and neap tides, albeit more intense during neap tides (Fig. 2.3).

The subtidal salinity structure has similar characteristics to the residual circulation. At Brandywine Shoal, stratification is as high as 10 psu between surface and bottom above the main channel and is vertically uniform in the flanks with a maximum lateral

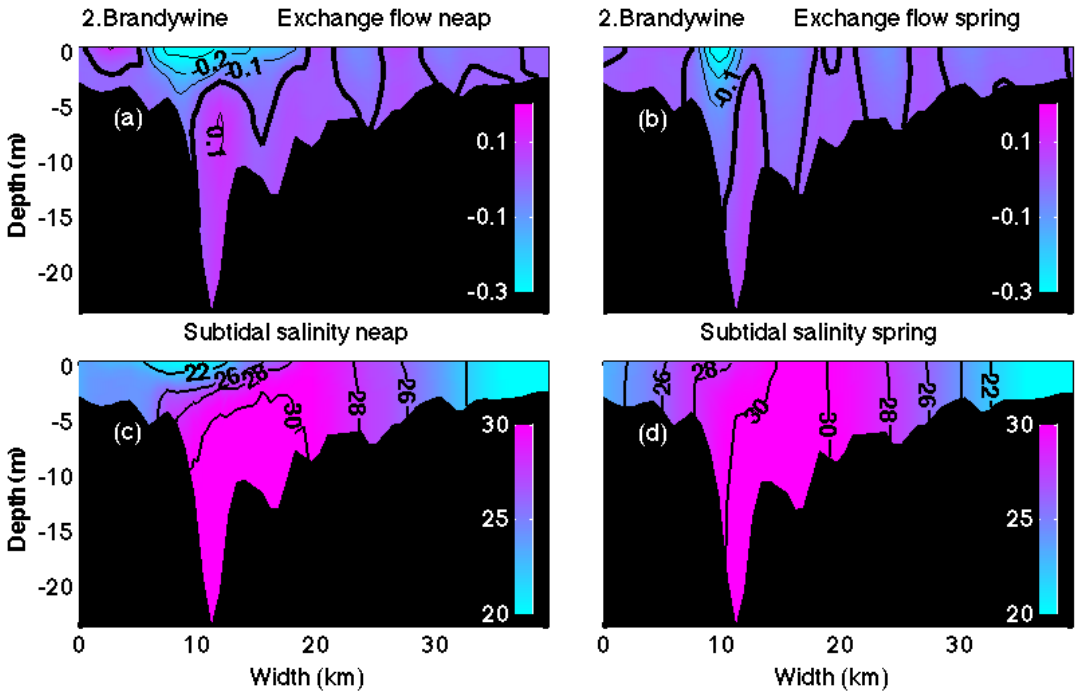

Figure 2.2: Exchange flow and subtidal salinity for station 2: Brandywine Shoal, during periods of neap and spring tide and for a river discharge of 650 m^3/s. The color scale is in m/s for the exchange flow. Positive values of velocity are directed landward. The perspective is looking into the bay.

salinity difference of 8 psu across the channel during neap tide. During spring tide, the water column in the main channel becomes weakly stratified (Fig. 2.2). At Woodland Beach, stratification presents a strong vertical gradient during neap tide of about 11 psu between surface and bottom, but it is significantly reduced to 2 psu during spring tides (Fig. 2.3).

2.5.2 Salt fluxes for mean river discharge conditions $Q = 650\ m^3/s$

Subtidal variability

The along-channel salt fluxes exhibit a marked spring-neap variability. The steady shear dispersion salt flux, F_e, is strongly landward during neap tides ($\sim$ day 68) but weakens considerably during spring tides ($\sim$ day 75) (Fig. 2.4) due to the reduction of both the mean shear and stratification (Fig. 2.2 and 2.3).

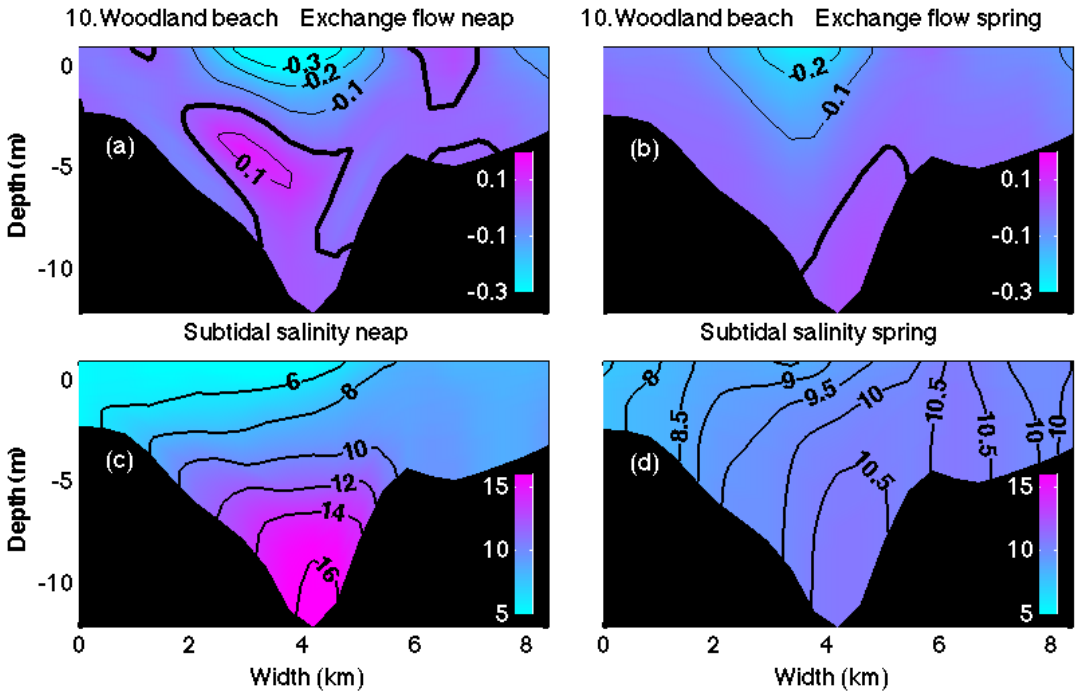

Figure 2.3: Exchange flow and subtidal salinity for station 10: Woodland Beach, during periods of neap and spring tide and for a river discharge of 650 m^3/s. The color scale is in m/s for the exchange flow. Positive values of velocity are directed landward. The perspective is looking into the bay.

At Brandywine Shoal, the tidal oscillatory salt flux, F_t, has a similar subtidal variability but less marked than the steady shear dispersion. F_e is the dominant mechanism during neap tides, but both fluxes have modest but similar contributions during spring tide. The spring-neap variability of F_t is counterintuitive because it decreases with increasing tidal currents and is contrary to existing parameterizations (Banas *et al.* 2004, MacCready 2007). The tidal oscillatory salt flux at Woodland Beach exhibits more robust spring-neap variability and its magnitude is similar to the salt flux associated with the steady shear dispersion. Similar to Brandywine shoal, the tidal oscillatory salt flux at Woodland Beach is maximum during neap tides and minimum during spring tides. We will discuss the cause for this time variability in section 2.5.2. The variability of F_0 at both locations is due to changes of the cross-sectional area average salinity with the spring-neap cycle which has a minimum around spring tides and a maximum at neap tides (Fig. 2.4).

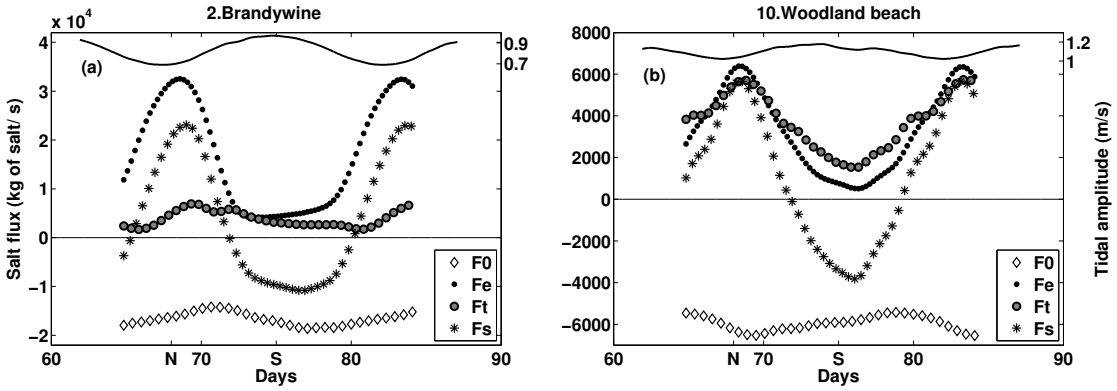

Figure 2.4: Area-integrated salt fluxes for (a) station 2, Brandywine Shoal and (b) station 10, Woodland Beach for a river discharge of 650 m^3/s. F_0, F_e, F_t and F_s stand for river advection, steady shear dispersion, tidal oscillatory and total salt flux respectively. The amplitude of the tidal velocity is at the top of the plots showing periods of neap and spring tide.

The sum of these two components, F_e and F_t, plus the advective salt flux F_0, yield the total salinity salt flux F_s. We can conclude that salt enters the estuary during neap tides and leaves the estuary during spring tides. However the total salt content of the estuary is two orders of magnitude larger than the change of the salt content over the spring-neap cycle. Therefore, changes in the salt intrusion length during the spring-neap cycle are small compared to the extent of the salt intrusion.

Spatial structure

The along-channel spatial structure of the salt fluxes (Fig. 2.5 (a)) shows that during neap tide the steady shear dispersion is the dominant mechanism in the lower and middle bay (0 to ~ 60 km in the along channel direction), except for station 4 (31.5 km from the entrance of the bay) where the tidal oscillatory salt flux is somewhat larger than steady shear dispersion. From stations 10-12 (69 to 85.1 km from the entrance of the bay) F_t is comparable or larger than F_e. Consequently, the values of the dispersive fraction of the downgradient salt fluxes, $\nu = F_t/(F_t + F_e)$ (Fig. 2.5 (c)), has values less than 0.5 for the lower and middle bay (except station 4) and values larger than 0.5 for stations 10-12. During spring tide (Fig. 2.5 (b)), both F_e and F_t are significantly reduced but have similar contributions, and accordingly, ν has values around 0.5 all

along the system (Fig. 2.5 (d)).

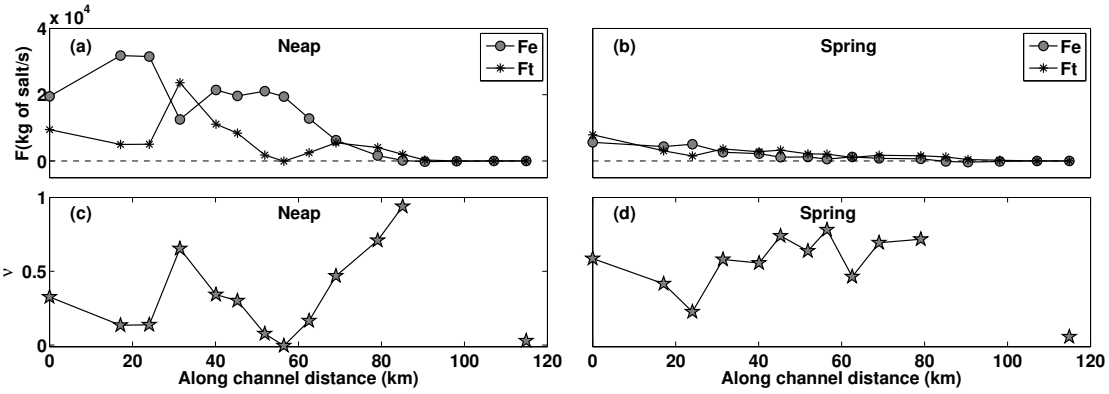

Figure 2.5: (a)-(b) Area-integrated steady shear dispersion (F_e) and tidal oscillatory salt flux (F_t) and (c)-(d) dispersive fraction of downgradient salt fluxes ν, along the estuary for periods of neap and spring tide and for river discharge of 650 m^3/s.

The cross-channel structure of salt fluxes reveals that most of the upstream salt flux occurs in the main channel and is quite small in the flanks (Fig. 2.6 and 2.8). To quantify this, we divide the downgradient salt fluxes, $F_e + F_t$, into contributions from the main channel and the flanks for all 16 sections along the estuary. The area of the main channel was defined as the portion of the total cross-sectional area which depth is larger than the average depth of the cross-sectional area. The area of the flanks is the total cross-sectional area minus the area of the main channel (Fig. 2.7 (a)). This decomposition shows (Fig. 2.7 (c)) that in fact during neap tides the contribution of the main channel dominates the downgradient salt fluxes while the role of flanks is negligible. During spring tide the downgradient salt fluxes are about 2 to 7 times smaller than during neap tide with both flanks and main channel having a similar contribution. Over the spring-neap cycle approximately 88% of the salt fluxes occurs in the main channel despite of only representing between 41% to 67% of the total cross-sectional area.

During neap tide, the steady shear dispersion (Fig. 2.6) is positive everywhere above the main channel. This is consistent with a vertical two layers exchange flow that drives salty water upstream in the lower layer and relatively fresher water downstream in the upper layer. On the other hand, during spring tides, F_e is negative on the flanks

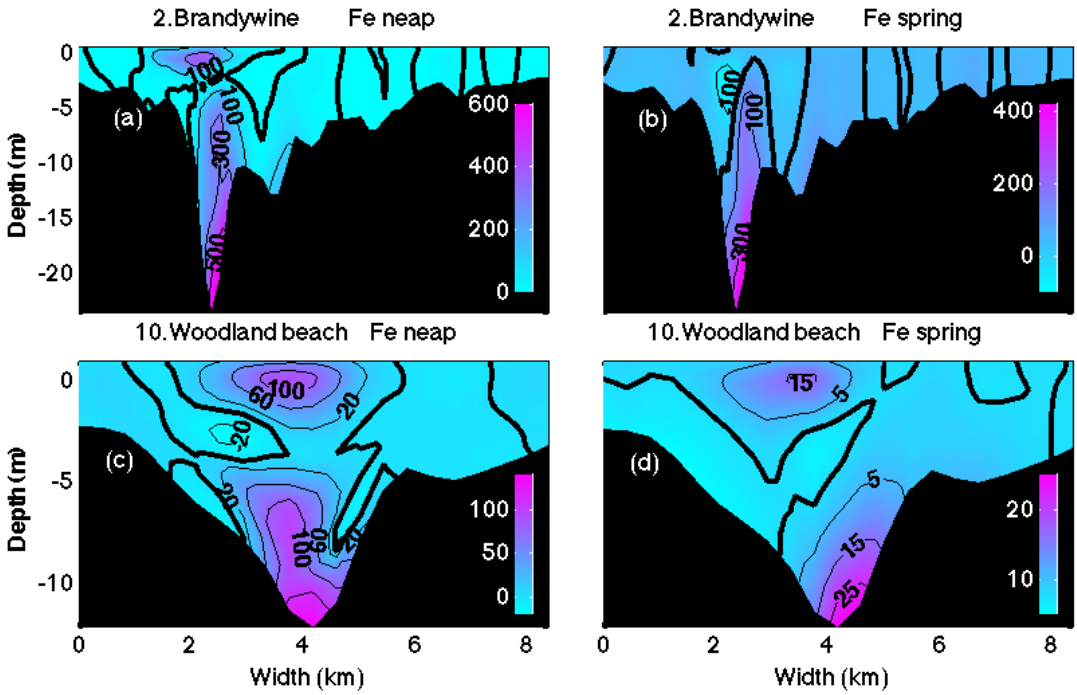

Figure 2.6: Spatial structure of steady shear dispersion at Brandywine Shoal and Woodland Beach, during periods of neap and spring tide for a river discharge of 650 m^3/s. The color scale is in kg of salt/ s with positive values representing landward salt fluxes. The perspective is looking into the bay.

and parts of the main channel due to an exchange flow that is laterally sheared in conjunction with lateral salinity gradients.

To investigate the mechanisms that drive the tidal oscillatory salt flux and, in particular, its spring-neap variability, we plot the spatial structure of F_t across the section at Woodland Beach during spring and neap tidal conditions (Fig. 2.8). We choose this location because of the large spring-neap variability in F_t and because of the the relative importance of F_t at this site. F_t is generally positive throughout the section and particularly so in the upper part of the main channel for both spring and neap tides and has the highest values towards the left flank only during neap tide. This enhancement is caused by an elevated tidal component of salinity (s_t) at this location and a shift away from quadrature between s_t and the tidal component of the along-channel velocity (v_t), both of which are associated with the cross-channel flows acting on the cross-channel salinity gradients.

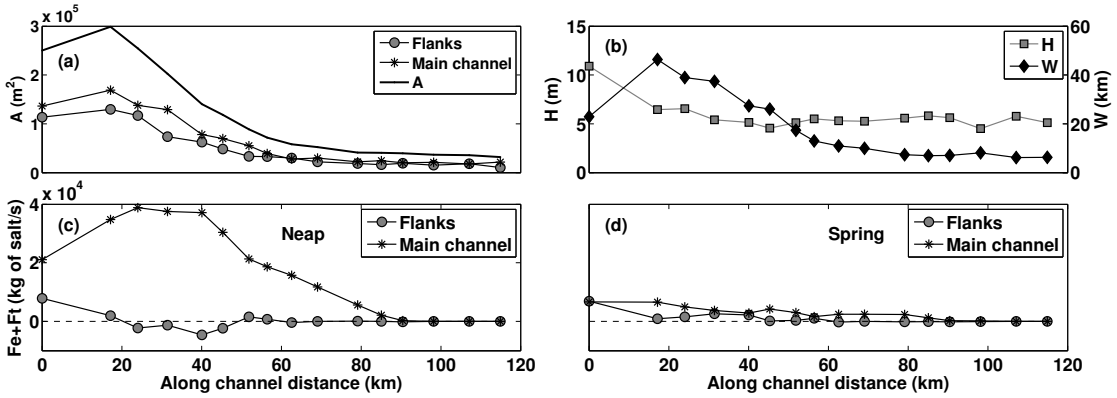

Figure 2.7: (a) Total cross-sectional area (A) and its decomposition into area of the main channel and flanks for the 16 cross-sectional areas defined along the estuary. The area of the main channel and flanks are defined in section 2.5.2. (b) Mean depth (H) of the cross sectional areas and width (W) of each section defined as $W = A/H$. (c)-(d) Downgradient salt fluxes in the main channel and flanks for periods of neap and spring tide for a river discharge of 650 m^3/s.

For example, during neap tide on ebb (Fig. 2.9 (a)), lateral flows advect fresh water from the left flank and the surface of the main channel towards the bottom of the main channel and augments ebbing current's tendency to freshen this region (Fig. 2.9 (c)). This brings the along-channel velocity and salinity out of quadrature, in particular in the left bottom part of the main channel where the phase difference between s_t and v_t is about 2.5 hours, implying that this region is the freshest 0.7 hours before the end of ebb tide (Fig. 2.9 (e) and (g)). This combined with s_t of about -4 produces high positive values of F_t in this region.

A reversal in the cross channel flows on flood (Fig. 2.9 (b)) tends to increase salinity and again augment the flooding tides tendency to increase salinity in the left bottom part of the main channel (Fig. 2.9 (d)). This again brings s_t and v_t out of quadrature, producing positive values of s_t (Fig. 2.9 (f)) resulting in a positive salt flux.

During spring tide, F_t is reduced despite the increase in tidal currents. The reduced stratification (Fig. 2.10 (c) and (d)) yields low values of s_t (Fig. 2.10 (e) and (f)) and this leads to a significant smaller tidal oscillatory salt flux during this period.

The cross-channel flows acting on the salinity field bring velocity and salinity out of quadrature and produce the time variability of the tidal oscillatory salt flux in this

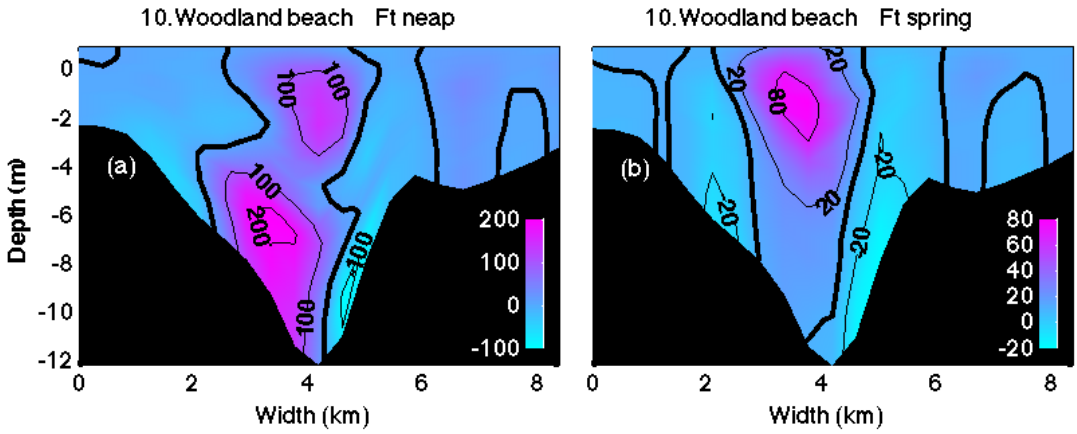

Figure 2.8: Spatial structure of tidal oscillatory salt flux at Woodland Beach, during periods neap and spring tide for a river discharge of 650 m^3/s. The color scale is in kg of salt/ s with positive values representing landward salt fluxes. The perspective is looking into the bay.

system. Therefore, in the next two sections we will discuss the dynamics of the cross-channel flows and develop a scaling for the along channel dispersion coefficient.

2.5.3 Cross-channel momentum balance

The vertical structure of the along and cross-channel flows in the main channel for the Woodland Beach cross section is shown in Fig. 3.11. The magnitude of the cross-channel flows is similar for both spring and neap tide inspite of increased stratification during neap tides. The vertical structure of the secondary flows changes through the tidal cycle but consists of one cell for most of the ebb tide and two cells between approximately 2 hours before and after the end of flood.

To determine the dynamics of the secondary flows we diagnose a cross-channel momentum equation (Eq. 2.6). This equation represents the tendency to drive cross-channel shear and is formed by the difference between the depth dependent and depth average momentum equation.

The balance in the cross-channel direction is given by the baroclinic pressure gradient minus its depth average, the Coriolis force minus its depth average, the vertical viscosity plus the stress at the bottom divided by the total depth of the water column

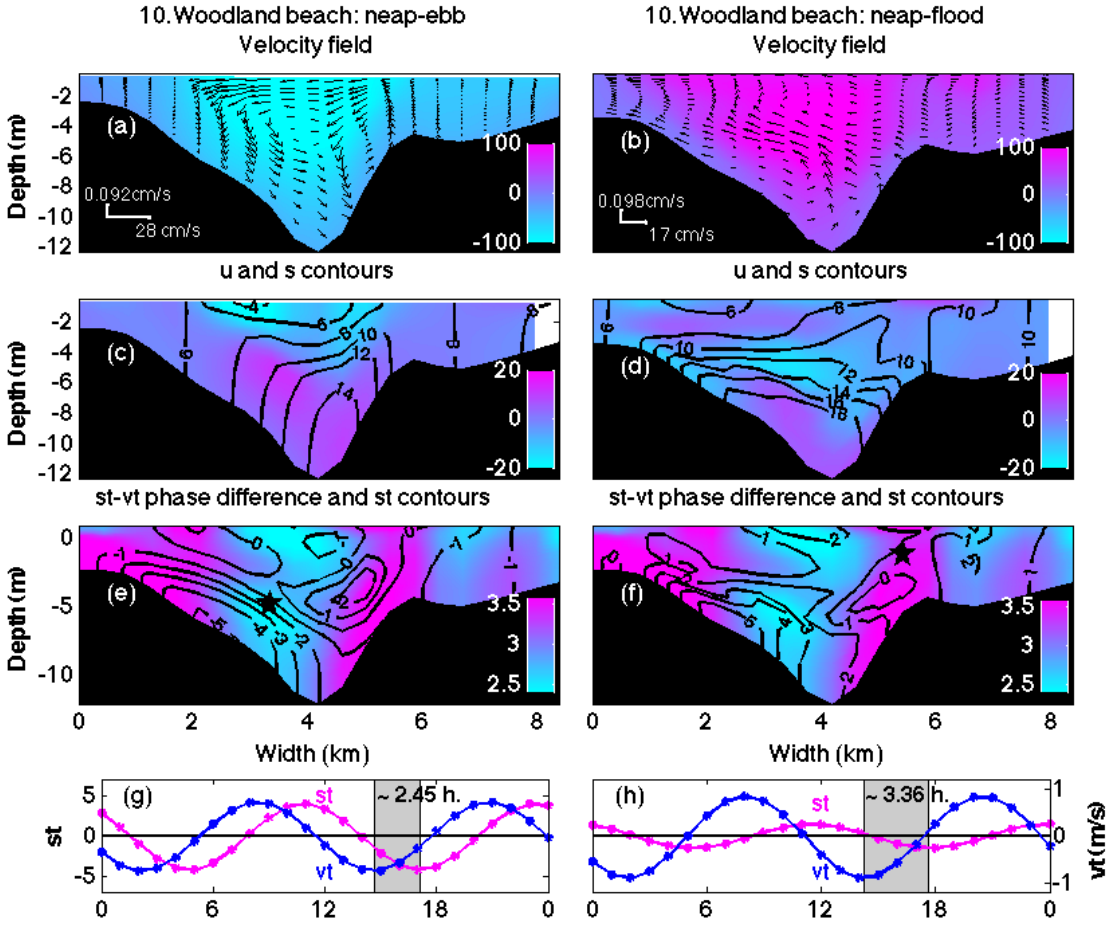

Figure 2.9: (a)-(b) Cross-channel plus vertical velocities (arrows) over imposing the along-channel velocity. The color scale in cm/s with negative velocities representing ebb tide. (c)-(d) Contours of salinity over imposing the cross-channel velocity. The color scale is in cm/s with positive values towards the right flank. (e)-(f) Contours of s_t, the tidal component of salinity, over imposing the phase difference between the M2 component of s_t and the along-channel tidal component of velocity v_t. The color scale is in hours. All the above at Woodland Beach, during neap tide and for a river input of 650 m^3/s . The perspective is looking into the bay. (g)-(h) Time series of the M2 component of s_t and v_t for two different locations in the cross-section: (g) in the main channel and (h) in the right flank. These two locations are shown in (e) and (f) as black stars. The shaded area is the phase difference between s_t and v_t is hours.

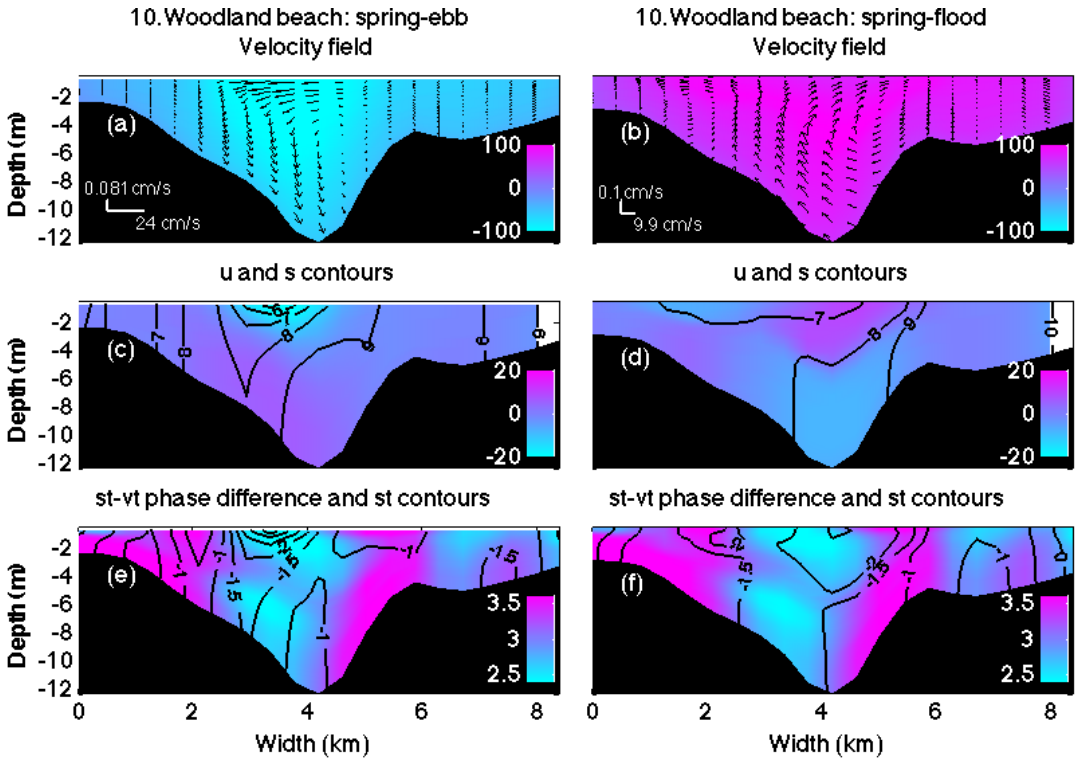

Figure 2.10: (a)-(b) Cross-channel plus vertical velocities (arrows) over imposing the along-channel velocity. The color scale in cm/s with negative velocities representing ebb tide. (c)-(d) Contours of salinity over imposing the cross-channel velocity. The color scale is in cm/s with positive values towards the right flank. (e)-(f) Contours of s_t, the tidal component of salinity, over imposing the phase difference between the M2 component of s_t and along-channel tidal component of velocity v_t. The color scale is in hours. All the above at Woodland Beach, during spring tide and for a river input of 650 m^3/s . The perspective is looking into the bay.

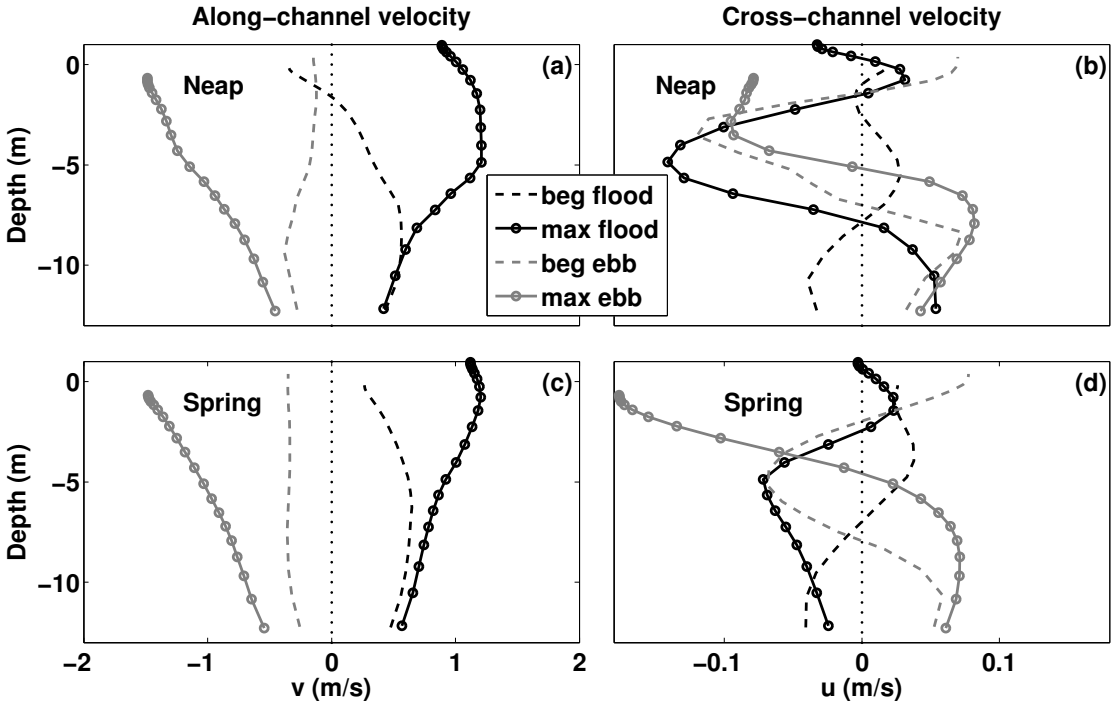

Figure 2.11: Vertical profile of the tidal-phase average of (a),(c) along-channel velocity and (b),(d) cross-channel velocity in the thalweg for Woodland Beach, during neap and spring tide and for a river discharge of 650 m^3/s.

and the total advection of momentum minus its depth average as follows

$$\underbrace{\frac{\partial(u-\overline{u})}{\partial t}}_{\text{accel}} = \underbrace{-\frac{g}{\rho_0}\frac{\partial \rho}{\partial x}(z-\overline{z})}_{\text{prsgrd}} + \underbrace{f(v-\overline{v})}_{\text{cor}} + \underbrace{\frac{1}{\rho_0}\left(\frac{\partial \tau}{\partial z}+\frac{\tau_H}{H}\right)}_{\text{vvisc}} + \underbrace{\left(u\frac{\partial u}{\partial x}-\overline{u\frac{\partial u}{\partial x}}+v\frac{\partial u}{\partial y}-\overline{v\frac{\partial u}{\partial y}}+w\frac{\partial u}{\partial z}\right)}_{\text{adv}} \tag{2.6}$$

Terms in Eq. 2.6 are tidally phase averaged for both neap and spring conditions (Fig. 2.12).

During ebb, neap tide, the cross-channel flows are directed to left (DE. side) at the surface and to the right to the bottom (NJ. side), consistent with rotationally forced flows (Fig. 3.11 (b)). This circulation strains the isohalines in such a way that the salinity in the middle of the channel is fresher than in the right flank (Fig. 2.9 (c)) and as a result a strong cross-channel baroclinic pressure gradient, that opposes Coriolis, is established (Fig. 2.12 (a)). The total acceleration (Fig. 2.12 (a) black line), being the

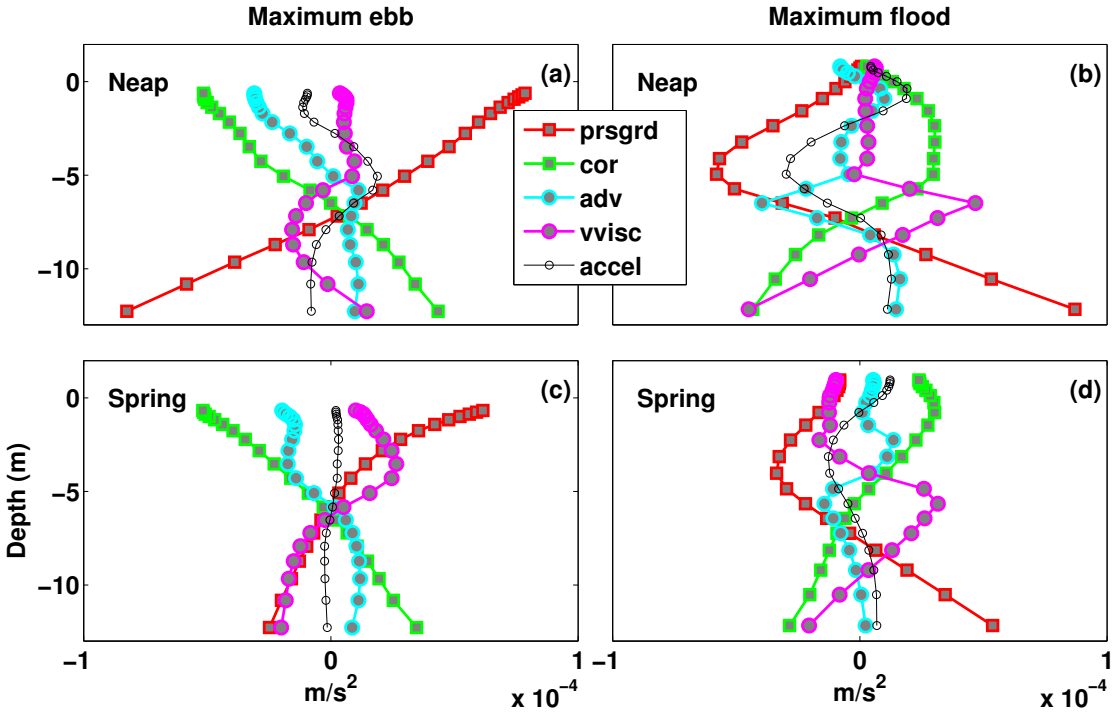

Figure 2.12: Vertical profile of the tidal-phase average of the cross-channel momentum terms in Eq. 2.6, in the thalweg for Woodland Beach at (a),(c) maximum ebb and (b),(d) maximum flood, during neap and spring tide and for a river discharge of 650 m^3/s.

result of the four different forces, accelerates the fluid at the surface but slows it down at the bottom.

During flood, neap tide, the cross-channel flows reverse presenting at times complex vertical structures but one hour after maximum flood a persistent two cells circulation is established with a strong mid depth jet towards the left flank (Fig. 3.11 (b)). This is also consistent with the Coriolis forcing driven by the along channel flows that present a mid depth velocity maximum. This circulation again strains the isohalines, but mostly at mid depth where the jet is found, and produces a cross-channel baroclinic pressure gradient that is approximately a mirror opposite of the rotational force (Fig. 2.12(b)). The total acceleration (Fig. 2.12(b) black line) then yields this two cell circulation by accelerating the fluid at the surface towards the right and at mid depth towards the left.

These dynamics also apply during spring tide, with the difference that the cross-channel baroclinic pressure gradients are weaker because stratification is significantly reduced during this period. Interestingly the advection terms are also quite significant in the cross-channel momentum balance associated with lateral variability in density field.

In summary, the flow structure and dynamics are consistent with Ekman forced flows that are modified by the cross-channel baroclinicity.

2.5.4 Scaling for the along channel dispersion coefficient

Here we propose a scaling for the along channel dispersion coefficient due to tidal processes K_t. The scaling is based on the fact that tidal oscillatory salt flux is caused by tidal correlations of velocity and salinity field: $F_t = \int v_t s_t dA$. This implies that if these two quantities are correlated at tidal time scales, i.e. they are out of quadrature, F_t is enhanced not only by an increase in tidal velocity, v_t, but also but an increase in tidal salinity, s_t. From our results, we obtained that the values of s_t were significantly enhanced during neap tides and so s_t was scaled as proportional to Δs. v_t was scaled as the amplitude of the along-channel velocity V. When F_t is expressed as the product of an along channel dispersion coefficient, K_t, and the along channel salinity gradient, $\frac{\partial s}{\partial x}$, K_t can be scaled as

$$K_t \propto V \Delta s \frac{L}{s_{ocn}} \tag{2.7}$$

where L is the length of the salt intrusion and s_{ocn} is the oceanic salinity.

To test this scaling, the left and right hand side of of Eq. 2.7 were calculated for each of the 16 stations along the estuary for the 6 different runs with different river input. V was obtained as the depth average of the amplitude of the along channel velocity in the main channel. Δs was calculated as the low passed bottom to surface salinity difference for the cross-channel average salinity. L was chosen as the average location of the 0.1 isohaline for each river input and s_{ocn} was set to 32. After obtaining an along channel average of the left and right hand side of the quantities in Eq. 2.7, a non-linear fit of these points were performed, which yielded a fit of the form (Fig. 2.13

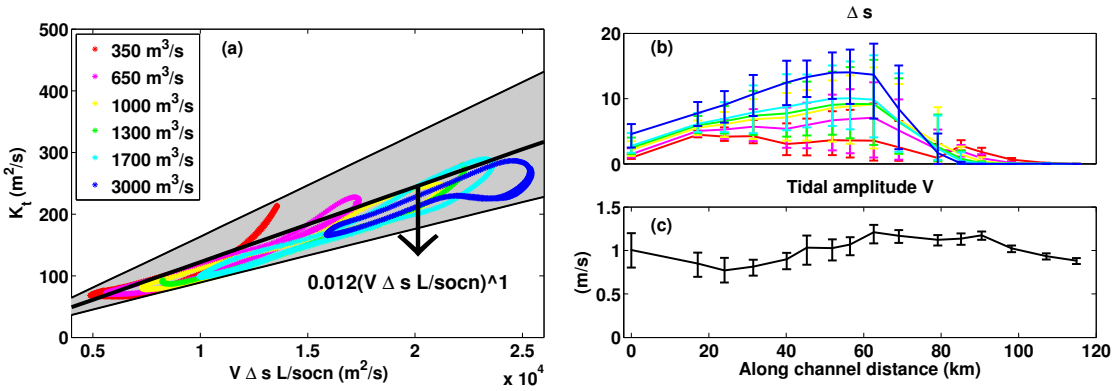

Figure 2.13: (a) Scaling for the tidal dispersion coefficient K_t as a function of: bottom to surface salinity difference, Δs, amplitude of the along-channel velocity, V, the salt intrusion length, L and the oceanic salinity, s_{ocn}. On the plot the color stars are the K_t vs. $V\Delta sL/s_{ocn}$ value for different river inputs, and the black line is the best fit of these points. The grey area around the black line is the 95 % confidence bounds of the fit. (b) Bottom to surface salinity difference for the 16 stations along the estuary for the 6 different river inputs. The error bars represent the range of values during the spring-neap cycle. (c) Amplitude of along-channel velocity for the 16 stations along the estuary. The error bars represent the range of values during the spring-neap cycle.

(a))

$$K_t = (0.012 \pm 0.0019)\left(V\Delta s\frac{L}{s_{ocn}}\right)^{0.998\pm0.015} \tag{2.8}$$

where the uncertainty in the fitting parameters is the 95 % confidence intervals for the non-linear least square fit. The above scaling states that the along channel dispersion coefficient is proportional to the magnitude of the tidal velocity, V, which is consistent with previous parameterization but additionally is proportional to bottom to surface salinity, Δs. Because the change of V over the spring-neap cycle is about 10 times smaller than the change of Δs (Fig. 2.13 (b) and (c)), the change in stratification is much more dominant than the change in tidal velocity in this system and, as a result, F_t is enhanced during neap tide.

2.6 Discussion

2.6.1 Salt intrusion length for mean river discharge conditions $Q = 650m^3/s$

The position of the 0.1 isohaline varies between 98 km, at the end of spring tide, and 106 km, at the end of neap tide (Fig. 2.14(a)) which is consistent with a system that loses and gains salt during spring and neap tide respectively. Garvine *et al.* (1992) obtained the mean along-channel salinity structure using a long term salinity data for a wide range of river discharges and found that the mean salt intrusion length, defined as the location where $s = 0$, is 96.7 km from the entrance of the bay. Our results are in good agreement with the results by Garvine *et al.* (1992) suggesting that the idealized 3D model is capturing the main features of the salt dynamics in Delaware Bay.

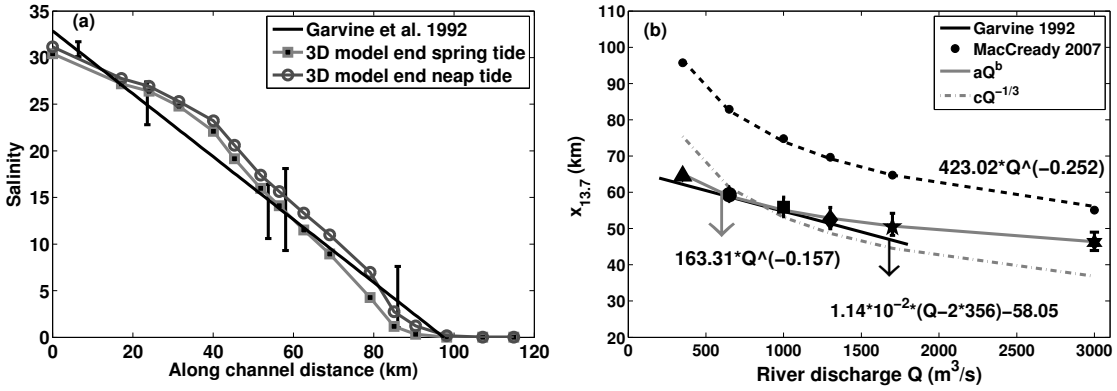

Figure 2.14: (a) Along-channel salinity structure for a river discharge of 650 m^3/s from the 3D model, compared with the observations by (Garvine *et al.* 1992). (b) Response of the 13.7 isohaline to river discharge. The different makers represent the position of the 13.7 isohaline for different river inputs from the 3D model with the error bars representing the spring-neap variability in the position of this isohaline. The gray solid line is the best fit of these points. The dashed-dotted line is the $cQ^{-1/3}$ fit for the 3D output. The black solid line is the result of a linear fit from observations performed by Garvine *et al.* 1992. The black circles are the results from MacCready (2007) and the black-dashed line is the best fit for these points.

2.6.2 Response of the salinity field to river discharge

Based on the series of simulations we estimated the salt intrusion length as a function of river discharge over a range of isohalines:

$$L(s=0.1) = (206.1 \pm 32.2)Q^{(-0.113\pm0.023)}\ ,\ L(s=2) = (169.0 \pm 23.3)Q^{(-0.103\pm0.020)}\ ,$$
$$L(s=8) = (190.0 \pm 32.4)Q^{(-0.148\pm0.025)}\ ,\ L(s=13.7) = (163.3 \pm 18.0)Q^{(-0.157\pm0.016)}\ ,$$
$$L(s=20) = (114.0 \pm 22.3)Q^{(-0.143\pm0.029)} \tag{2.9}$$

where the interval in the fitting parameters is the 95 % confidence bounds for the non-linear least square fit. In particular we see that the position of the 13.7 isohaline (Fig. 2.14 (b)) is in good accordance with the observations by Garvine *et al.* (1992) for total river input of 650, 1000 and 1300 m^3/s, slightly differs for the smallest value: 350 m^3/s but differs significantly for the highest values: 1700 and 3000 m^3/s. The reason for this is that the fit in Garvine *et al.* (1992) is a linear fit that is representative of small to moderate river discharges with a mean value of 356 m^3/s and a standard deviation of 338 m^3/s for river discharge at Trenton. The low exponent of all the isohalines fits demonstrates that the salt field is quite insensitive to river discharge.

The key to the observed dependence of L on Q in the Delaware Bay appears to be both the dependence of steady shear dispersion, F_e, and tidal oscillatory salt flux, F_t, on Q and particularly on the relative importance of F_t to the net upstream salt flux (i.e. $\nu = F_t/(F_e + F_t)$). The dependence of steady shear dispersion and tidal oscillatory salt flux with river discharge (Fig. 2.15 (a)) reveals that steady shear dispersion has an important dependence with Q, $F_e = 22.88Q^{0.901}$, and so it is close to be proportional to Q. On the other hand, the tidal oscillatory salt flux has a weaker dependence, $F_t = 33.23Q^{0.719}$, such that it increases approximately 5 times for a 8.5 increase in Q and is consistent with the increase of F_t during neap tide associated with an increase in stratification. Furthermore the advective salt flux F_0 has a dependence given by $F_0 = -31.7Q^{0.891}$ (Fig. 2.15 (b)). This dependence occurs because $F_0 = -QS_0$, where S_0 is the cross-sectional average salinity and decreases with increasing river input, and therefore F_0 has a weaker dependence than direct proportionality with Q.

Additionally during low flow condition there is a similar contribution of steady and

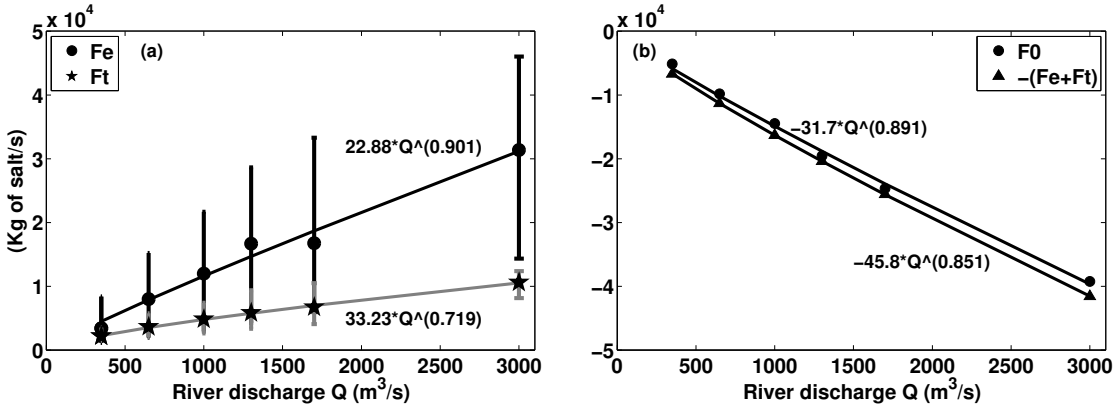

Figure 2.15: (a) Along-channel average of the steady shear dispersion and tidal oscillatory salt flux, $\int F_e dx / \int dx$ and $\int F_t dx / \int dx$, as a function of river discharge. The error bars represent the spring-neap variability of these quantities. (b) Time mean of the along-channel average $\int F_0 dx / \int dx$ as function of river discharge and the direct sum of the function $F_e + F_t = 22.88Q^{0.901} + 33.23Q^{0.719}$. In both figures, the integrations are performed over the length of the salt intrusion and the equation next to each curve is the best fit of the mean value of the along-channel average.

oscillatory salt fluxes, e.g. $\nu \approx 0.34$ for $Q = 350\ m^3/s$. However as river flow increases ν decreases, e.g. $\nu \approx 0.25$ for $Q = 3000\ m^3/s$. While F_t increases with $Q^{0.72}$, F_e increases as $Q^{0.90}$ and thus, for relatively high river discharge, F_e mainly balances the seaward salt flux associated with the river discharge with $Q^{0.89}$. In summary, for low flow conditions both F_t and F_e contribute in determining L, while for high river flows F_e dominates. Thus the weakening influence of F_t with increasing Q suggest that it is the increase in F_e with Q that is primarily responsible for stiffening the salt field under high flows.

Using the theory of Hansen and Rattray (1965) and assuming that the only mechanism responsible for the downgradient salt flux is steady shear dispersion, a scaling for the salt intrusion length is obtained (Monismith *et al.* (2002))

$$L_s \propto (g^2\beta^2)^{1/3} \frac{A^{1/3} H^{8/3}}{(K_m^2 K_s)^{1/3}} \frac{1}{Q^{1/3}} \left(\frac{s_{oc} - s}{s_{oc}^{1/3}} \right) \tag{2.10}$$

where g is gravitational acceleration, β is the haline contraction coefficient, S_{oc} is oceanic salinity, A is cross-sectional area, H depth, K_m and K_s vertical eddy viscosity and diffusivity, Q is river discharge, s is a specific salinity value and L_s is the distance from the mouth of the estuary to the isohaline s. It should be noticed that the functional

dependence on Q shown by Eq. 2.10 is the same for any isohaline in the system because it assumes a constant along-channel salinity gradient. Equation 2.10 states that $L \propto Q^{-1/3}$ which implies a more sensitive response of the salt field to changes in river input than the response exhibited by Delaware Bay. This scaling fails in this system in part because it neglects the contribution of the tidal oscillatory salt flux to the downgradient salt fluxes, but it also assumes a vertical eddy viscosity that is independent with Q.

For instance, Monismith *et al.* (2002) found that in San Francisco Bay $L \propto Q^{1/7}$ and they attributed the stiffening of the salinity field to the increased stratification with increasing river discharge, which in turn increases the estuarine circulation and therefore enhances the upstream steady shear dispersion salt flux. Results from the 3D model show that the vertical eddy viscosity K_m is approximately reduced by half with an 8.5 fold increase in river input (Fig. 2.16(a)).

Alternatively, Ralston *et al.* (2008), based on Eq. 2.10, proposes that bathymetry can be a determining factor for the response of salt intrusion length to river discharge. Following a similar approach as Ralston *et al.* (2008), we defined a weighted geometrical factor as

$$\bar{G} = \frac{\int A^{1/3} H^{8/3} \frac{\partial s}{\partial x} dx}{\int \frac{\partial s}{\partial x} dx} \tag{2.11}$$

and obtained that $\bar{G} \propto Q^{0.162}$, which combined with $Q^{-1/3}$ yields $L \propto Q^{-0.171}$. So the inclusion of the geometrical factor does not completely explain the sensitivity of the various isohalines with river input (Eq. 2.9), though it does weaken the response. A similar conclusion was obtained by Monismith *et al.* (2002) when in their 1D model they included variable bathymetry but no tendency of stratification to reduce vertical mixing and found that L versus Q relationship was less sensitive to Q than the $Q^{-1/3}$ dependence.

Additionally, we estimated $\bar{K} = \int A^{1/3} H^{8/3} (K_m^2 K_s)^{-1/3} dx / \int dx$, that is the along-channel average of the factor accompanying the $Q^{-1/3}$ in Eq. 2.10, and found that it scales with $Q^{0.223}$ (Fig. 2.16 (b)), which combined with $Q^{-1/3}$ gives $L \propto Q^{-0.110}$, a very close response to the salt intrusion length for $s = 0.1$ and $s = 2$ obtained with the 3D model. We also calculated the factor $\bar{K} = \int (K_m)^{-1} dx / \int dx$, and obtained a

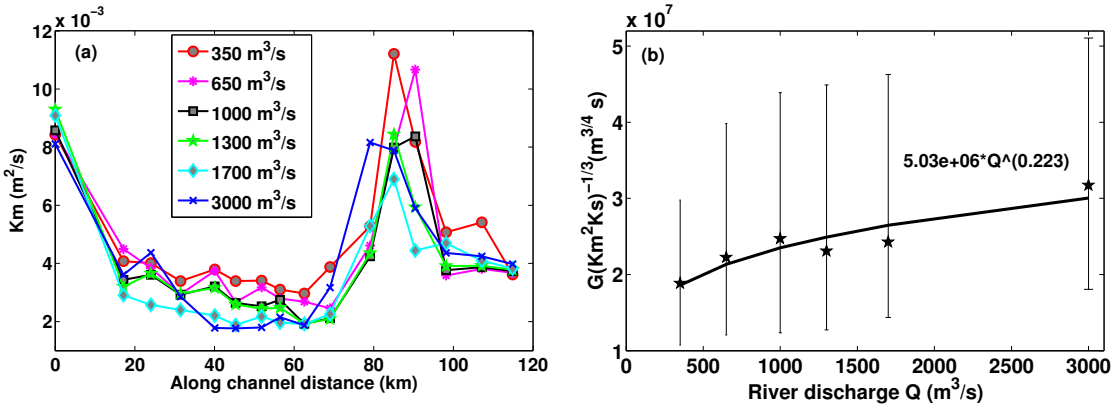

Figure 2.16: (a) Time-mean vertical eddy viscosity K_m as a function of along-channel distance for different river discharges. Here, K_m for each of the 16 cross-sectional areas, was calculated by finding the grid points where the vertical salinity gradient was maximum and averaging these values for every time step. (b) Along-channel average of the factor accompanying $Q^{-1/3}$ in Eq. 2.10: $\int \frac{A^{1/3}H^{8/3}}{(K_m^2 K_s)^{1/3}} dx / \int dx$. Here, the integration is performed over the length of the salt intrusion. The error bars represent the spring-neap variability of this quantity. The equation next to the curve is the best fit of the mean value of the along-channel average.

functional dependence with Q ($Q^{0.218}$) that was very close to the response that includes the geometrical factor. The reason these two approaches yield similar results is that neither H nor A show much variability in the region where the head of salt resides across these simulations ($\sim 80km - 110km$) (Fig. 2.7) and, thus, the dependence of $\bar{K}$ on Q is primarily due to changes in K_m rather than that associated with the geometric factor. This suggests that the vertical eddy viscosity is playing a important role on controlling the salt intrusion length in this system.

2.6.3 Insights from the 3D model and MacCready model

The salt intrusion length estimated by a two dimensional model by MacCready 2007 is significantly longer than observational results by Garvine *et al.* 1992 and the 3D numerical simulations (Fig. 2.14(b)). In this 2D model an, exponentially decaying cross-sectional area with along-channel distance and constant depth are used to represent the bathymetry of Delaware Bay. Motivated by the 3D model results that most of the downgradiant salt fluxes occur in the main channel, we ran the MacCready model for a river input of 650 m^3/s for two cases: case one uses the original area, depth and

tidal velocity used in MacCready (2007) and case two uses the area that was defined in section 2.5.2 (Fig. 2.7 (a)) and a depth that also varies in the along channel section and is equal to the mean depth of the main channel in each segment. The tidal velocity is prescribed with an along-channel variation given by

$$\begin{aligned} x < 80km \quad & U_t = \tfrac{(x-40)^2}{4*1000} + 0.8\ m/s \\ x >= 80km \quad & U_t = 1.2\ m/s \end{aligned} \tag{2.12}$$

similar to the tidal velocities obtained with the 3D model. Additionally, the along-channel dispersion coefficient K_h was set to a constant value of 150 m^2/s that is representative of the values obtained with the 3D model. For the vertical eddy viscosity K_m we used the parameterization by Ralston *et al.* (2008) multiplied by a factor of 0.5 so the stratification would resemble closer to the stratification with the 3D model. The results show that for the case of the original area (Fig. 2.17(a)) the salt intrusion length is significantly overpredicted, but for the case of the main channel area (Fig. 2.17(b)) the salt intrusion length is shorter and closer to the one predicted by the 3D model and Garvine *et al.* (1992). It is well known that the salt intrusion is highly sensitive to channel morphology. Indeed the classic theory encapsulated in Eq. 2.10 indicates that L scales with $H^3W^{1/3}$, where W is the width of the cross-sectional area and so a small change on H would imply a much larger change on L.

Comparison between the 3D and 2D model salt fluxes provide insights into the failure of the 2D model when run in the original bathymetry (Fig. 2.18 (a) and (c)). During neap tide Fe in both models have similar magnitudes up to 60 km from the entrance of the bay, but beyond this point is significantly over predicted. However, the biggest mis-match is associated with Fe during spring tide where it exceeds that of the 3D runs by approximately one order of magnitude in the middle reach of the estuary (between 40 and 80 km from the entrance of the bay). The use of an effective area reduces this mis-match but still persists during spring tide (Fig. 2.18 (b) and (d)). We suggest that the reason for this is that the spring-neap variation in stratification in the 2D model is muted due to the insensitivity of the mixing parameterization to stratification. For example, In the 2D model vertical mixing varies by a factor of 2 over

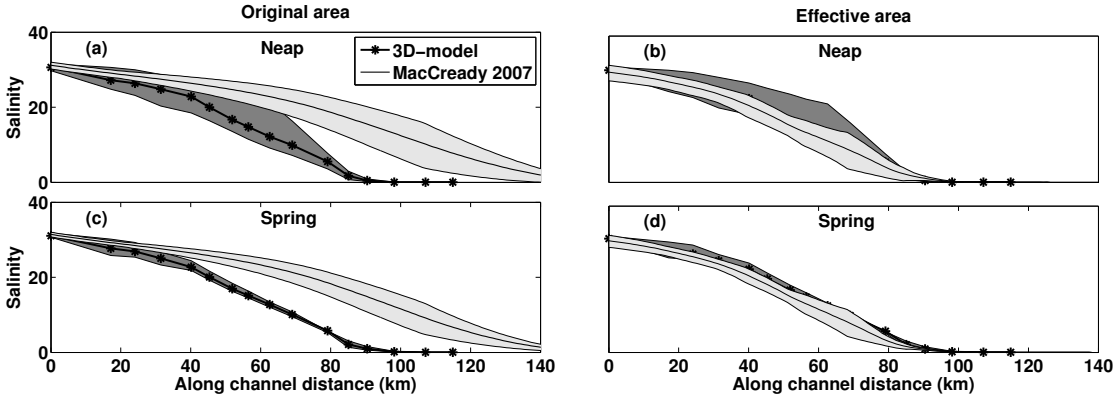

Figure 2.17: Along-channel salinity from the 3D numerical model and the MacCready (2007) model, with the parameterization for the vertical eddy viscosity proposed by (Ralston *et al.* 2008) for: (a),(c) using the original area in MacCready (2007), and (b), (d) using as area the area of the main channel, as defined in section 2.5.2, and the mean depth of the main channel. The shaded area represents the surface to bottom salinity difference.

the spring-neap cycle while in the 3D model mixing varies over an order of magnitude. This suggests that a mixing parameterization that is more sensitive to stratification may improve the models ability to capture the spring-neap variability.

2.7 Summary and conclusions

Based on 3D numerical simulations of Delaware Bay using ROMS we provide a description of the subtidal circulation, salinity structure and salt fluxes in the system. The subtidal circulation presents two different regimes in this system. One is such that the exchange flow is laterally sheared and corresponds to the lower and middle bay where the estuary is the widest and is characterized by a deep channel and wide shallow flanks. The other in which the exchange flow is mostly vertically sheared and corresponds to the upper estuary where the system considerably narrows. The subtidal salinity field presents similar characteristic to the subtidal circulation being laterally segregated in the lower and middle bay and vertically segregated in the upper estuary.

For mean river discharge conditions, $Q \approx 650 m^3/s$, steady shear dispersion and tidal oscillatory salt flux exhibit an enhancement during neap tide and weakening during spring tide producing a total landward and oceanward salt flux during neap and

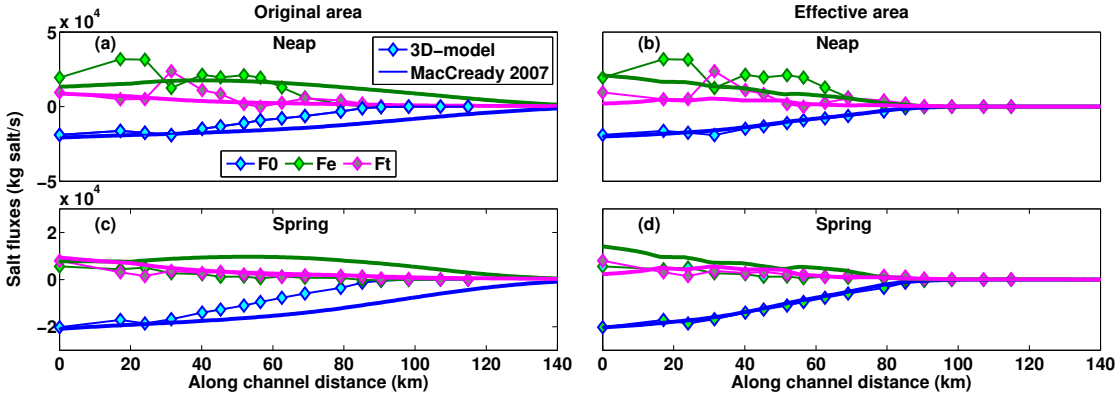

Figure 2.18: Area-integrated salt fluxes from the 3D numerical model and the MacCready (2007) model with the parameterization for the vertical eddy viscosity proposed by (Ralston *et al.* 2008), (a),(c) using the original area in MacCready (2007), (b),(d) using as area the area of the main channel, as defined in section 2.5.2, and the mean depth of the main channel. F_0, F_e and F_t stand for advective salt flux, steady shear dispersion and tidal oscillatory salt flux respectively. The diamonds are the 3D model results and the solid lines are the results from the MacCready model.

spring tide respectively. This spring-neap variability of the tidal oscillatory salt flux is contrary to previous parameterizations (Banas *et al.* (2004) and MacCready (2007)) and is caused by an enhancement of the tidal component of salinity (s_t) during periods of high stratification. This increase on s_t is induced by the action of the cross-channel flows over the salinity field that additionally bring the along-channel velocity and salinity out of quadrature. These cross-channel flows are driven by the action of Coriolis, but as these flows develop, they strain the isohalines and create cross-channel density gradients that compete with the Coriolis forcing. The resultant cross-channel flows have a vertical structure that is mostly characterized by one cell during ebb tide and two cells during flood tide.

A scaling for the along channel dispersion coefficient K_t is proposed such that K_t is proportional to the amplitude of the tidal velocity V and bottom to surface salinity difference Δs. Given that the changes during the spring-neap cycle in Δs are much more predominant than changes in V, K_t is enhanced during periods of high stratification.

The 3D simulations revealed that the landward salt fluxes were primarily confined to the main channel. This lead to a modification of the 2D model that utilized an

effective bathymetry defined by the region where the landward salt flux was concentrated. While this significantly improved the 2D models ability to estimate salt fluxes and salt intrusion length, it still failed to adequately capture the spring-neap variation in stratification that occurred in the 3D model. We suggest that this is due to the insensitivity of mixing parameterization to stratification in the 2D model.

We studied the dependence of salt intrusion length with river input. The 3D model results showed that the salinity field is quite insensitive to river discharge (Eq. 2.9) significantly deviating from the $Q^{-1/3}$ scaling. Our analysis shows that this insensitivity is in part caused by the dependence of F_e and F_t with Q and the relative importance of F_t to the total upstream salt flux (ν). The tidal oscillatory salt flux has a weaker response with Q than steady shear dispersion and therefore allows the salt field to migrate oceanward, but as river discharge increases F_t becomes less important and F_e becomes the dominant mechanism stiffening the salt field. This stiffening for high river discharges is caused by a reduction of the vertical eddy viscosity with an increase in river discharge. This dependence of K_m with Q allows the salt field to migrate further upstream as proposed by Monismith *et al.* (2002) and competes with the $Q^{-1/3}$ dependence. While bathymetry strongly constrains the salt intrusion length as both the classic theory and Ralston et al (2008) suggest, bathymetry alone could not explain the insensitivity of L on Q. Instead, the reduction of mixing with increased river discharged must be taken into account.

In summary, our conclusions are consistent with the idea that Delaware Bay has a buffering mechanism such that the effective along-channel dispersion is close to be proportional to river discharge (Paulson (1970); Garvine *et al.* (1992); Whitney and Garvine (2006)).

2.8 Acknowledgments

This work was supported by a National Science foundation Grant OCE-0928567 and OCE-0825833. We thank NSF NCAR's computational support for providing computer time to run most of the simulations. The author Maria Aristizabal was founded by

a Dupont Fellowship and a Graduate Assistenship from IMCS at Rutgers University. We thank John Wilkin for his invaluable help with the details of the model and for providing the grid of Delaware Bay. We also thank Parker MacCready for letting us use his eta2d model. Finally we thank Steve Monismith and an anonymous reviewer for their thorough comments that helped to improve this manuscript.

Chapter 3

Mechanisms driving stratification

3.1 Abstract

An observational study in the middle reach of Delaware Bay shows that stratification is often enhanced during flood relative to ebb, contrary to the tidal variability predicted by the tidal straining mechanism. This tidal period variability was more pronounced during times of high river discharge when the tidally mean stratification was higher. During low flow conditions, stratification was weaker and its tidal period variability conformed with the tidal straining mechanism. It is shown that there is a competition between the straining caused by the along and cross-channel flows: while the along channel flows stratify the water column during ebb, the cross-channel flows tend to de-stratify it, while the opposite occurs on the flood.

A diagnosis of the cross-channel momentum balance reveals that the lateral flows are driven by the interplay of Coriolis and cross-channel pressure gradient. During the flood tide these two forces mostly oppose each other, while during the first half of the ebb tide they act in concert. This sets up a lateral circulation that strains the isohalines during the ebb reducing vertical stratification and producing a significant cross-channel density gradient. Subsequently, during the flood, the isohalones adjust enhancing water column stability.

3.2 Introduction

Stratification in estuaries is driven by a competition between vertical mixing induced by wind and tides and the fresh water buoyancy input. These processes together establish the observed along-channel and vertical density gradients. At subtidal time scales the

estuarine exchange flow always promotes a stable water column, but the intensity of the stratification depends on the mixing strength controlled by the spring-neap cycle. On top of this background stratification there is a tidal variability in stratification. Simpson *et al.* (1990) proposed the tidal straining mechanism to explain the periodic stratification observed in the Region Of Fresh water Influence (ROFI) of Liverpool Bay (Sharple and Simpson 1995, Rippeth *et al.* 2001). According to this mechanism, changes in stratification are caused by differential advection, due to the vertical shear of the tidal velocities, acting on the horizontal density gradient.

Observations in the Rhine ROFI also showed large semidiurnal variations in stability under conditions of weak mixing (Simpson and Souza 1995, Souza and Simpson 1995). These semidiurnal variations are caused by a cross-shore tidal straining, which interacts with the density gradient to induce or reduce stratification. This cross-shore tidal straining is driven by a two step process: first stratification causes a decoupling of the surface and bottom tidal ellipses (Souza and Simpson 1996) and second, the minor axis component of the tidal ellipses drive the subsequent straining. This contrasts with the Liverpool ROFI, where the straining is caused by the main-axis component of the almost rectilinear tidal ellipse. Whether the main or minor-axis of the tidal ellipses is the one that strains the density field depends on which component is aligned with the density gradient.

Semidiurnal changes in stratification have also been observed in a variety of estuaries (Jay and Smith 1990, Sharples *et al.* 1994, Nepf and Geyer 1996, Stacey *et al.* 1999, Chant and Stoner (2001), Cheng *et al.* 2009). In these systems where tidal flows are highly elongated , it is the shear in the along-channel tidal velocities that interact with the along-channel density gradient to produce the tidal variations in vertical stability. These variations are such that the water column is well mixed at the end of flood and reaches maximum stability at the end of ebb (Simpson *et al.* 1990). Nevertheless, there have been observational studies in a number of systems that have shown that this tidal variability in stratification is not always apparent. For example, observations in a channel in northern San Francisco Bay (Lacy *et al.* 2003) showed that vertical stratification can develop during spring flood-tides. This is because during these periods the

lateral density gradient far exceeded the longitudinal density gradient, and therefore the onset of stratification was caused by the lateral baroclinic forcing that surpassed turbulent mixing. More recently, Scully and Geyer (2012) also showed that in the upper Hudson tidal variations in stratification are not consistent with the along-channel straining mechanism. They attributed this to a competition between the along-channel and cross-channel advection of vertical salinity gradients ($\partial s/\partial z$) and tidal asymmetries in vertical mixing. These processes are likely to be negligible during well mixed conditions because as ($\partial s/\partial z$) becomes small, both longitudinal advection of stratification and cross-channel density gradients are reduced. This implies that a periodic stratification that agrees with longitudinal tidal straining is more likely to manifest during well mixed periods such as found in Liverpool Bay (Simpson *et al.* 1990).

In order to quantify the different processes that control stratification, Simpson and Hunter (1978) defined the potential energy anomaly ϕ as the total amount of work per unit volume required to completely mix the water column. The potential energy anomaly has been used as a framework in a number of observational and numerical studies. Simpson and Hunter (1974), Simpson (1981) and Simpson and Bowers (1981) studied the behavior of fronts in the shelf seas around U. K., assuming surface heating as the only source of stratification and stirring due to winds and tidal stresses as the destabilizing source. Simpson *et al.* (1990) then expanded his analysis to estuaries by including the effects of horizontal density gradients induced by freshwater buoyancy inputs at the boundaries. Later, de Boer *et al.* (2008) derived a dynamic equation for ϕ that was suitable for the analysis of 3D models and applied it to an idealized simulation of the Rhine ROFI. They assumed constant depth and zero surface and bottom density fluxes. Furthermore, Burchard and Hofmeister (2008) rigorously derived $\partial\phi/dt$ based on the dynamic equations for temperature and salinity, the continuity equation and the non-linear equation for sea water. All these studies have demonstrated that the potential energy anomaly is a extremely useful tool to quantify the different mechanism that control water instability in estuaries and coastal seas.

Our observations in Delaware Bay on the East Coast of the USA show substantial changes in stratification levels at tidal time scales but this variability is opposed to

the one predicted by the tidal straining mechanism. The aim of this work is to understand the physical mechanisms that mediate this tidal variability in stratification using the potential energy anomaly approach and an analysis of the cross-channel momentum balance. Indeed it is important to improve our understanding of what controls stratification at tidal time scales in estuaries since stratification is central to estuarine dynamics and significantly controls biogeochemical processes, such as sediment transport, biological production, hypoxia and carbon storage among others.

3.3 Study site

Delaware Bay is a coastal plain estuary located on the east coast of the US. Its main tributary is the Delaware river, which accounts for $50\% - 60\%$ of the total fresh water input into the bay. The Schuylkill and Christina river are the second and third rivers in importance and contribute 15% and 8% respectively (Wong 1994). Based on statistics from a one hundred year record (USGS 2012), the mean annual Delaware River discharge at Trenton is 342 m^3/s and averages ≈ 200 m^3/s during the summer and fall but increases to ≈ 630 m^3/s during the spring freshets and it can exceed 5000 m^3/s during extreme storms events.

The bathymetry of the system is characterized by shallow flanks and a deep main channel that has been dredged since the late 19^{th} century. The bay's mean depth is 8 m with a maximum depth of 45 m. This system presents a relatively simple geometry (Fig. 3.1) with a mouth that is 18 km wide and a maximum width of 40 km at 17 km from the entrance of the bay. Beyond this point the system narrows, resembling a funnel shape.

In the literature Delaware Bay has been classified as a weakly stratified estuary (Beardsley and Boicourt 1981, Garvine *et al.* 1992), but from our observations we see that this system can have a vertical stratification as high as 9 during periods of high river discharge but is almost vertically well mixed for periods of low river discharge particularly during spring tide conditions. (Fig. 3.5). The salt intrusion length has been monitored by USGS for several decades and is located approximately between 90

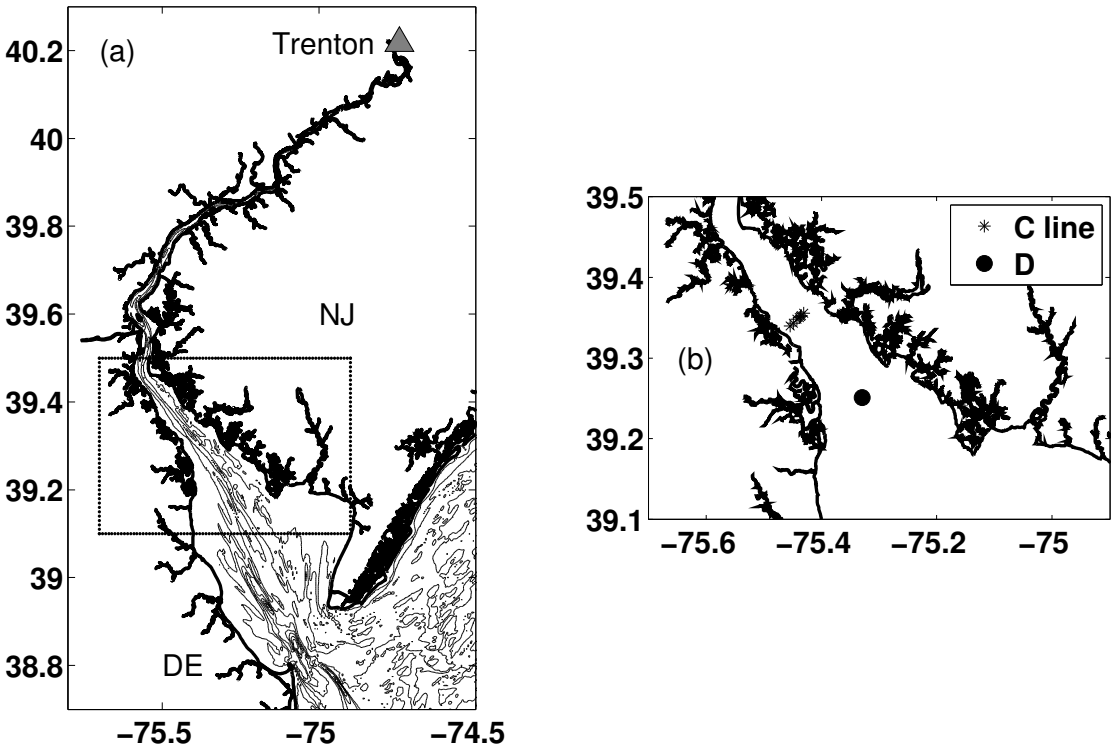

Figure 3.1: (a) Delaware Bay map with bathymetry contours. The location of Trenton, the head of the tides, is shown as a grey triangle. (b) Detail of Delaware Bay showing the location of the mooring array.

and 140 km from the entrance of the bay with a mean along-channel salinity gradient of 0.34 $1/km$ (Garvine *et al.* 1992).

Lateral variations of salinity are quite significant in this system an play and important role in its dynamics, as suggested by Wong (1994) and the analysis presented here. From observations, we obtained a cross-channel salinity gradient that fluctuates from about 1.0 ($1/km$) at the end of ebb tide to close to zero or small negative values at the end of flood tide (Fig 3.7 (d)). The flanks tend to be fresher than the main channel, with the Delaware side being the freshest due to the Coriolis acceleration trapping the outflowing water to the bay's southern shore.

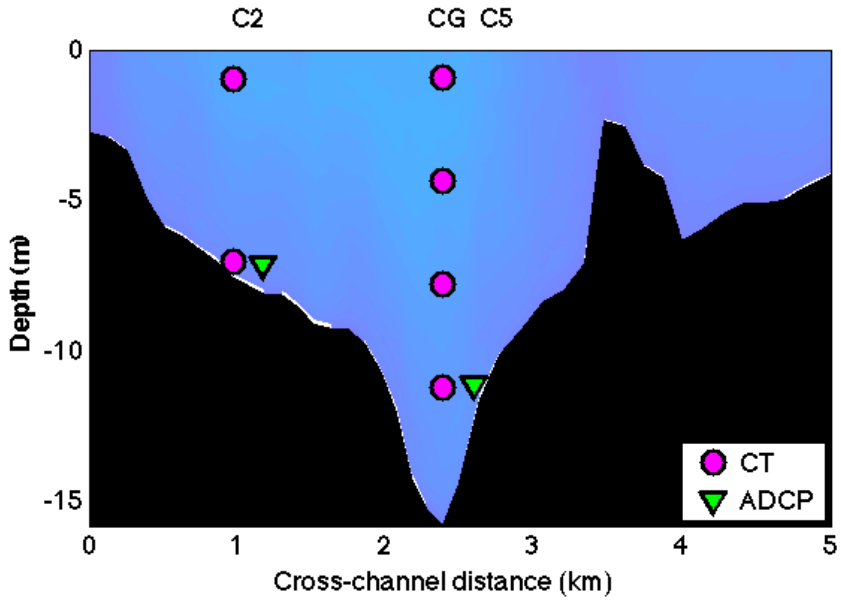

Figure 3.2: Cross-section of Delaware Bay at the C line (69 km from the entrance of the bay) showing the different instruments deployed at this location. In this figure the right flank is on the NJ side and the left flank on the DE side.

3.4 Field program

From April 8 to June 27, 2011 we deployed a mooring array in the middle reach of Delaware Bay, consisting of a 6 elements cross-channel array (C-line) and a single mooring (D-mooring) located at 68 km and 54 km respectively from the entrance of the bay (Fig. 3.1). This paper focuses on 3 of the moorings along the C-line: the C2 mooring with a bottom mounted ADCP of 1200 KHz and a surface and bottom CT sensor, the C5 mooring with a bottom mounted 1200 KHz ADCP, and a string of 4 CT sensors spanning the water column deployed from a Coast Guard Navigational Buoy (CG) (Fig. 3.2). The D mooring had a bottom mounted 600 KHz ADCP and a surface and bottom CT sensor. The ACDPs were programmed to acquire data for a period of 2 minutes at a rate of 1 Hz, every 10 minutes. These measurements were averaged for a total of 6 ensembles per hour. The resolution of the vertical bins was set to 0.5 m for the D mooring and 0.25 m for the C2 and C5 moorings. The CT sensors were programmed to acquire data at a rate of 1 sample every 10 minutes.

Additionally, two cross-channel tidal surveys (corresponding to periods of neap and

spring tide) were performed on the same location of the C line on April 13 and 19, 2011. The surveys consisted of hourly transects with a downward looking 1200 KHz ADCP over a period of 13 hours. Other instruments included a CT sensor and two OBS. These instruments were mounted in a cage that was manually lowered and provided measurements from the surface to within 2 m from the bottom with a horizontal resolution of about 130 m.

3.5 Methods

Principal component analysis was performed on the depth average velocities from the C5 mooring the vertical profile of velocity was accordingly rotated to find the along and cross-channel components. The velocities measured at C5 covered approximately 73% of the water column from 0.87 m above bottom to 2.9 m below the surface due to sidelobe interference with the surface. These velocity profiles were then extrapolated to the surface using a parabolic profile and to the bottom with a logarithmic profile with a bottom roughness of $z_0 = 0.04\ m$ above the bed. These full-water column velocity profiles were then converted into a terrain following coordinate system with 40 vertical levels. Additionally, a 3 hours lowpass filter was applied to all velocity and salinity data in order to eliminate high frequency variations when calculating the different terms in the salinity and momentum equations.

3.5.1 Potential energy anomaly and salinity equation

The potential energy anomaly and its time rate of change were calculated for the CG mooring following Simpson *et al.* (1990):

$$\phi = \frac{g\beta}{H}\int_0^H (\bar{s} - s)z dz \tag{3.1}$$

$$\frac{\partial \phi}{\partial t} = \frac{g\beta}{H}\int_0^H \left(\frac{\partial \bar{s}}{\partial t} - \frac{\partial s}{\partial t}\right) z dz \tag{3.2}$$

where g is the gravitational acceleration, β is the isohaline expansion coefficient, ρ_0 is the fresh water density, H is the total depth of the water column and 0 represents the surface, s is salinity at different depths, $\bar{s} = \frac{1}{H}\int_0^H s dz$ is the depth average salinity

and z is the depth at which the CT sensors are located. Defined this way, a negative ϕ means a stratified water column. The more negative ϕ is, the more stratified it becomes, thus, a negative $\partial\phi/\partial t$ means that stratification is being enhanced and a positive $\partial\phi/\partial t$ means that stratification is being reduced.

Meanwhile the salinity equation can be written as

$$\frac{\partial s}{\partial t} = -v\frac{\partial s}{\partial y} - u\frac{\partial s}{\partial x} - w\frac{\partial s}{\partial z} + \frac{\partial}{\partial z}\left(\frac{K_s \partial s}{\partial z}\right) \tag{3.3}$$

where v, u and w are the along-channel, cross-channel and vertical velocity respectively. $\partial s/\partial y$, $\partial s/\partial x$, $\partial s/\partial z$ are the along-channel, cross-channel and vertical salinity gradients. $\frac{\partial}{\partial z}\left(\frac{K_s \partial s}{\partial z}\right)$ is the time rate of change of salinity due to vertical mixing, and K_s is the vertical eddy diffusivity of salt. The along and cross-channel salinity gradients were calculated using the depth average salinity between the D and CG moorings and the CG and C2 moorings respectively.

Additionally, the along-channel velocity can be devided in three different components (MacCready 2011):

$$v_0(t) = \frac{1}{<H>}\left\langle \int v(z,t)\ dz \right\rangle \tag{3.4}$$

$$v_e(z,t) = \frac{\langle v\ dz\rangle}{<dz>} - v_0 \tag{3.5}$$

$$v_t(z,t) = v - v_e - v_0 \tag{3.6}$$

where the brackets $<\ \ >$ represent a low pass filter to remove oscillations at tidal time scales. We used a 32 hours Lanczos low pass filter with a 70 hour half window. Under this decomposition, v_0 represents the river discharge velocity but may include other contributions such as meteorological forced flows. v_e is the estuarine exchange flow and v_t is the tidal component of velocity. Then the depth dependent and the depth average salt equations can be expressed as:

$$\frac{\partial s}{\partial t} = -(v_0 + v_e + v_t)\frac{\partial s}{\partial y} - u\frac{\partial s}{\partial x} - w\frac{\partial s}{\partial z} + \frac{\partial}{\partial z}\left(\frac{K_s \partial s}{\partial z}\right) \tag{3.7}$$

$$\frac{\partial \overline{s}}{\partial t} = -(v_0 + \overline{v_t})\frac{\partial s}{\partial y} - \overline{u}\frac{\partial s}{\partial x} - \overline{w\frac{\partial s}{\partial z}} + \overline{\frac{\partial}{\partial z}\left(\frac{K_s \partial s}{\partial z}\right)} \tag{3.8}$$

where the overbar represents a depth average: $\overline{(\ )} = \frac{1}{H}\int_0^H (\ )dz$. Here we have used the fact the depth average of v_e is zero and have assumed that $\partial s/\partial y$ and $\partial s/\partial x$ are depth independent.

Then Eq. 3.2 can be expressed as follows:

$$\frac{\partial \phi}{\partial t} = \frac{g\beta}{H}\int_0^H (\underbrace{v_e \frac{\partial s}{\partial y}}_{\text{exchange}} + \underbrace{(-\overline{v_t} + v_t)\frac{\partial s}{\partial y}}_{\text{along-tidal}} + \underbrace{(-\overline{u} + u)\frac{\partial s}{\partial x}}_{\text{cross-tidal}} + \text{other terms}) z dz \tag{3.9}$$

where "other terms" represent the vertical advection and mixing contribution that can not be calculated directly with the available data. So $\frac{\partial \phi}{\partial t}$ written this ways allows us to estimate the contributions of horizontal advection to stratification. When calculating the different terms in Eq. 3.7, 3.8 and 3.9, $\frac{\partial s}{\partial y}$ was low passed but the tidal variability of $\frac{\partial s}{\partial x}$ was retained for reasons that will become apparent.

3.5.2 Momentum equation

The cross-channel momentum equation can be expressed as

$$\frac{\partial u}{\partial t} = -g\frac{\partial \eta}{\partial x} - \frac{g}{\rho_0}\frac{\partial \rho}{\partial x} z + fv + \frac{1}{\rho_0}\frac{\partial \tau_u}{\partial z} \tag{3.10}$$

where the advection terms have been neglected. The first two terms on the right side are the barotropic and baroclinic contribution of the cross-channel pressure gradient, fv is the Coriolis acceleration and the last term is the vertical stress divergence. We do not have an accurate estimate for the barotropic pressure gradient, but this term can be elimninated by subtracting the depth average cross-channel momentum equation from the depth dependent equation. This yields

$$\frac{\partial (u - \overline{u})}{\partial t} = -\frac{g}{\rho_0}\frac{\partial \rho}{\partial x}(z - \overline{z}) + f(v - \overline{v}) + \frac{1}{\rho_0}\left(\frac{\partial \tau_u}{\partial z} - \frac{\tau_0 - \tau_H}{H}\right) \tag{3.11}$$

where τ_0 and τ_H are the stresses at the surface and bottom respectively.

3.6 Results

3.6.1 Cross-channel tidal surveys

On April 13, 2011 at the beginning of the deployment period we performed the first cross-channel tidal survey during a period of neap tide and a river discharge at Trenton of 640 m^3/s. The tidal cycle survey provided a detailed view of the cross-channel structure of velocity and salinity and its variability over a tidal cycle. The first transect

shown in Fig. 3.3 (left panels) corresponds to the end of the ebb tide and presents a bottom to surface salinity difference of about 3 in the middle of the channel. Once the flood tide developed (Fig. 3.3, right panels), the stratification began to increase to a maximum value of 5. During the first half of the ebb tide (Fig. 3.4, left panels) the vertical stratification is again reduced to 3 and reaches its minimum value after maximum ebb (Fig. 3.4, right panels) with a value of 2. This tidal variability in stratification is contrary to the variability expected from tidal straining mechanism introduced by Simpson *et al.* (1990). The cross-channel flows had a significant spatial and temporal variability. The most important features of these flows is a clockwise circulation during the first half of the flood, two counterclockwise cells around maximum flood, and a very clear counterclockwise cell during the rest of ebb tide.

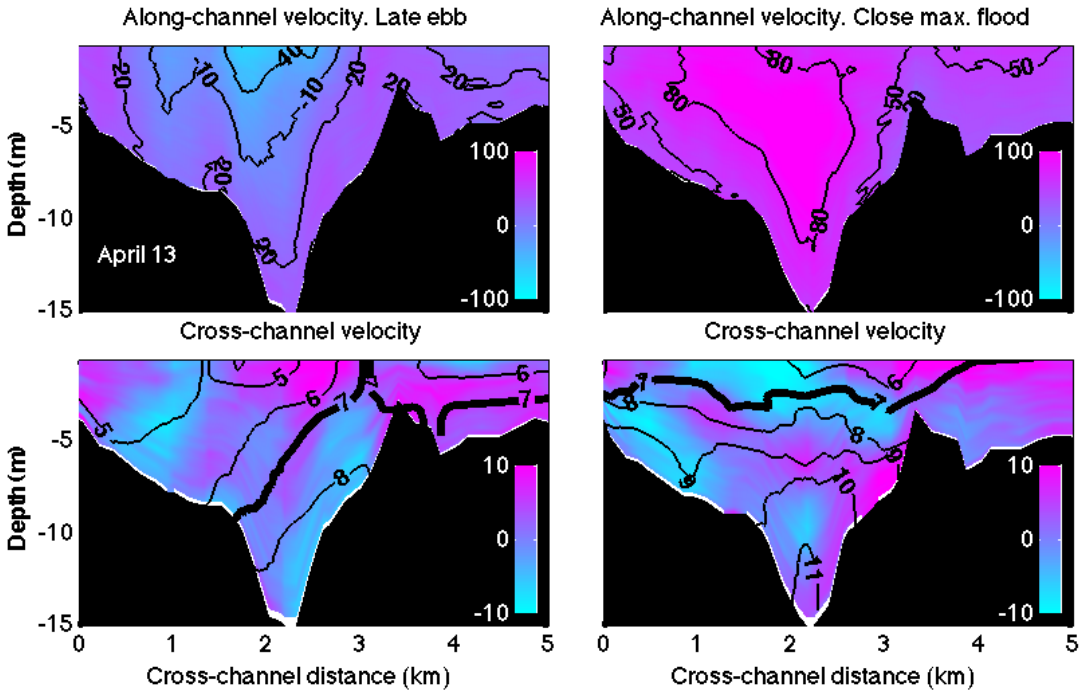

Figure 3.3: Cross-sectional transects from the tidal survey on April 13, 2011 at the beginning of the study period. The oceanward direction points out of the page. The upper panels correspond to contours of along-channel velocity with the color scale in cm/s and positive values indicating landward direction. The lower panels show contours of salinity over imposed on the cross-channel velocity in cm/s and positive values towards the right flank (NJ side). The first transect (left panels) took place towards the end of the ebb tide and the second transect (right panels) took place close to maximum flood.

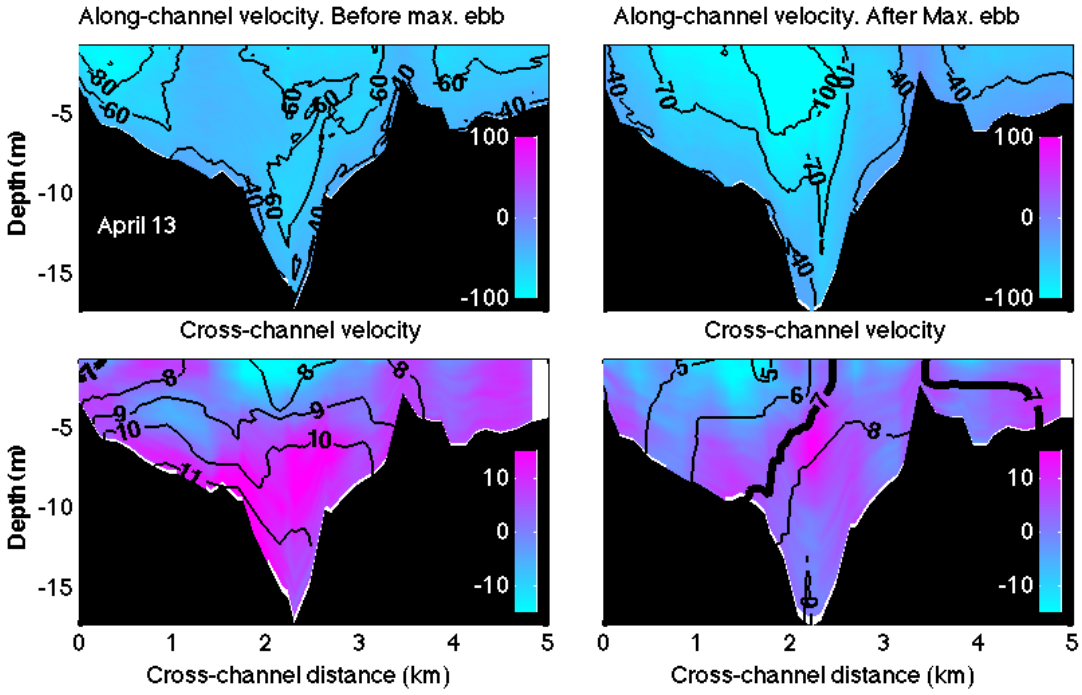

Figure 3.4: Cross-sectional transects from the tidal survey on April 13, 2011 at the beginning of the study period. The oceanward direction points out of the page. The upper panels correspond to contours of along-channel velocity with the color scale in cm/s and positive values indicating landward direction. The lower panels show contours of salinity over imposed on the cross-channel velocity in cm/s and positive values towards the right flank (NJ side). The first transect (left panels) took place before maximum ebb and the second transect (right panels) took place after maximum ebb.

This tidal cycle surveys illustrate how the action of the cross-channel flows affect the density field. At the end of the ebb, the isohalines are tilted and generate a strong cross-channel density gradient that forces the isohalines to adjust until they become horizontal towards maximum flood. Close to maximum ebb the isohalines remain flat, but there is a clear one cell circulation according with Coriolis forcing. This counterclockwise circulation strains the isohalines and, by the end of ebb, they again have a significant slope.

A similar tidal variability in stratification was also captured by the moored data. In what follows we will present further evidence for the tidal variability in stratification that we just described and we will try to understand more quantitively how the cross-channel flows bring about this variability and what are the underlying dynamics that

drive these cross-channel flows.

3.6.2 Stratification conditions

The bottom to surface salinity difference Δs from the CG mooring varied from a maximum of 8.5 to very close to zero (Fig. 3.5 (c)). The periods of high stratification corresponded to times of river discharge of around 1500 m^3/s and neap tides, while periods of low stratification coincided with times of the lowest river discharge of the deployment, $\sim$ 400 m^3/s, and spring tides. The first week of May is an exception to this stratification pattern: it is well stratified in spite of corresponding to a spring tide, but the river discharge is the highest of the observation period. For this reason, periods of low and high stratification were defined based on the average bottom to surface salinity difference Δs for the entire deployment rather than using tidal amplitude (i.e. spring/neap) as a proxi.

The values of Δs corresponding to the end of flood and the end of ebb tide are shown in Fig. 3.5 (d). For periods of high stratification, Δs is the largest at the end of flood tide and is significantly reduced at the end of ebb tide. On the other hand, during periods of low stratification Δs is either similar for these two tidal phases or larger at the end of the ebb tide.

The potential energy anomaly ϕ (Eq. 3.1), the total amount of work per unit volume required to completely mix the water column, is an equivalent way of estimating stratification (Fig. 3.6). The tidal phase average of ϕ shows again that the end flood is when the water column is more stratified for periods of high stratification.

3.6.3 Along and cross-channel salinity gradient

During the time of the deployment, the river discharge at Trenton had a maximum value of approximately 1744 m^3/s and a minimum of 228 m^3/s. The along-channel salinity gradient between the CG and D mooring, $\partial s/\partial y$, fluctuated around -0.45 $(1/km)$ (Fig. 3.7 (a)) and its low pass signal was highly correlated with river discharge (Fig. 3.7 (b)) with a maximum correlation of 0.76 for a lag of 3 days.

On the other hand, the cross-channel salinity gradient between the CG and C2

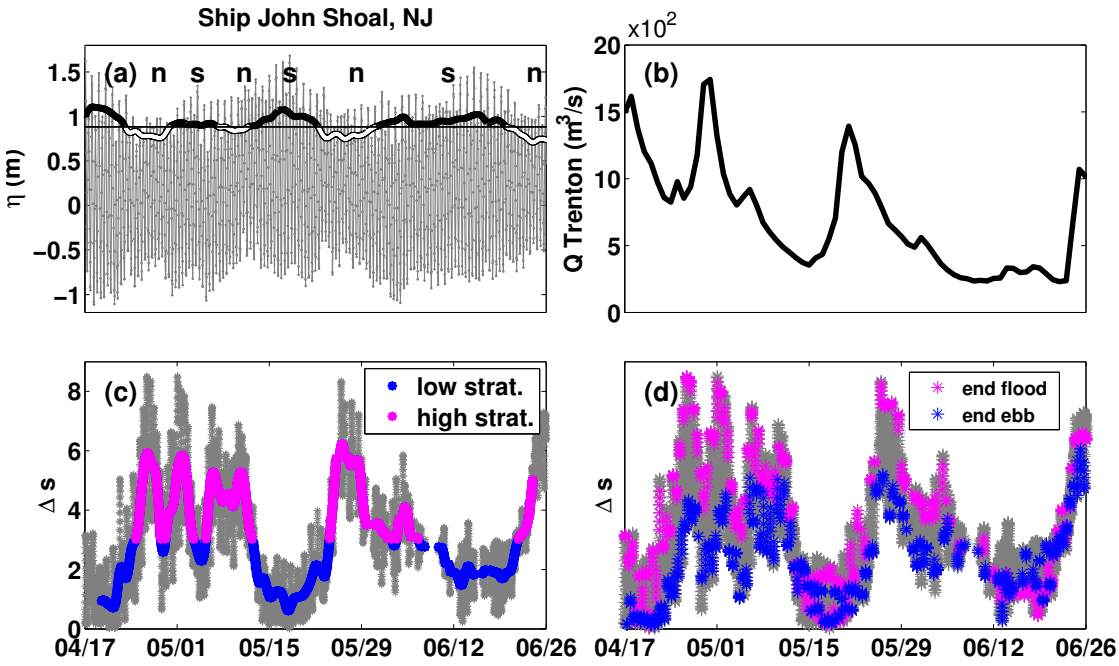

Figure 3.5: (a) Time series of mean sea level from the NOAA station at Ship John Shoal. The figure also shows periods of neap and spring time during the time of the deployment. (b) Delaware river discharge measured at Trenton (NJ). (c) Bottom to surface salinity difference Δs from the NG mooring (grey line) for the time of the deployment. The mean of the low pass signal of Δs is used to classify times of low stratification (cyan line) and high stratification(magenta line). (d) Δs from the NG mooring highlighting the Δs value for two tidal phases: end of flood (magenta) and end of ebb (cyan).

mooring, $\partial s/\partial x$, is significantly larger than $\partial s/\partial y$ and fluctuates between positive and negative values (Fig. 3.7 (c)) with greater positive values during periods of high stratification. When a tidal phase average is performed on $\partial s/\partial x$ (Fig. 3.7 (d)), we see that the positive values occur from maximum ebb through slack water and into the flood, as isohalines become vertical and the main channel becomes saltier than the left flank (Delaware side) during this phase of the tide. The cross channel gradient is near zero or weakly negative during the second half of the flood through the first half of the ebb as isohalines flatten. This tidal variability of $\partial s/\partial x$ plays an important role in the cross-channel dynamics as will be discussed later.

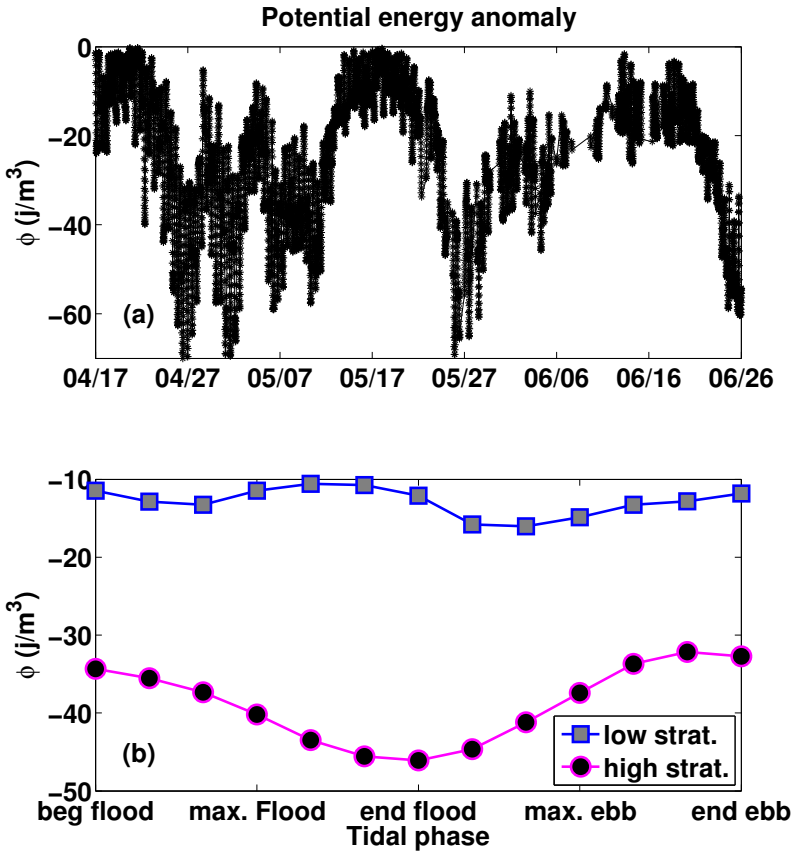

Figure 3.6: (a) Time series of the potential energy anomaly from the NG mooring. (b) Tidal phase averaging of the potential energy anomaly for times of high and low stratification.

3.6.4 Salt equation

The time rate of change of salinity, the along-channel advection, and cross-channel advection terms were calculated directly from this data set using the salinity data from the CG mooring and velocity profiles from the C5 mooring.

The depth average salt equation (Fig. 3.8 (a)) shows that there is a close balance between $\frac{\partial \overline{s}}{\partial t}$ and $-\overline{v_t}\frac{\partial s}{\partial y}$, meaning that in a depth average sense the time rate of change of salinity is caused primarily by the along channel advection of the tidal flows. The term $-v_0\frac{\partial s}{\partial y}$ is very close to zero considering that v_0 is about one order of magnitude smaller than v_t. Additionally, $-\overline{u}\frac{\partial s}{\partial x}$ is also quite small because the depth average cross-channel flow is close to zero in the middle of the main channel, consisting with a closed cell.

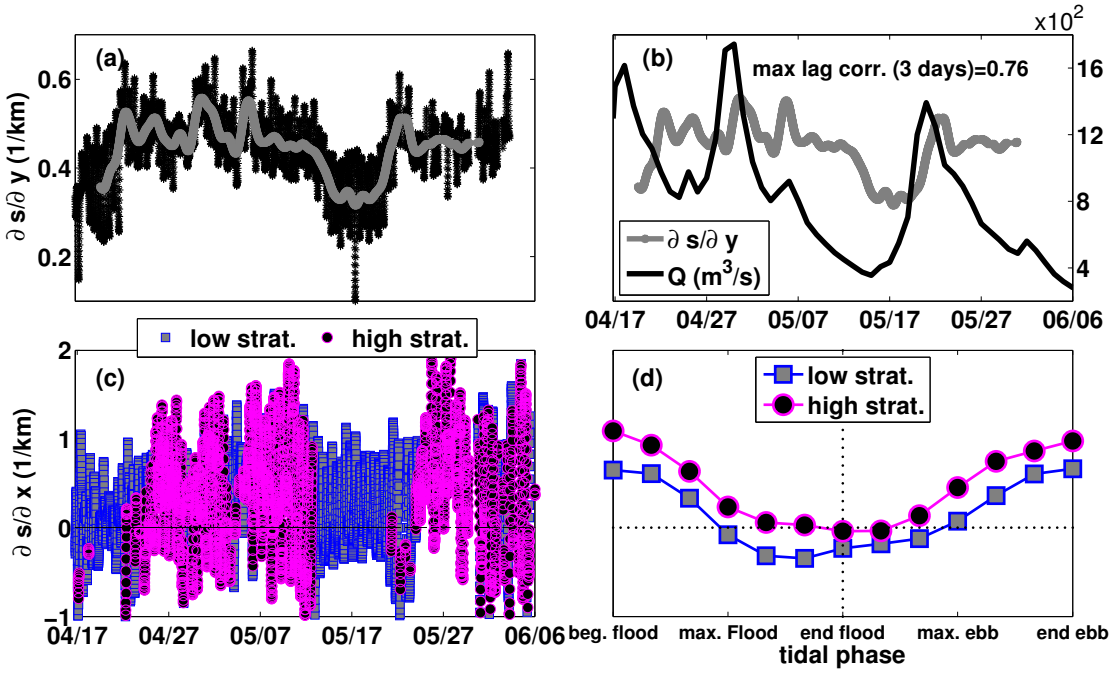

Figure 3.7: (a) Time series of the along-channel salinity gradient (black line) and its low pass signal (grey line). (b) Delaware river discharge at Trenton along with the low pass of the along-channel salinity gradient. They have a maximum correlation of 0.76 for a time lag of 3 days. (c) Time series of the cross-channel salinity gradient at the location of the C line. The black and grey lines show times of low and high stratification respectively. (d) Tidal phase averaging of the cross-channel salinity gradient for times of high and low stratification.

The depth dependent salt equation shows that the cross-channel advective term is significant at times 1 meter from the surface (Fig. 3.8 (b)), but is negligible at 8 meters depth (Fig. 3.8 (c)). The terms $-v_e\frac{\partial s}{\partial y}$ and $v_0\partial s/\partial y$ are also negligible considering that the v_0 and the subtidal velocity are one order of magnitude smaller than v_t. The sum of the along and cross-channel advective terms does not equal the time rate of change of salinity, especially close to maximum ebb and flood tide. This implys that the vertical mixing term is quite important in the salinity balance during these periods.

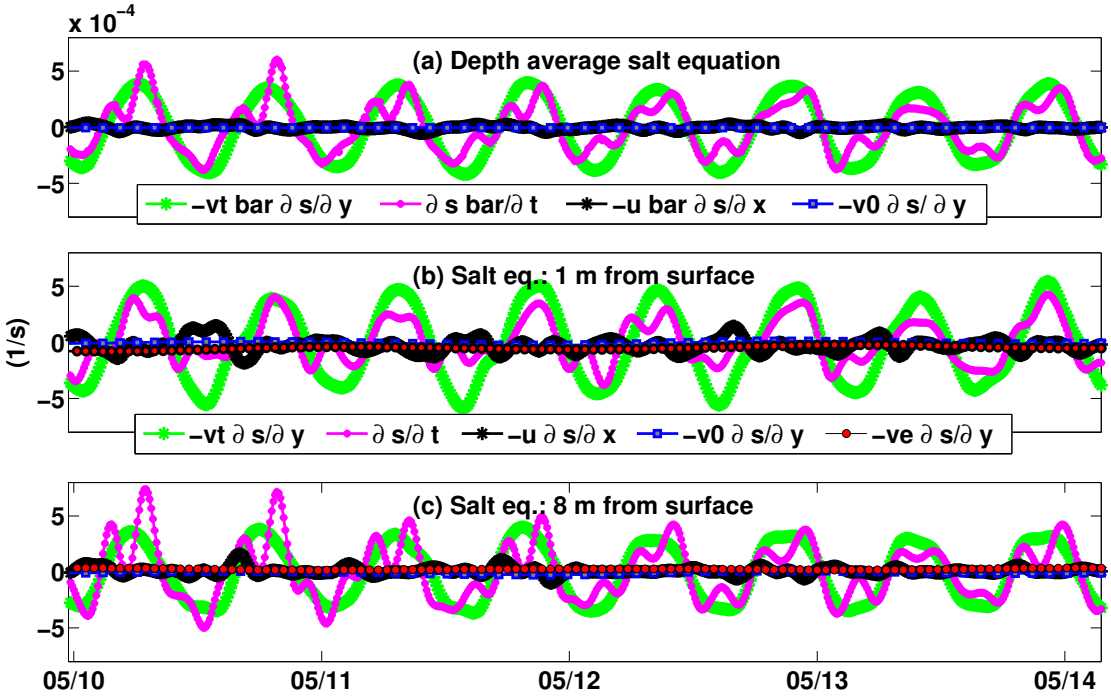

Figure 3.8: Detail of the time series of the salt equation between March 10 and 12, 2011. (a) Depth average salt equation (Eq. 3.8). (b) Salt equation (Eq. 3.7) at 1 meter below the surface. (c) Salt equation (Eq. 3.7) at 8 meter below the surface.

3.6.5 Time rate of change of the potential energy anomaly

$\partial\phi/\partial t$ (Eq. 3.9) is expressed as different contributions: subtidal, along-tidal, cross-tidal and "other terms". The subtidal term expresses the contribution of the estuarine circulation to stratification. The along-tidal term represents the contribution of the shear in the along-channel tidal velocity, which corresponds to the tidal straining mechanism introduced by Simpson *et al.* (1990). Likewise, the cross-tidal term can be interpreted as the effect that the shear in the cross-channel flows have on vertical stability.

The time series of $\partial\phi/\partial t$ (Fig. 3.9) shows that the along-tidal and cross-tidal contribution to stratification have similar magnitudes and that the along-channel subtidal contribution is smaller but not insignificant. This contrasts with the relatively small contributions that the cross-channel and subtidal advection have in the depth dependent salinity equation. This emphasizes the importance of using a depth integrated quantity as the potential energy anomaly.

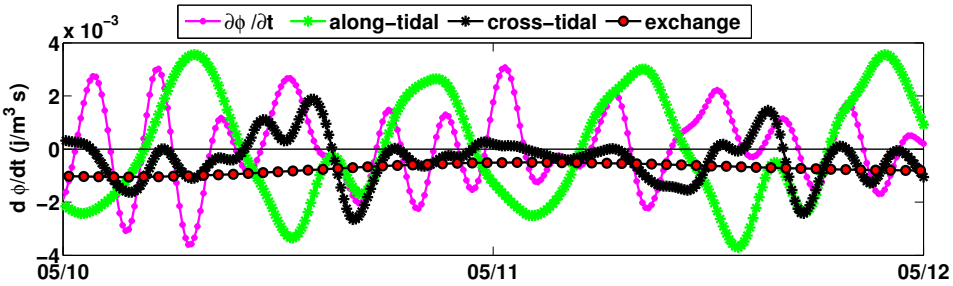

Figure 3.9: Detail of the time series of the time rate of change of the potential energy anomaly as shown in Eq. 3.9 between March 10 and 12, 2011.

A tidal phase averaging is performed on the different advective contributions of $\partial\phi/\partial t$ in addition to dividing this tidal phase averaging into times of low and high stratification (Fig. 3.10). We noted that the along-channel tidal contribution has a de-stratifying action during most of the flood (positive $\partial\phi/\partial t$) and a stratified effect during ebb tide (negative $\partial\phi/\partial t$), consistent with the tidal straining mechanism. The subtidal component has always a stratifying action corresponding to a two layers exchange flow, so it is enhanced during periods of high stratification. On the other hand, the cross-channel component tends to stratify during first half of the flood and de-stratify at the end of the ebb for both periods of low and high stratification competing with the along-channel tidal contribution. Moreover, during highly stratified conditions, the sum of the along channel terms are smaller during flood (primarily due to the enhanced straining by the mean flow) and thus, the lateral straining term overcomes these terms and tends to increase stratification during the flood tide.

3.6.6 Cross-channel dynamics

The cross-channel flows have an important influence on the tidal variability of stratification, and therefore we next diagnose the lateral momentum budget to understand what is driving the cross-channel flows and how they affect the density field.

The cross-channel flows from mooring C5 (Fig. 3.11) consist mostly of a single circulation cell throughout most of the tidal cycle. During the beginning of flood the circulation is clockwise (i.e. bottom flows towards Delaware), but before maximum

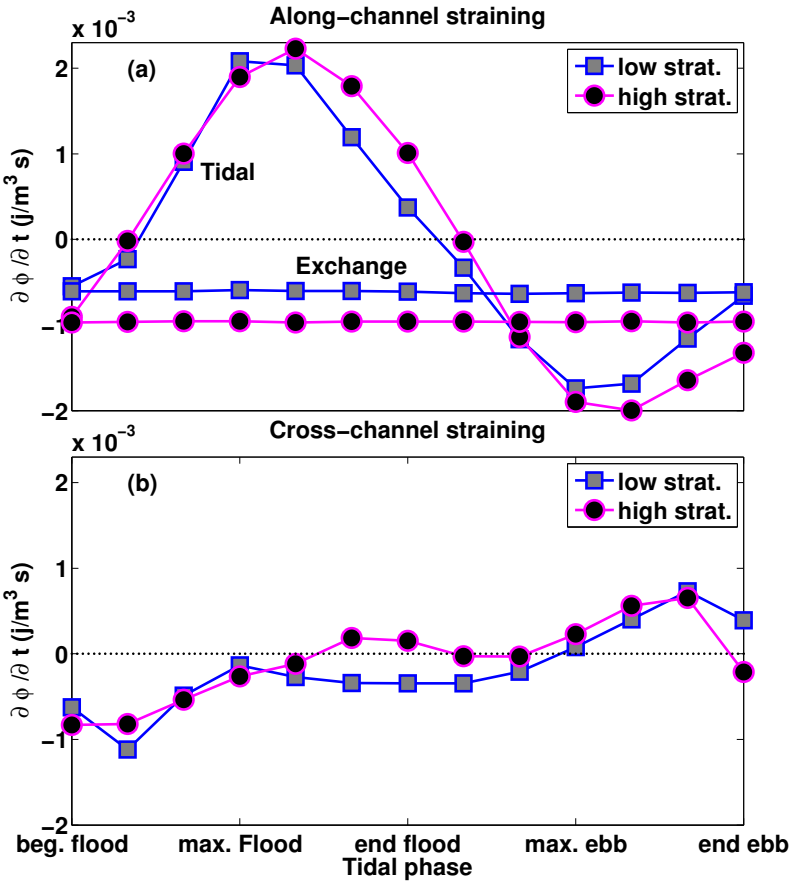

Figure 3.10: Tidal phase averaging of (a) "along-tidal" and "subtidal" terms and (b) "cross-tidal" term of $\partial\phi/\partial t$ (Eq. 3.9) for times of high and low stratification.

flood the lateral flows begin to weaken and eventually flow clockwise, with particularly swift surface currents flowing towards the Delaware side at the beginning of ebb. During maximum ebb, lateral flows show a hint of a three-cell system during highly stratified conditions, but remain primarily a single cell with surface flows towards Delaware and bottom/mid-water column flows towards New Jersey. Note that lateral flows for both phases of the tide are maximum at the surface around slack water, which we interpret to be due to lateral gravitational adjustment of a cross-channel density gradient set up during the previous phase of the tide. To assess this interpretation, we then analyze the cross-channel dynamics.

Terms in Eq. 3.11 that describe the tendency to drive cross-channel shear are shown in Fig. 3.12. Near the surface, the cross-channel baroclinic term and the Coriolis are

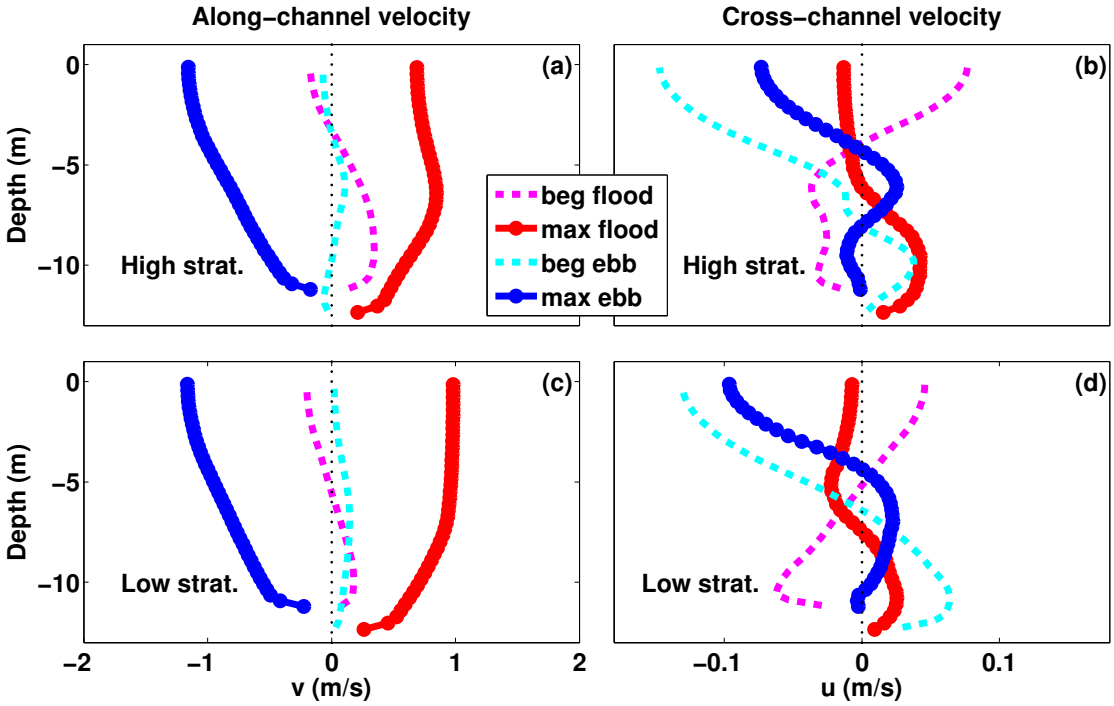

Figure 3.11: Tidal phase averaging of (a) and (c) along-channel velocity and (b) and (d) cross-channel velocity for times of high and low stratification.

of opposite sign; however, they do not balance, as evidenced by the prominence of the acceleration term. In the lower layer the Coriolis term dominates, suggesting the likely importance of the stress divergence, which we do not estimate.

A tidal phase averaging of Coriolis and the cross-channel baroclinic pressure gradient provides insight into how these two forces drive the cross-channel circulation. The Coriolis term $f(v - \overline{v})$ (Fig. 3.13 (a)), driven by the shear in the along channel flow, is stronger during the ebb than during the flood. During the flood, vertical shear in the along channel flow is largely confined to the bottom boundary layer and thus, at the bottom, the Coriolis term is negative and accelerates the fluid towards the left (DE). At the surface, Coriolis weakly drives a circulation in the opposite direction except during the first two hours of the flood tide when there is a lag between the time the surface and bottom along-channel vertical shears change sign. During the ebb, the Coriolis term drives lateral flows in the opposite direction with the lower layer accelerated towards the NJ shore and the upper layer towards the DE shore.

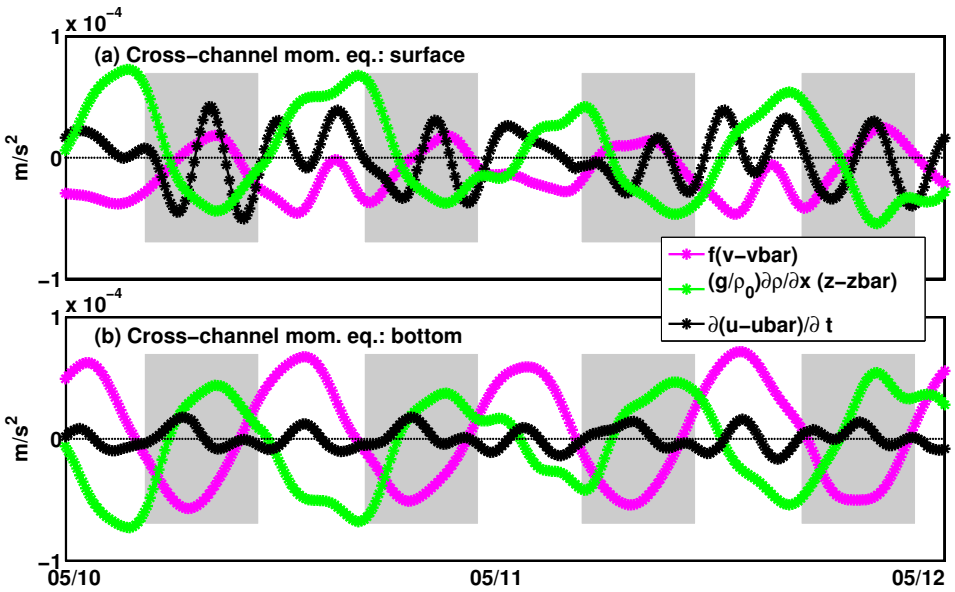

Figure 3.12: Detail of the time series of the cross-channel momentum equations as expressed in Eq. 3.11 between March 10 and 12, 2011 for (a) surface and (b) bottom. The shaded areas represent periods of flood tide.

The cross-channel baroclinic term (Fig. 3.13 (b)) changes sign halfway through each tidal cycle: it is positive at the surface during the first half of the flood because the main channel is saltier than the flanks but changes to negative during the second half of the flood and through the first half of the ebb and then back to positive during the last half of the ebb. Note that the sign of the cross-channel salinity gradient during the second half of the flood is inconsistent with differential advection, which continues to increase the cross-channel salinity gradient throughout most of the flood tide. This fluctuation in the cross-channel density gradient is caused by the straining of the salinity field by the cross-channel flows during the ebb and the subsequent adjustment during the flood.

The tidally mean state of the cross-shore salinity gradient in Delaware Bay is characterized by a coastal current with fresher, more stratified fluid found along the bay's Delaware coast and more saline and mixed conditions along the New Jersey Coast (Aristizábal and Chant, 2013). During the early flood, tide lateral flows tend to "up-well" this coastal current and increase stratification while the reverse flows during the ebb

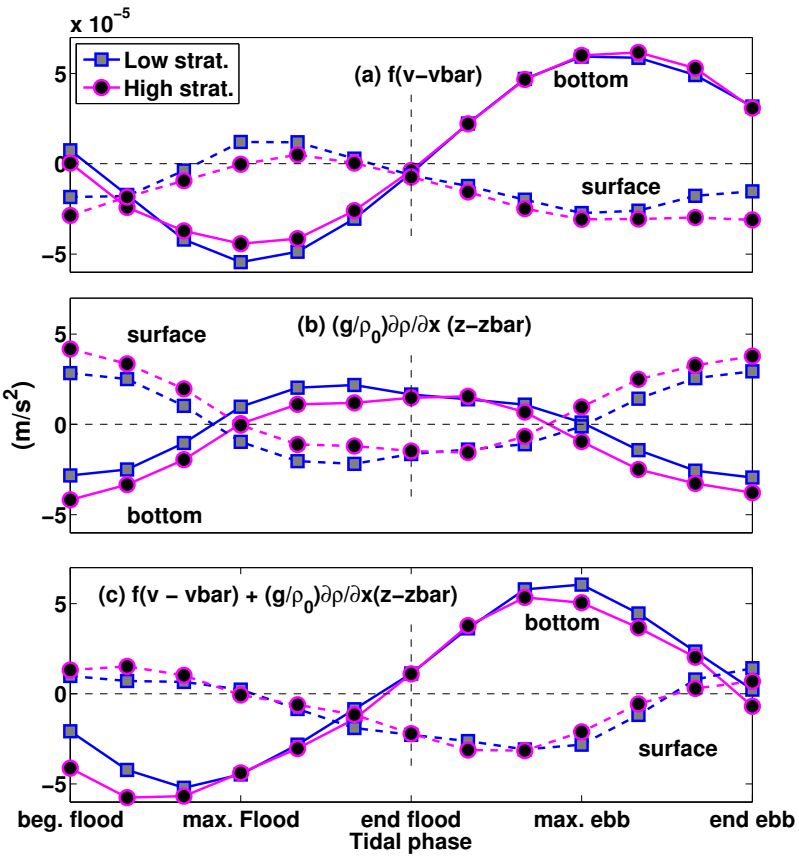

Figure 3.13: Tidal phase averaging of (a) Coriolis minus its depth average, (b) cross-channel baroclinic pressure gradient minus its depth average and (c) the sum of (a) and (b), for times of high and low stratification.

"down-well" the coastal current producing vertical isohalines and weakly mixed conditions. Superimposed on this, of course, is the action of the along channel flow that tend to produce the opposite tidal period variability and mixing which weakens stratification following peak flows. During low stratification periods the cross-channel salinity field is relatively homogenous and lateral straining is overcome by both along-channel straining, which produces stronger stratification at the end of ebb, and vertical mixing, which overcomes lateral straining during flood, and the water column becomes mixed (Fig. 3.5 (d)).

The cross-channel circulation is consistent with the circulation driven by the combination of Coriolis and cross-channel pressure gradient (Fig. 3.13 (c)). During the first

half of flood the circulation is clockwise, but during the second half, the circulation consists of a weak counterclockwise circulation. The reason for this is that the Coriolis acceleration is relatively weak at the surface because the shear in the along channel velocity is weak in the upper 6 m of the water column (Fig. 3.11 (a) and (c)). When this weak Coriolis force is combined with the cross-channel baroclinic pressure gradient, which drives a circulation towards the left at the surface, baroclinicity overcomes Coriolis. During the first part of ebb, both the baroclinic and Coriolis term work together (Fig. 3.13 (a) and (b)) to produce strong near-surface cross-channel flows during the early ebb. However, during the final phase of the ebb the DE flank becomes fresher than the main channel and as a result the cross-channel baroclinic term opposes Coriolis and reverses the lateral flows.

A tidal phase averaging of $\partial v/\partial z$ at mid depth and $(g/\rho f)\partial\rho/\partial x$ shows that a thermal-wind balance holds only during the first half of flood tide (Fig. 3.14). This implies that during this period the cross-channel flows (at mid depth ($\sim$ 5 m)) do not experience any acceleration and corresponds to the location where the lateral flows change sign (Fig. 3.11 (b) and (d)).

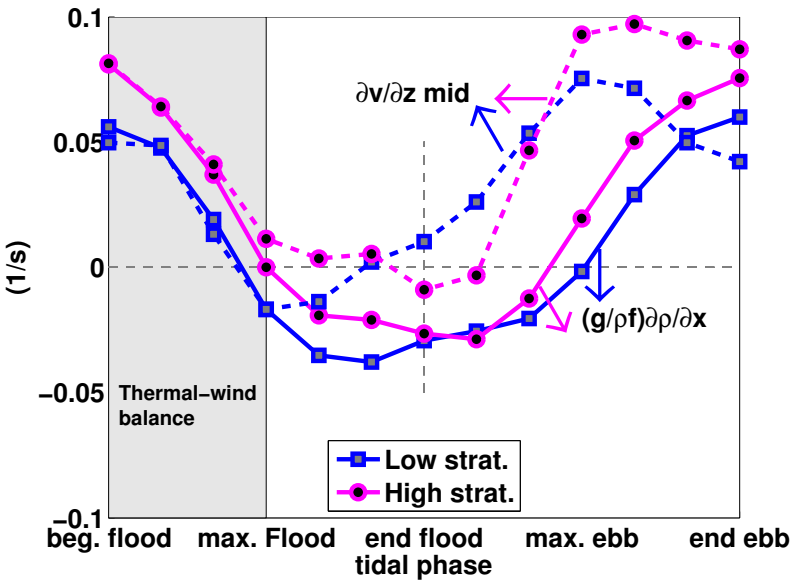

Figure 3.14: Tidal phase averaging of $(g/\rho f)\partial\rho/\partial x$ and $\partial v/\partial z$ (at mid depth) for times of low and high stratification.

This circulation pattern, along with the tidal variability in the cross-channel density gradient and stratification, are depicted in Fig. 3.15; This shows enhanced stratification throughout the flood and weakening stratification toward the end of ebb. During weakly stratified conditions this cartoon would be modified by mixing, which would weaken stratification around both maximum flood and maximum ebb.

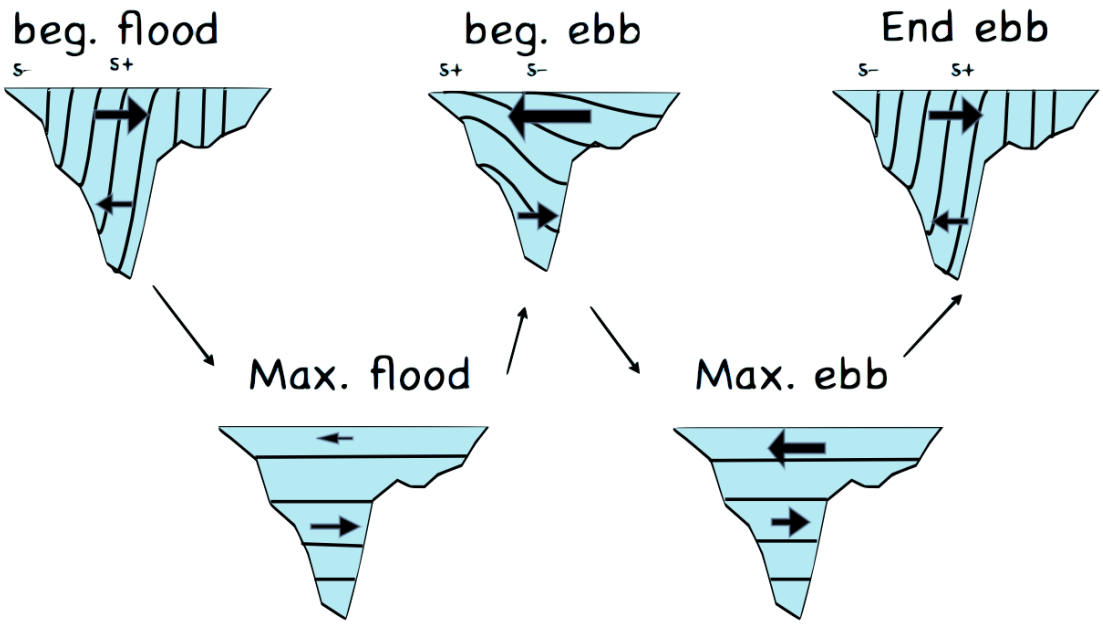

Figure 3.15: Cartoon depicting the cross-channel circulation and salinity field for different tidal phases. The oceanward direction is out of the page.

In conclusion, the observed cross-channel circulation is driven by the interplay between Coriolis and the cross-channel baroclinic pressure gradient, which is itself modified by the cross-channel flows.

3.7 Discussion

Tidal oscillatory salt flux (TOSF) is zero when tidal period salinity and velocity fluctuations are in quadrature. During such conditions, maximum salinity occurs at the end of flood, minimum salinity coincides with the end of ebb, and tidal motion yields no net salt flux. Tidal period salinity and velocity fluctuations are in quadrature when the time rate of change in salinity is driven solely by the along channel advection of the

along channel salinity gradient, i.e.

$$\frac{\partial s_t}{\partial t} = -v_t \frac{\partial s_t}{\partial y} \tag{3.12}$$

where s_t and u_t are the tidally varying salinity and along channel velocity. Thus, if u_t is harmonic, i.e. $u_t \propto \sin(\omega t)$, s_t is 90 degrees out of phase, i.e. $s_t \propto \cos(\omega t)$, and the tidally averaged flux is zero. However, as other terms in the salt budget equation become important, such as the lateral advection of salt and mixing processes, s_t and u_t become out of quadrature and a net salt flux occurs.

Observations presented here and in modeling results (Aristizábal and Chant, 2013) reveal that secondary flows play an important role in determining the tidal period variability in salinity and driving the phase relationship between salinity and velocity out of quadrature resulting in a net upstream TOSF. In addition, the modeling results indicate that TOSF increases with increasing stratification. TOSF is proportional to stratification because as stratification increases, lateral circulation produces larger tidal period variability in s_t, and thus the tidal cycle average of the product of $u_t s_t$ is larger. However, stratification increases with decreasing tidal current speed and thus TOSF is largest during neap tide and weakest during spring tide in contrast to existing parameterizations of TOSF, which suggest that it increases with increasing tidal current speed (Banas *et al.* 2004 and MacCready 2007). This discrepancy is probably due to the large spring neap variation in stratification that occurs in Delaware Bay.

The observed cross-channel flows have similar magnitudes during flood and ebb tides and for periods of high and low stratification (Fig. 3.11). This time variability also contrasts with previous observational (Chant 2002) and modeling (Lerczak and Geyer 2004) studies. However, both these previous studies occurred in much narrower systems, and thus the effects of the earth's rotation may be more prominent in the wider Delaware Bay. Moreover, numerical modeling results in Cheng *et al.* (2009) revealed that the inclusion of a turbulence closures scheme, in contrast to the constant eddy viscosity in Lerczak and Geyer (2004), increased the strength of lateral flows during stratified conditions.

Both the observations presented here and recent modeling results (Aristizábal and Chant, 2013) indicate that lateral circulation in Delaware Bay is driven primarily by the Coriolis acceleration and that the phasing of this term is similar to that of the along channel flows and largest around maximum currents with sign reversal around slack water. In contrast, the cross-channel baroclinicity tends to change sign around maximum current and thus augments the Coriolis forcing as tidal currents accelerate, but competes with the Corioils as tidal currents decelerate. The interplay of these two terms result in a maximum cross-channel flows around slack water and relatively weak secondary flows after peak tidal currents. Furthermore, the cross-channel baroclinic pressure gradient is somewhat enhanced during periods of high stratification, but so is the vertical shear in the along channel flow. As a result the observed lateral circulation is slightly increased during strongly stratified periods. In addition the reduction of stress during highly stratified times would also augment lateral circulation.

While we did not make an estimate of the contribution of differential advection to the cross-channel baroclinic pressure gradient, the tendency for this term to change signs during peak current and in particular for the main channel to become fresher than the flank on the last part of flood (and visa-versa on ebb) indicates that differential advection is not the dominant mechanism behind the tidal period variability in the cross-channel salinity gradient. Instead, it is the process of straining of the cross-channel salinity gradients by the secondary flows and the subsequent readjustment of he buoyancy that determines the tidal period variation in the cross-channel density gradient.

Analysis of tidally averaged momentum equation presented in both Lerczak and Geyer (2004) and Scully *et al.* (2009b) suggests that non-linear advection associated with lateral circulation rectify the estuarine exchange flow. However, the tidal rectification they describe relies on specific tidal and spring/neap variability in the lateral flows, which is not evident in this study. While it is possible that the lateral flows observed here also rectify the exchange flow, the fact that their tidal period variability differs dramatically from those studies suggests that investigation of the tidal rectification by lateral flows in wider estuaries is warranted.

Finally, the lateral flows likely play an important role in the transport of sediment from the main stem to the fringes of the estuary (Sommerfield and Wong 2011). This process is likely important for the accretion of salt marshes and, in particular, their ability to keep up with sea-level rise. While a number of factors have contributed to the loss of salt marshes in recent decades, lack of sediment supply is among the predominate causes (Deegan *et al.* 2012) Like many estuaries world-wide, the Delaware Bay has undergone significant channel deepening to accommodate the ever-increasing draft of the international shipping fleet. It is likely that this deepening has modified the strength and variability of the lateral flows and thus altered the net flux of sediment delivered to the marshes, and potentially limiting the marsh's ability to accrete at a rate to keep up with sea-level rise.

3.8 Conclusions

Stratification in the middle reach of Delaware Bay is characterized by a reduction of the bottom to surface salinity difference during ebb tide and an increase during the flood tide for periods of high stratification. This tidal variability in stratification is contrary to the tidal variability predicted by the tidal straining mechanism introduced by Simpson *et al.* (1990).

An analysis of the time rate of change of the potential energy anomaly reveals that there is a competition between the along- channel tidal straining, which stratifies the water column during the ebb and de-stratifies it during the flood and the straining caused by the cross-channel flows that tends to have an opposite effect.

The shear in the cross-channel flows strains the salinity field during ebb, causing the isohalines to tilt upwards and reduce stratification. This creates a strong cross-channel density gradient that relaxes during the flood tide and causes the isohalines to become horizontal and enhance vertical stability.

During periods of low stratification, lateral straining is overcome by the along-channel straining and by vertical mixing during peak velocity periods.

The cross-channel dynamics show that the lateral flows are driven by the combination of Coriolis and cross-channel pressure gradient. During the flood tide, Coriolis and the cross-channel pressure gradient tend to oppose each other, creating a clockwise circulation that only persists during the first half of the flood. The circulation reverses around maximum flood and remains a counterclockwise cell for the rest of the ebb tide due to the fact that Coriolis and cross-channel pressure gradient work together during the first half of the ebb.

3.9 Acknowledgements

We thank Eli Hunter, Chip Haldeman, Joe Jurissa, Dove Guo and the captain of the ship Ken Roma for all their dedication collecting the data. This work was supported by a National Science Foundation grant OCE-0928567 and OCE-0825833. The author María Aristizábal was supported by a Dupont fellowship and the Institute of Marine and Coastal Sciences at Rutgers University. We also thank Jack McSweeney for closely reading the manuscript.

Chapter 4

Area integrated salt fluxes: an observational study

4.1 Introduction

Dispersion in estuaries determines the fate and distribution of materials such as contaminants, sediments, organic-carbon, nutrients, among others. The dispersion of salt from the ocean into the estuary is of particular interest, because it determines the along-channel distribution of salinity, which in part controls the strength of the gravitational circulation. In turn, this gravitational circulation is one of the main mechanisms that bring salt into the system and thus points to the strong interplay between estuarine dynamics and dispersion.

The transport of salt into estuaries can be differentiated into a seaward salt flux due to the river outflow, a landward salt flux driven by the estuarine exchange flow, called steady shear dispersion, and the tidal oscillatory salt flux, induced by the tidal flows. The tidal oscillatory salt flux is usually landward but may contribute to oceanward transport of salt.

The steady shear dispersion is relatively a well understood mechanism. Its has a time variability with more accentuated values during neap tide, due to an increase in vertical stratification, and smaller values during spring tide, when vertical stratification is hindered by mixing. In some systems, like the Hudson River (Lerczak *et al.* 2006), steady shear dispersion is the dominant mechanism.

However, there are other systems in which the tidal oscillatory salt flux is as important or more dominant than steady shear dispersion (San Francisco Bay (Conomos 1979), Mersey estuary (Oey 1984), Merrimack River (Chen *et al.* 2012)). It is then pertinent to understand what are the main drivers of the salt fluxes at tidal time scales.

Fisher *et al.* (1979) introduced the oscillatory shear dispersion as the mechanism responsible for dispersion at tidal time scales. According to this mechanism, the vertical or cross-channel shear in an oscillatory flow, differentially advects fluid parcels, that are subsequently dispersed through vertical or lateral mixing.

Zimmerman (1986), building on the seminal work of Okubo (1973), proposed a different mechanism, in which along-channel dispersion is a result of the complex bathymetry, which induces highly irregular velocity fields, hence, greatly variable residual flows.

Banas *et al.* (2004) suggested a scaling for the along-channel dispersion coefficient given by: $K_H = c_k U_T B$, where c_k is a proportionality constant, U_T is the root mean square of the tidal velocity and B is the width of the channel. This parameterization can be interpreted as a dispersal mechanism that is achieved by residual eddies, with a mean current equal to a fraction of the tidal velocities: $c_k U_t$, and with a maximum length equal to the width of the channel (Banas *et al.* 2004). Later, MacCready (2007) expanded the previous parameterization by including the tidal excursion length (L_t) as possible limiting factor for the size of the eddies: $K_H = c_k U_T min(B, L_t)$. In addition MacCready (2007), based on the ideas of Stommel and Farmer (1952), proposed a K_H that is enhanced at the entrance of the system, due to the efficient tidal exchange between estuarine and oceanic waters.

According to this parameterization for K_H, the dispersion of salt at tidal time scales should be enhanced during spring tides due to stronger tidal velocities. However, Aristizábal and Chant (2013), in a numerical study of the salt fluxes in Delaware Bay, found that the tidal oscillatory salt flux had a variability that is contrary to aforementioned parameterization. They proposed an alternative scaling for the along-channel dispersion coefficient that involves the amplitude of the tidal velocities, as well as the strength of stratification.

In this chapter, we use observations in Delaware Bay to calculate the different components of the area-integrated salt fluxes following the methods by Lerczak *et al.* (2006). The estimate for the along-channel dispersion coefficient from this analysis is partially consistent with the proposed parameterization by Aristizábal and Chant (in

press).

4.2 Field program

From Jun 29 to August 10, 2011, we deployed a mooring array in the middle reach of Delaware Bay consisting of 7 elements, located 68 km from the mouth (C-line). In addition, a single mooring (D mooring), located 54 km from the entrance of the bay, was also deployed in the middle of the channel (Fig. 4.1).

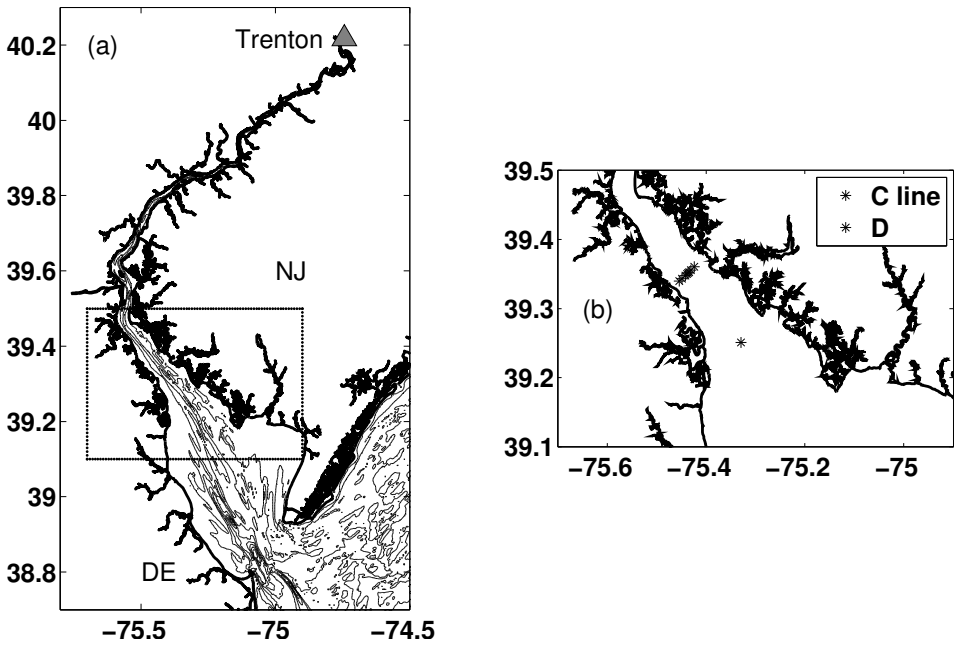

Figure 4.1: (a) Delaware Bay map with bathymetry contours. The location of Trenton, the head of the tides, is shown as a grey triangle. (b) Detail of Delaware Bay showing the location of the mooring array.

Seven of the eight moorings: C1-C6 and D (Fig. 4.2), had a bottom mounted 1200 KHz ADCP that were programmed to acquire data for a period of 2 minutes, at a rate of 1 Hz every 10 minutes. The resolution of the vertical bins was set to 0.25 m for moorings C1 to C6, and to 0.5 for the D mooring. The C7 mooring was mounted with a 300 KHz ADCP. It was programed to acquire 3 ensembles per hour and had a vertical bin resolution of 0.5 m.

All the moorings had bottom conductivity-temperature sensors, but only the moorings with surface expression: C1, C2, C6 and C7 had surface CT sensors. The moorings

closer to the navigational channel were equipped with acoustic releases, due to the heavy ship traffic in Delaware Bay. We took advantage of a Coast Guard Navigational moorring (CG), in the middle of the channel, to deploy a surface and mid-depth CT sensor. All the conductivity-temperature sensors were programmed to acquire data at a rate of 1 sample every 10 minutes.

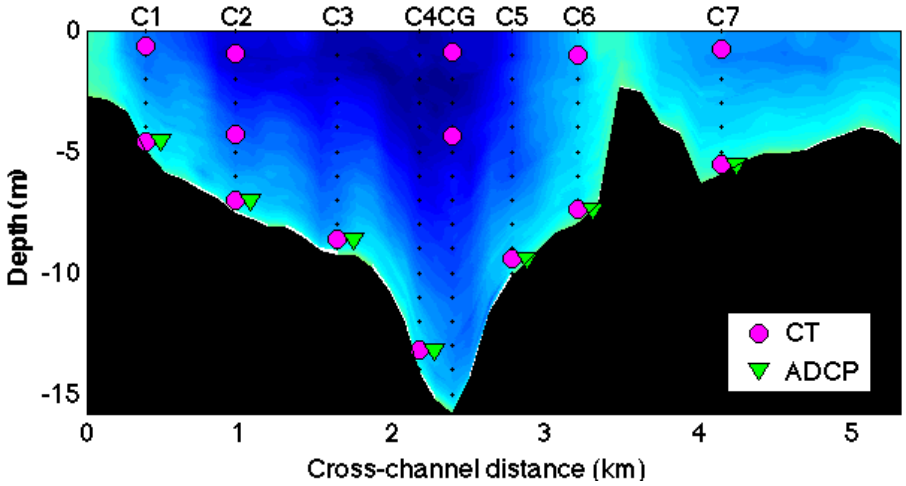

Figure 4.2: Cross-section of Delaware Bay at the C line (69 km from the entrance of the bay) showing the different instruments deployed at this location. In this figure the right flank is on the New Jersey side and the left flank on the Delaware side.

Additionally two cross-channel tidal surveys were performed along the C line on July 28 and August 4, 2011, corresponding to periods of neap and spring tide respectively. The surveys consisted of hourly transects with a downward looking 1200 KHz ADCP over a period of 13 hours. Other Instruments included a RBR CT sensor, two D & A Optical Back Scatter, an Aanderaa optode oxygen sensor and a Satlantic Ultraviolet Nitrate Anylizer (SUNA) sensor. These instruments were mounted into a cage that was attached to a tow-yo'd system. It provided measurements from the surface to within 2 m from the bottom with a horizontal resolution of about 60 m.

4.3 Methods

We followed the methods described by Lerczak *et al.* (2006) in order to calculate the area-integrated salt fluxes. The first step in this calculation was to divide the cross-sectional area into 6×3 regions for a total of 18 regions (Fig. 4.3). These regions are

quadrilaterals in order to better match the shape of the cross-sectional area. The depth of each region expands or contracts according with the total depth of the water column. The center of the bottom boxes correspond to the location of the ADCPs and bottom CT sensors. The surface CT sensors are located in the middle of the boxes closest to the surface. The velocity measurements from the C2 mooring were not included, because the ADCP and bottom CT sensor were covered by mud very early in the deployment. However the surface and mid-depth salinity measurements from the C2 and CG mooring were used to interpolate salinity to the regions with no salinity data.

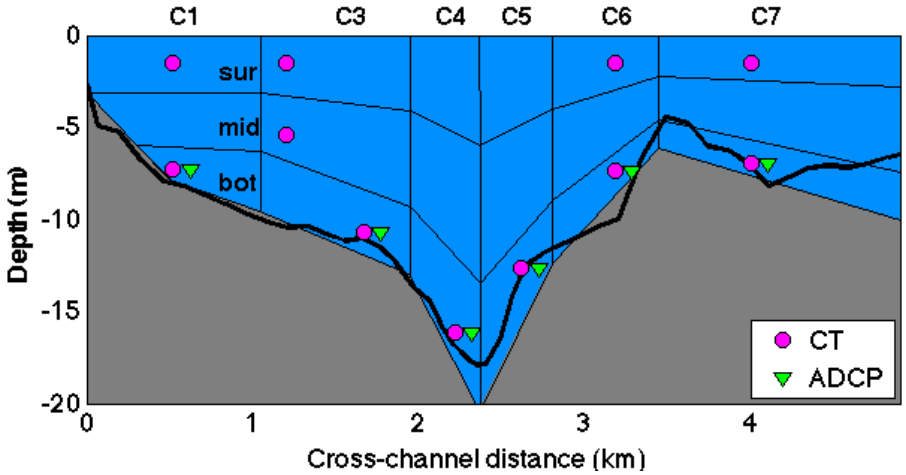

Figure 4.3: Regions in which the cross-sectional area was divided. The black thick line is the depth of the cross-sectional area from the ADCP measurements, from one of the transects, obtained during the tidal surveys.

Principal component analysis was performed on the depth-averaged velocity for each mooring, and according to this, the vertical profile of velocity was rotated to find the along and cross-channel components.

Next, the rotated velocity profiles were extrapolated to the surface, using a parabolic profile and imposing zero vertical shear close to the surface. The velocity profiles were also extrapolated to the bottom, using a logarithmic profile with a bottom roughness of $z_0 = 0.04\ m$ above the bed. These extrapolated velocity profiles were then stretched or compressed, according to the depth, at the edges of the boxes where the ADCPs were located. This is done in order to have a better estimate of the velocity magnitude at each box. Finally, the time series of the velocity in each box was calculated by

averaging, vertically and laterally, the velocity values that are contained in the box.

Salinity was interpolated in a way that, we considered, would reflect the spatial salinity structure of the site, according to our previous knowledge of this system. The mid-depth salinity for the C6 and C7 moorings were obtained using linear interpolation between surface and bottom salinity for each mooring. The surface salinity for the moorings C3, C4 and C5 were also linearly interpolated using the data from the surface CT sensors from moorings C1, C2, CG and C7. Likewise, the mid-depth salinity for the moorings C3, C4 and C5 were linearly interpolated using the bottom salinity from C2, the mid-depth salinity from CG and the interpolated mid-depth salinity for the C7 mooring. Finally the mid-depth salinity for the C1 mooring was interpolated using a 2D spatial interpolation (Delaunay triangulation), using all the salinity data in the cross-section. The interpolation of salinity, in our judgment, is the step that requires more adjustment and can introduce inaccurate estimates of the salt field, especially when it is decomposed in subtidal and tidal contributions.

The instantaneous total salt flux was calculated as:

$$FF_s(t) = \sum_{i=1}^{18} v_i(t) s_i(t) A_i(t), \tag{4.1}$$

where s_i, v_i and A_i are the salinity, along-channel velocity and area of each region. The net salt flux was obtained as: $F_s(t) =< FF_s(t) >$, where the brackets $<\ \ >$ represent a low pass filter to remove oscillations at tidal time scales. We used a Lanczos low pass filter with a cut-off period of 32 hours and a 70 hour half window.

In order to separate the contribution from different processes to the salt fluxes, the velocity and salinity field were decomposed as follows (Lerczak *et al.* 2006):

$$v_i(t) = v_0(t) + v_{e,i}(t) + v_{t,i}(t), \tag{4.2}$$

$$v_0(t) = \frac{Q_0}{A_0} = \frac{\langle \sum_{i=1}^{18} v_i\ A_i \rangle}{\langle \sum_{i=1}^{18} A_i \rangle}, \tag{4.3}$$

$$v_{e,i}(t) = \frac{\langle v_i\ A_i \rangle}{<A_i>} - v_0(t), \tag{4.4}$$

$$v_{t,i}(t) = v_i(t) - v_{e,i}(t) - v_0(t). \tag{4.5}$$

where Q_0 is the low-passed volume flux at the location of the mooring array and A_0 is the low-passed total cross-sectional area. There is a corresponding set of equations

for salinity. Under this decomposition, v_0 is an area-averaged, tidal-averaged velocity and is associated with the river discharge, but includes other contributions such as meteorological forced flows. v_e is a space-dependent, tidal-averaged flow and corresponds to exchange flow, and v_t is a space-dependent and tidal-dependent contribution and represents the tidal component of velocity.

Then the net total salt flux can be calculated in this way:

$$\begin{aligned}
F_s(t) &= \left\langle \sum_{i=1}^{18} v_i(t) s_i(t) A_i(t) \right\rangle \\
&= \left\langle \sum_i (v_0 + v_{e,i} + v_{t,i})(s_0 + s_{e,i} + s_{t,i}) A_i \right\rangle \\
&= v_0 \sum_i \langle A_i \rangle \, s_0 + \sum_i (v_{e,i} s_{e,i}) \langle A_i \rangle + \sum_i \langle (v_{t,i} s_{t,i}) A_i \rangle + \text{cross terms} \\
&= \quad Q_0 s_0 \quad + \quad \sum_i F_{e,i} \quad + \quad \sum_i F_{t,i} \\
F_s(t) &= \quad F_0 \quad + \quad F_e \quad + \quad F_t. \qquad (4.6)
\end{aligned}$$

Under this decomposition, F_0 is the advective salt flux and represents the flux due to river discharge or meteorological induced flows. F_e is called the steady shear dispersion and is the salt flux driven by the estuarine exchange flow. F_t is known as tidal oscillatory salt flux and is driven by the tidal flows. In Eq. 4.6, $F_{e,i}$ and $F_{t,i}$ are the contributions of each region to the salt flux due to the exchange flow and tidal flows respectively. The cross terms have been dropped because they are largely uncorrelated by definition (MacCready 2011).

The data from the tidal surveys were used to calculate the total instantaneous salt fluxes. The velocity and salinity data were interpolated into a rectangular grid with a vertical resolution of 0.25 meters. The horizontal resolution was about 120 meters, for velocity, and 60 meters, for salinity. In a similar way as we did with the mooring data, all the velocity profiles were rotated into along and cross-channel components, by performing principal component analysis to the depth average velocity. Then, these velocity profiles were extrapolated to the surface and to the bottom in the same way as the mooring data. Salinity was also extrapolated to the surface and bottom using a parabolic fit and imposing the vertical stratification to be zero at both boundaries. Finally, the velocity and salinity fields were interpolated to a common grid and the

total instantaneous salt flux was calculated according with Eq. 4.1, with the i index running from 1 to 4140 grid elements.

4.4 Results

During the time of the deployment, the river discharge at Trenton varied between 120 and 900 m^3/s (Fig. 4.4). There were two periods of approximately constant river discharge: between 07/17 and 07/27 and 07/30 and 08/06, and three sudden increases in river outflow: 07/05, 07/27 and 08/09, where the discharge increases about 3 fold. The mean sea level at Lewes (DE.) shows two complete spring-neap cycles: the first one, from 07/03 to 07/17, with a slight variation in tidal range, while the second one, from 07/17 to 07/31, presents a more pronounced fortnightly modulation. It also shows a consistent diurnal inequality in the magnitude of the sea surface height, which is commonly observed at mid-latitudes, particularly around the equinoxes.

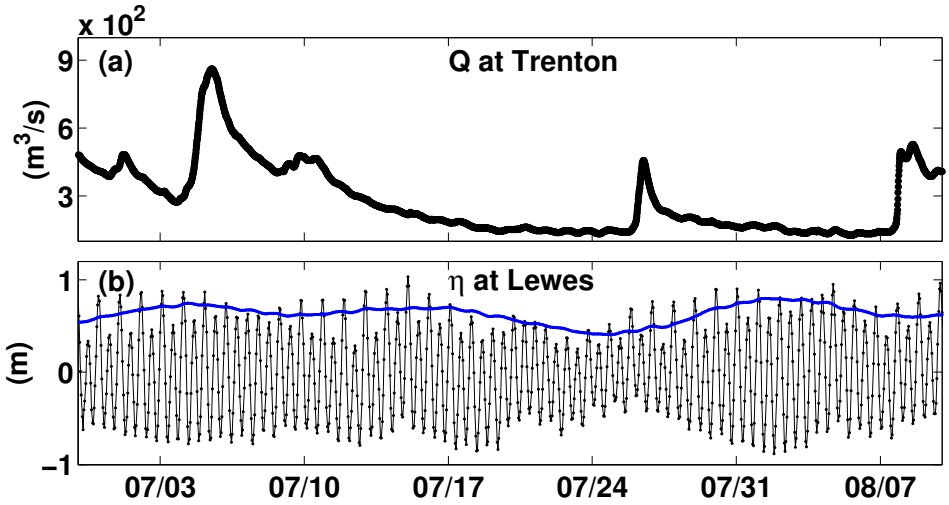

Figure 4.4: (a) River discharge at Trenton. (b) Mean sea level at Lewes (DE). The blue line shows the amplitude of the M2 component of the signal.

4.4.1 Decomposition of velocity and salinity fields

The area-averaged, subtidal, along-channel velocity v_0 ranges approximately between -0.05 to 0.05 m/s (Fig. 4.5). We would expect v_0 to be mostly negative, corresponding

to the oceanward velocity of the river outflow. Although the mean value of v_0 is negative, v_0 fluctuates around zero with a couple of strong positive peaks. The reason for these distinct positive values, is changes in the sea surface height due to passing storms. We will later discuss the consequences of these changes in sea surface height for the net salt fluxes. The area-averaged instantaneous salinity presents a clear tidal variability and the tidal-averaged salinity is a smooth function of time with values raging between 10 and 14.

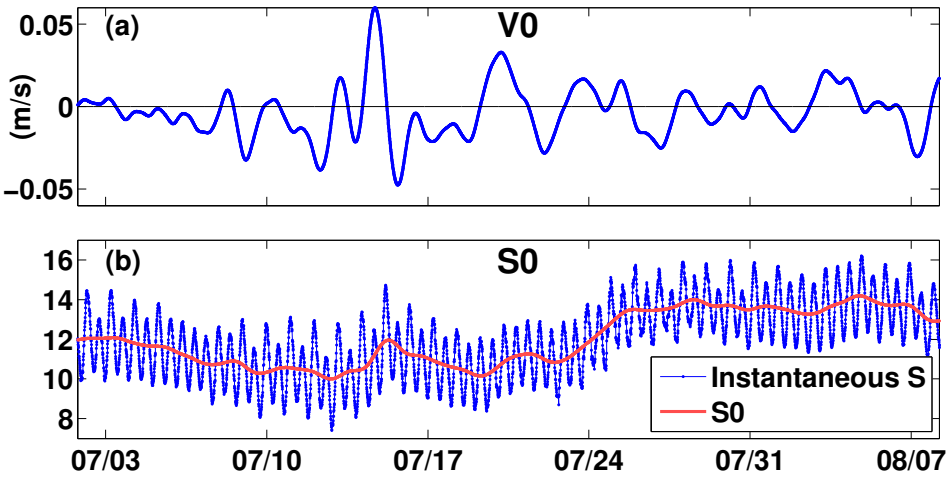

Figure 4.5: (a) Area-averaged, subtidal, along-channel velocity v_0. (b) Area-averaged, instantaneous salinity (blue line) and Area-averaged, tidal average salinity s_0 (red line).

The time series of the exchange flow (Fig. 4.6), for surface and bottom C4 regions close to the main channel, shows values that are relatively constant and there is little, if any, spring-neap variability in the exchange flow, which is inconsistent with the Hansen and Rattray solution. On the other hand, the subtidal salinity presents a significant enhancement during the neap tide period of 07/25 and decreases considerably on the next spring tide, but remains rather constant during the rest of the deployment. This period of significant change in the magnitude of s_e, coincides with a period of marked spring-neap variability in the tidal range (Fig. 4.4).

The spatial structure of v_e, shows a flow with a clear surface layer directed oceanward. This exchange flow is strongly directed landward in the left portion of the main channel (mid and bottom C3 and C4) for both spring and neap tide. However the right

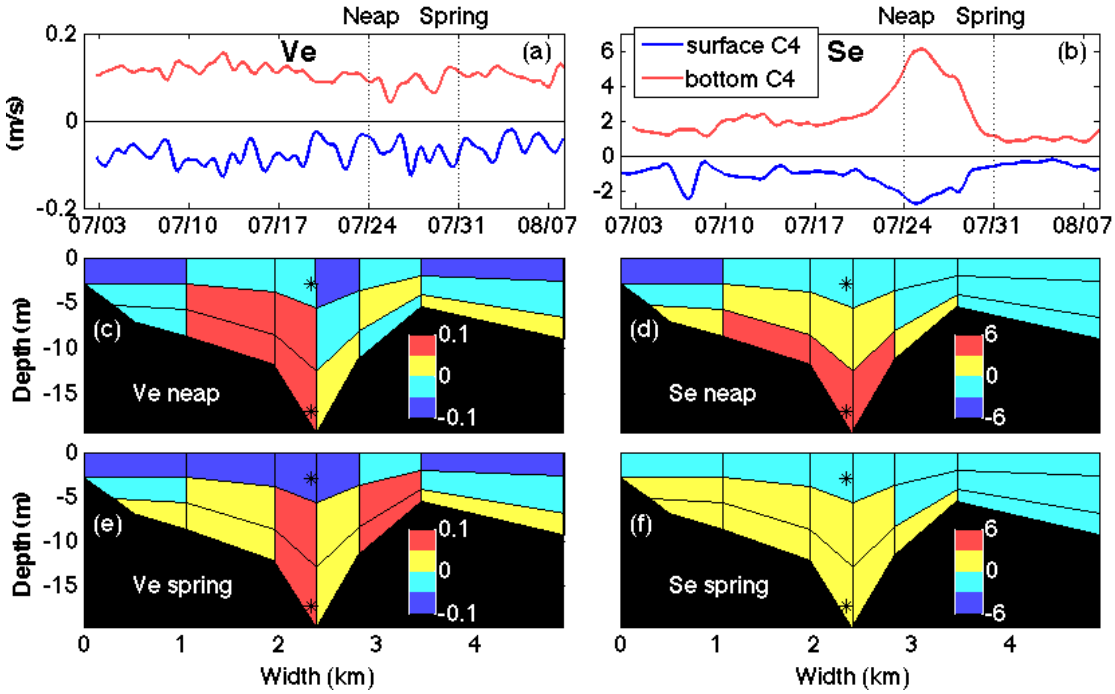

Figure 4.6: Time series of the (a) exchange flow and (b) subtidal salinity, corresponding to the surface-C4 region, in red, and to the bottom-C4 region, in blue. (c) and (d) Spatial structure of the exchange flow, and (d) and (f) the subtidal salinity, for periods of neap and spring tide. The color scale for the exchange flow is in m/s. Positive and negative values indicate landward and oceanward direction, respectively. The stars indicate the two regions pictured in (a) and (b). In this cross-sectional areas, NJ. is on the right side and DE. is on the left side.

portion (mid and bottom C5 and C6) presents weaker positive and negative values during neap, but it is clearly positive during spring tide. v_e tends to be weak in the mid and bottom regions of both flanks, but it is predominantly oceanward in the left flank during neap tide. The spatial structure of the subtidal salinity resembles the spatial structure of v_e. s_e is negative in the surface layer and right flank, but positive values persist in the bottom and middle layer in the main channel and at depth in the left flank.

The tidal velocity field (Fig. 4.7) fluctuates approximately between ± 1.5 and ± 0.8 m/s at the surface and bottom C4 region, respectively. The tidal salinity field shows that the maximum change in salinity at tidal time scales, in this location, roughly ranges between 4 and 2. Both, tidal velocity and salinity fields are accompanied by a large diurnal inequality.

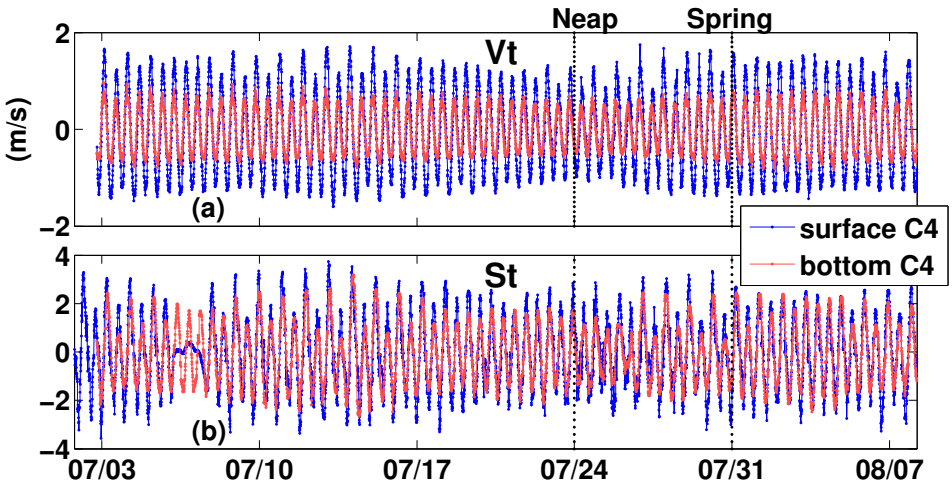

Figure 4.7: (a) Tidal velocity and (b) tidal salinity field for the surface and bottom C4 regions.

4.4.2 Salt fluxes: spatial and temporal variability

The area integrated instantaneous salt fluxes from the tidal surveys on July 28 and August 24, were compared with the estimates from the mooring array, with very good agreement (Fig. 4.8 (a) and (b)). The spatial structure for the instantaneous salt fluxes was also compared for two different transects (Fig. 4.8 (c), (d), (e) and (f)). The transects from the tidal surveys reveal that most of the salt fluxes occur in the middle of the channel and are weak in the flanks. The spatial structure from the mooring array also shows strong salt fluxes at the surface and middle region in the main channel (surface and middle C3, C4 and C5 regions), but shows a more vigorous flux at the surface and middle regions of the flanks. This is probably due to the difference in the spatial resolutions of both grids. A more direct comparison would require the interpolation of the salt flux from the tidal surveys, into the grid defined for the mooring array.

The contribution to the steady shear dispersion, for the surface and bottom C4 regions (Fig. 4.9 (a)), show a F_e that is always positive, with particular enhanced values at depth. It presents stronger values during neap and weaker values during spring tide, but only for the second half of the record, where the sea surface level exhibits a more pronounced fortnightly cycle. On the other hand, the contributions to tidal oscillatory

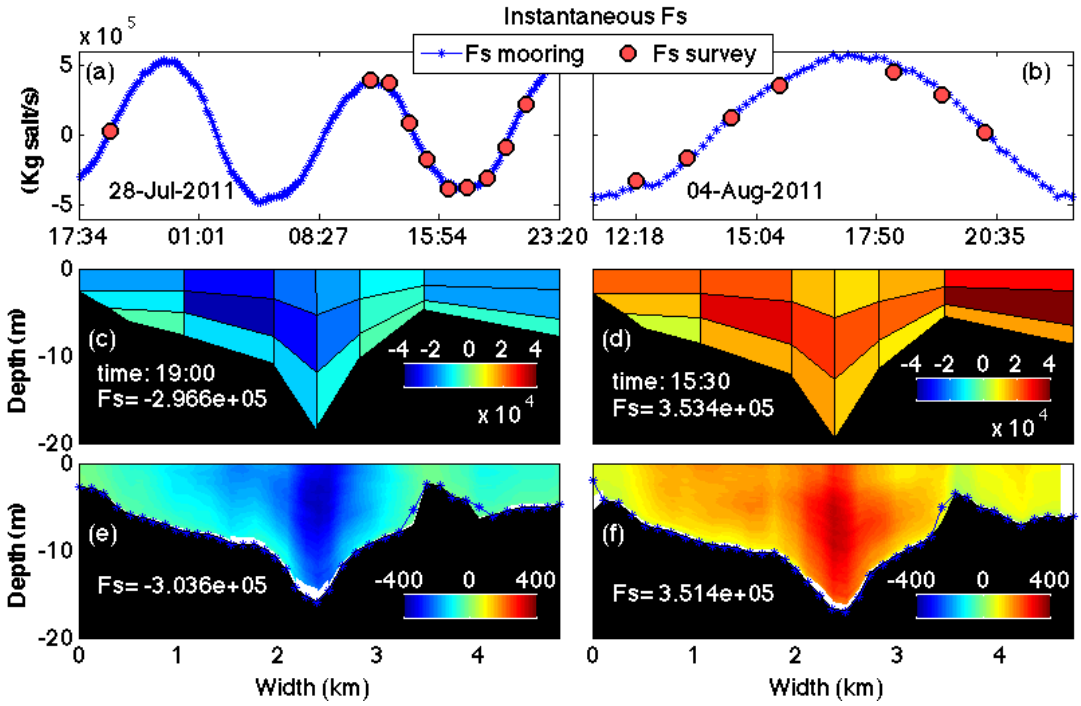

Figure 4.8: (a) and (b) Comparison between the time series of the instantaneous salt fluxes from the mooring array (blue line) and the different transects from the tidal surveys (red dots) on July 28 and August 4, respectively. The time assigned to the transects of the tidal surveys, was defined as the average time that took to cover the cross-sectional area. (c) and (d) Contribution to the instantaneous salt flux from each region in the mooring array on July 28 at 19:00 hours and August 4 at 15:30 hours, respectively. (e) and (f) Spatial structure of the instantaneous salt fluxes from the tidal surveys on the same dates as (c) and (d).The color scale is in $kg\ salt/s$. Positive values indicate landward salt flux. In this cross-sectional areas, NJ. is on the right side and DE. is on the left side.

salt flux (Fig. 4.9 (b)) are such that the bottom region presents weak negative values, and the surface region, stronger positive values, with no clear spring-neap variability. The spatial structure of F_e (Fig.4.9 (c) and (e)) indicate that most of the positive salt fluxes are concentrated on the left portion of the cross-section, with particular strong values in the bottom C4 region and the surface left flank. The middle and bottom right portion (middle C5 and C6, bottom C6 and C7) and the left middle and bottom left flank, predominantly promote weak salt fluxes that oscillate between positive and negative values.

On the other hand, the spatial structure of F_t (Fig. 4.9 (d) and (f)) shows that, most of the right portion consistently produces substantial negative fluxes, while the

positive fluxes are concentrated on the left side of the main channel (surface C1, C3, C4 and middle and bottom C3). These spatial patterns, for both F_e and F_t, change slightly from neap to spring tide but the main features remain the same.

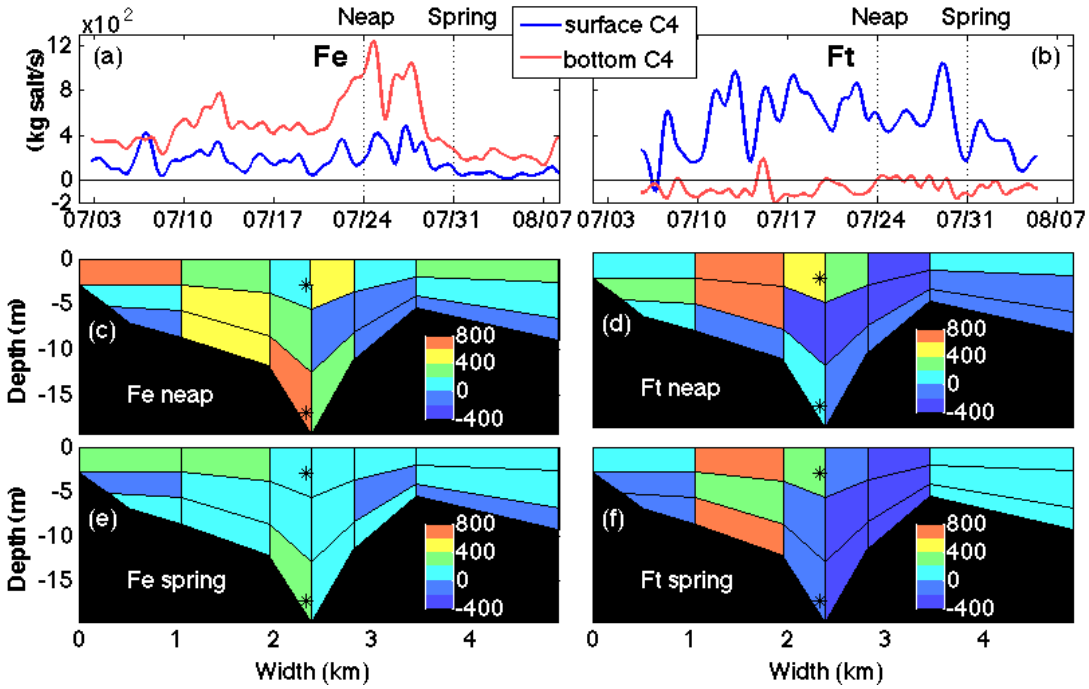

Figure 4.9: (a) Time series for steady shear dispersion F_e and (b) tidal oscillatory salt flux F_t, for the surface and bottom C4 regions. (c) and (d) Contribution of each region to F_e during times of neap and spring tide respectively. (d) and (f) Contribution of each region to F_t during times of neap and spring tide respectively. The color scale is in $Kg\ salt/s$. Positive values indicate landward salt flux. In this cross-sectional areas, NJ. is on the right side and DE. is on the left side.

The accumulative contribution from these regions produce the area-integrated, tidal-average salt fluxes that are depicted in Fig. 4.10 (a). The most striking feature is how F_0 dominates the salt fluxes, and as a consequence F_e and F_t are close to be an order of magnitude smaller than F_0. Additionally F_0 exhibits very strong positive values, that mimic the positive peaks on v_0, and implies that salt fluxes, in the 2-5 day band, are driven by the variability in v_0. The total salt flux F_s closely follows F_0 because is the dominant mechanism.

The time series of F_e (Fig. 4.10 (b)), shows that is always positive and presents a clear enhancement during neap and a reduction during spring tide, especially during

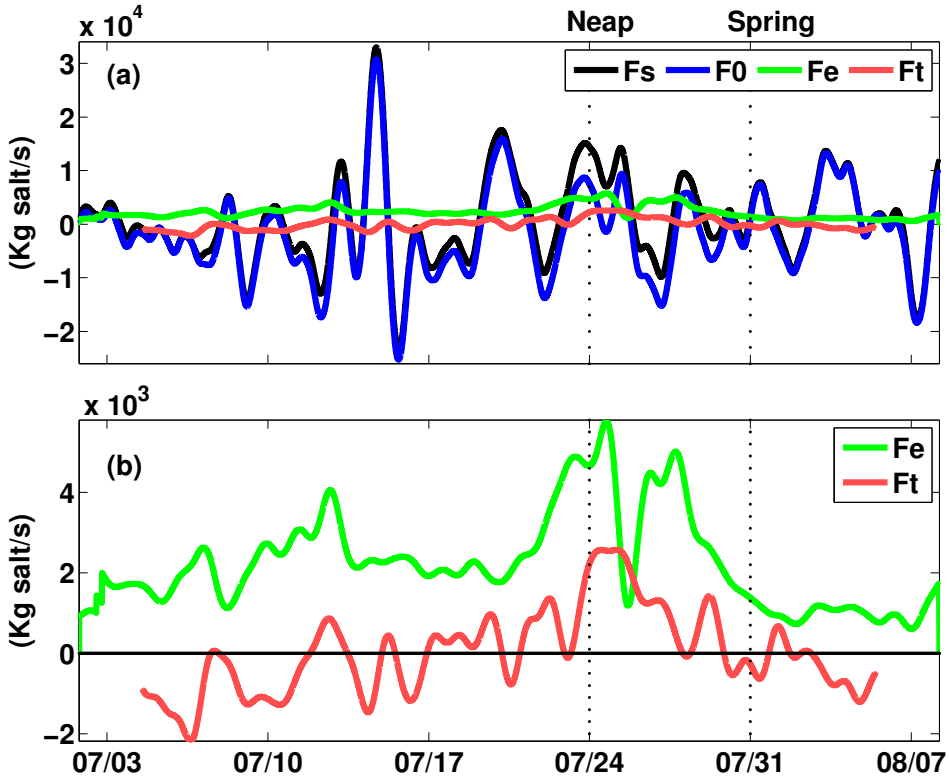

Figure 4.10: (a) Time series of the area-integrated, tidal-average salt fluxes. F_s, F_0, F_e and F_t represents the total salt flux, the advective salt flux, the steady shear dispersion and the tidal oscillatory salt flux. (b) Time series of F_e and F_t alone.

the second half of the record. This time variability is expected since the values of s_e are intensified during neap, in particular at depth in the main channel. However, F_t exhibits mostly negative values during the first half of the deployment, but becomes positive during the neap tide period, where a significant decrease in currents (07/25) occured. Subsequently F_t decreases and becomes negative again on the next spring tide. For about half of the time, F_t remains negative and this implies that the area-integrated tidal oscillatory salt flux can be either a landward salt flux, as it is usually assumed, or an oceanward salt flux.

4.5 Discussion

4.5.1 F0 driven by meteorological forcing

The area-integrated, tidal-average salt fluxes are dominated by F_0, which is an order of magnitude larger than the other two mechanisms: F_e and F_t. In addition F_0 presents several sharp positive peaks associated with strong landward salt fluxes. The cause of this marked positive values is investigated by comparing it to the area-average, tidal-average velocity $v_0 = Q_0/A_0$. Q_0 is weakly correlated with river flow (r $\sim$ 0.15). However the tidal-average signal of the mean sea surface level at the entrance of the bay (Lewes, NJ.), has a better correlation with Q_0 (r $\sim$ 0.37), in particular during sudden changes in sea level due to passing storms. Q_0 is then, primarily, driven by changes in sea surface height rather than river discharge. It appears, that in this system, meteorological forcing plays a very important role on driving salt inside the bay at subtidal time scales, particularly in the 2-5 day band.

Nevertheless, the mean value of the subtidal volume flux from the mooring: $Q_0 = 144\ m^3/s$, should be close to the mean value of the total river input into the bay, which we estimate as 2 folds the river discharge at Trenton (NJ.): $Q_{river} = 660\ m^3/s$. The disagreement between these two values suggest that: first, the estimate of the total fresh water input into the bay needs to be refined, and second, the parabolic profile used to extrapolate velocity to the surface, with zero shear at the surface, is possibly giving us an underestimation of the mass transport in the upper two meters of the water column. We note that an underestimate of the velocity in the upper meters of the water column by 0.05 m/s corresponds to 350 m^3/s.

4.5.2 Subtidal variability in the salt fluxes

If the only mechanism responsible for the advective salt fluxes were the river outflow, this mechanism would only contribute with a oceanward flux. We can recalculate the salt fluxes, assuming that Q_0 is equal to the total fresh water input into the bay (Fig. 4.12). The results for F_e and F_t are almost unchanged since $v_0 = Q_0/A_0$ only represents about 10% and 1% of the subtidal (v_e) and tidal velocity (v_t). Under this hypothetical

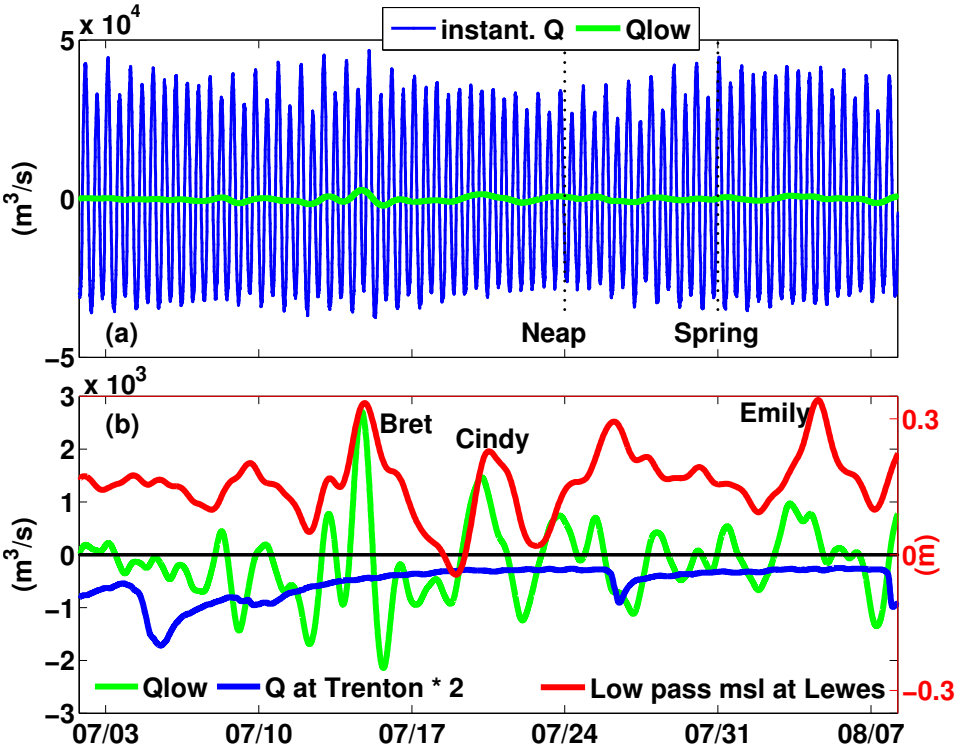

Figure 4.11: (a) Time series of the Instantaneous volume flux Q and its tidal-average signal Q_0. (b) Tidal-average volume salt flux (green line) compared with the river discharge at Trenton (NJ.) multiply by 2 (blue line), which approximately represents the total fresh water input into the bay. The tidal-average of the mean sea level at Lewes (De.) (red line) is also shown. The names, next to some of the peaks in the sea surface level line, correspond to passing storms.

situation, the total salt flux is negative the first two weeks of the deployment due to a peak in river discharge on 07/06. In the subsequent three weeks, the river discharge remains relatively constant (grey area in Fig. 4.12), except on 07/27, when the discharge increases about three times, but it quickly returns to its previous value. During this period the total salt flux is such that is positive around neap tide and becomes negative around spring tide. This is consistent with numerical simulations in Delaware Bay (Aristizábal and Chant 2013, Chapter 2 of this manuscript), that showed that under constant river forcing, the net total salt flux was oceanward during spring tides and landward during neap tides. In an observational study in the Hudson River, Lerczak *et al.* (2006) found the same subtidal variability in the total salt flux, after removing oscillations at a time scale of 3 to 5 days.

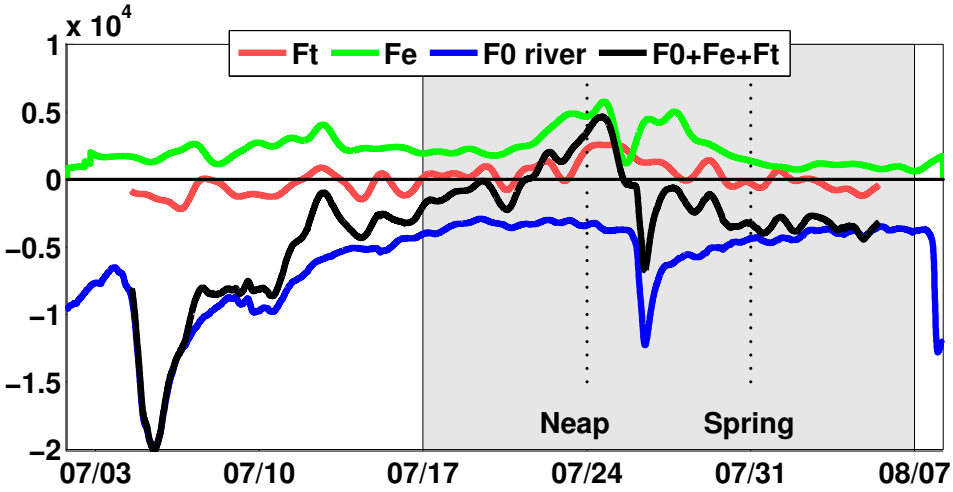

Figure 4.12: Time series of the area-integrated, tidal-average salt fluxes under the assumption that Q_0 is only equal to the total fresh water input into the bay. F_e and F_t stands for the steady shear dispersion and the tidal oscillatory salt flux. F_0 river is the advective salt flux equal to $Q_0 S_0$. The black line is the total salt flux under this hypothetical situation.

The aforementioned studies also showed a spring-neap variability in F_e that is consistent with our results: F_e is clearly enhanced during neap tide and is diminished during spring tide (Fig. 4.10 (b)). This variability is explained by a two-layer, vertically-sheared exchange flow that transports relatively fresh water at the surface oceanward, and saltier water at depth landward, both resulting in a landward salt flux. This salt flux mechanism is maximum when the salinity difference between the bottom and surface layer increases during neap tide, and is inhibited when stratification is minimum during spring tide.

Subtidal variability of F_t

The subtidal variability in F_t is less clear, but we do see a consistent oceanward enhancement during the neap tide period centered on 07/25 (Fig. 4.10 (b)). This variability is consistent with numerical simulations in Delaware Bay (Aristizábal and Chant, in press), that showed a very clear intensification of F_t during neap tides, in the same location of the mooring array. In the results by Lerczak *et al.* (2006), F_t is very variable. However there are two neap tide periods, characterized by strong stratification,

in which F_t becomes negative. Based on this, they suggest that F_t may experience a subtidal variability, such that, F_t is smallest during neap and largest during spring tide, an opposite variability to the one we found in Delaware. Previous parameterizations, for the along-channel dispersion coefficient K_t (Banas *et al.* 2004; MacCready 2007), favor the subtidal variability suggested by Lerczak *et al.* (2006).

In order to understand the time variability in the area-integrated F_t, it is important to recognize that F_t has a high spatial variability. The magnitude of Ft for the various regions is relatively high but of opposite signs. This means that some regions contribute to a landward salt flux, while others contribute with a seaward salt flux. When all these contributions are added up, we obtain an area-integrated signal that not necessarily reflect the time variability of the individual regions.

The direction of the tidal salt flux is determined by the phase difference between the along-channel velocity and salinity. When the along-channel velocity and salinity are in quadrature, i.e. their phase difference is a quarter of a period ($\sim$ 3.1 hours), the tidal oscillatory salt flux is equal to zero. This situation corresponds to maximum salinity at the end of flood and minimum salinity at the end of ebb. This occurs when salinity is driven exclusively by the along-channel advection by the tidal flows. However, as other processes become important, such as mixing and cross-channel advection, the along-channel velocity and salinity become out of quadrature. Estimate of the phase difference between the M2 component of the tidal along-channel velocity, v_t, and the tidal salinity, s_t (Fig. 4.13 (a)), show that the phase difference spans from 2 to 4 hours. The regions with phase difference less than quadrature (blue colors) contribute with a positive salt flux while the regions with a phase difference larger than quadrature (warm colors) contribute with a negative salt flux. The spatial structure of the tidal oscillatory salt flux (Fig. 4.9) closely resembles the spatial pattern for the phase difference between s_t and v_t. This suggests that other processes, besides along-channel advection of salinity, are at play at this location in Delaware Bay.

The time variability of the tidal oscillatory salt flux is dictated by the time variability of v_t and s_t combined. The spring-neap cycle produces stronger tidal currents during spring than neap. However the fortnightly variability of s_t is more complex. Fig. 4.14

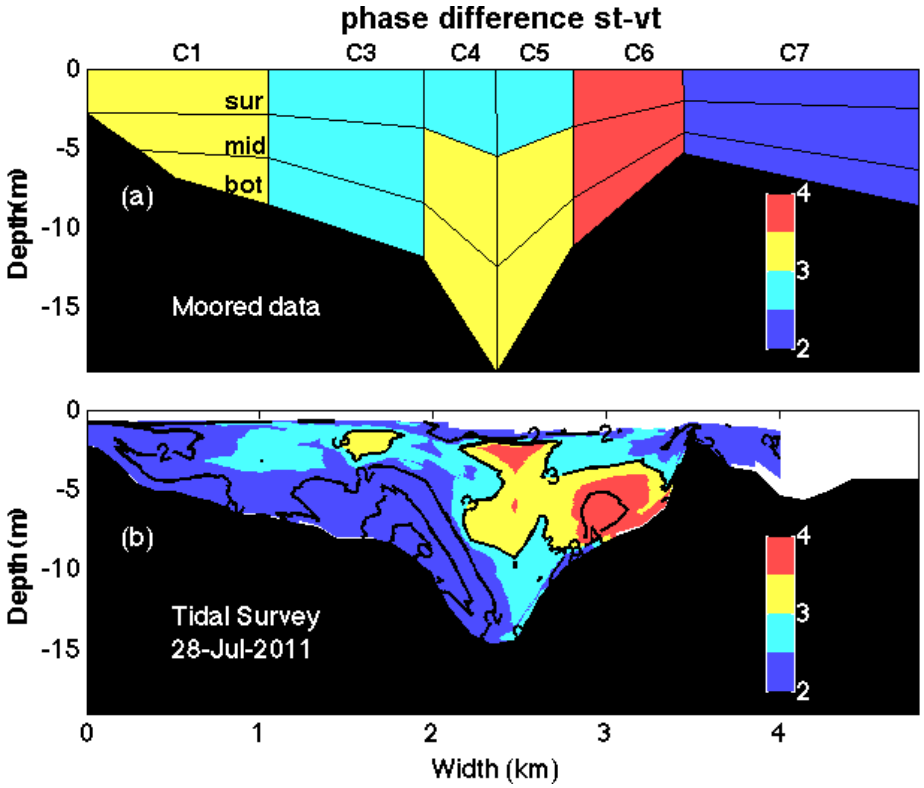

Figure 4.13: (a) Phase difference between the M2 component of the tidal salinity (s_t) and tidal velocity (v_t) from the moored data. (b) Phase difference between the along-channel velocity and salinity for the tidal survey on July 28. The color scale is in hours. In this cross-sectional areas, NJ. is on the right side and DE. is on the left side.

shows the time series of F_t and s_t for different regions in the cross-section. The first region, middle C3 shows a clear increase in F_t during neap tide when compared to spring tide. This variability is explained by an increase of s_t during neap tide as well. Contrary to this, the surface C2 region, which also contributes with a positive flux, presents a stronger values towards spring than during neap tide. In this case s_t shows a very subtle decrease during neap. Among the regions that bring salt oceanward, middle C5 is always weakly negative but switches to weak positive values around neap tide. Accordingly the time series of s_t shows a clear amplification on neap. The surface region C6, always has negative (i.e. oceanward) values because the phase difference between s_t and v_t is approximately 4 hours. The spring-neap variability of s_t has small values during neap compared to spring. This variability of s_t, combined with weaker tidal currents on neap and stronger tidal currents on spring, produces a weak oceanward

salt flux on neap and a stronger oceanward salt flux on spring. Therefore, the F_t of this regions has a very small contribution to the area-integrated F_t during neap, but diminishes the landward fluxes, or equivalently, enhances the oceanward fluxes during spring tide. This effectively reinforces the observed spring-neap variability in the area-integrated F_t. Our last case is the bottom C3 region, showing an F_t that switches to negative during neap tide and becomes positive towards spring. Similar to the surface C2 region, s_t also exhibits a subtle decrease during neap and a slight increase on spring, which combined with weak neap currents, produce the observed variability.

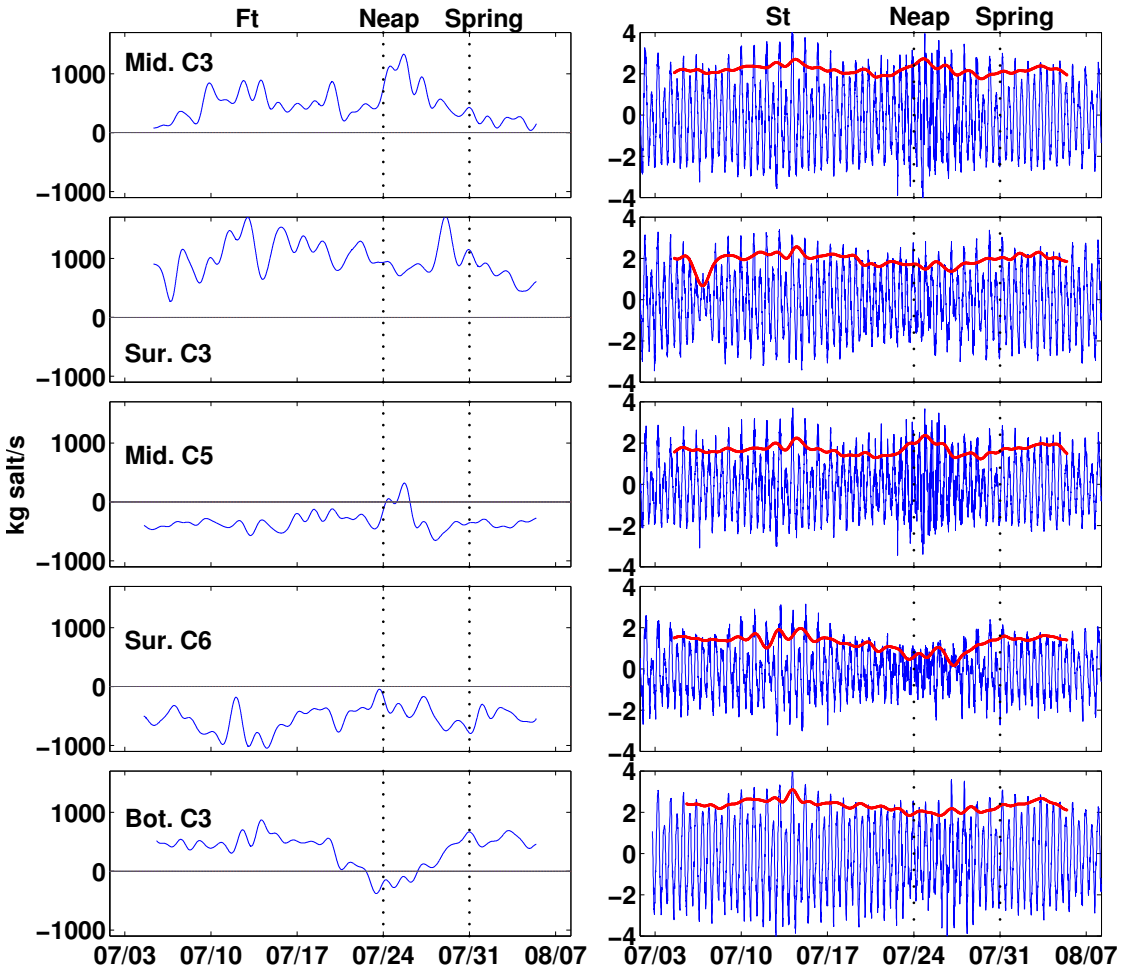

Figure 4.14: Time series of the tidal oscillatory salt flux (left column) and the tidal component of salinity s_t (right column) for different regions in the cross-section. The red line is the demodulated s_t.

Fig. 4.14 exemplifies how different time variabilities can manifest at different locations. The spring-neap variability in the area-integrated F_t is a the sum of these different variabilities. In our case, the enhancement of the area-integrated F_t during neap tide is due to a decrease, or reversal to positive, of the salt flux in the regions that contribute negatively, in addition to, a solid intensification of F_t during neap in the middle C3 region.

The tidal oscillatory salt flux is ultimately controlled by the mechanisms that bring along-channel velocity and salinity out of quadrature and that control their time variability. Aristizábal and Chant (2013) (Chapter 2 of this manuscript) suggested that this mechanism in Delaware Bay is mediated by the cross-channel flows. During the ebb tide, the circulation consists of a counterclockwise cell, looking into the bay with the Delaware side to the left. This circulation brings fresh water from the surface to the bottom left side of the channel, augmenting the freshening action of the along-channel flows, and therefore, causes this region to be the freshest before slack after ebb. This brings along-channel salinity and velocity out of quadrature, with a phase difference less than 3.1 hours, and causes a positive salt flux in this region. On the New Jersey side, the lateral flows are bringing salty water from the bottom towards the right flank, opposing the freshening action of the along-channel flows, bringing the along-channel velocity and salinity out of quadrature as well. Under this conditions, the phase difference is larger than 3.1 hours, and as a result, this region contributes with a seaward salt flux. During the flood, the circulation reverses, though it has a more complex pattern, and yet produces the same effect on the phase difference between along-channel velocity and salinity.

In the numerical simulations in Aristizábal and Chant (in press), s_t is significantly enhanced during neap tides compared to spring tides, in the regions with a phase difference less than quadrature. Again, this can be attributed to the advection of salt by the cross-channel flows. For example during ebb, as the lateral flows move fresh water from the surface to the bottom left side of the channel, the variability of s_t increases (Fig. 2.9). This deviation is enhanced when the bottom to surface salinity difference is at its maximum, which occurs during neap tides.

Our results for the phase difference between the along-channel tidal velocity and salinity are consistent with the mechanism described above. Furthermore, the time series of s_t also show different subtidal variability, depending on the location, which is also in agreement with this proposed mechanism.

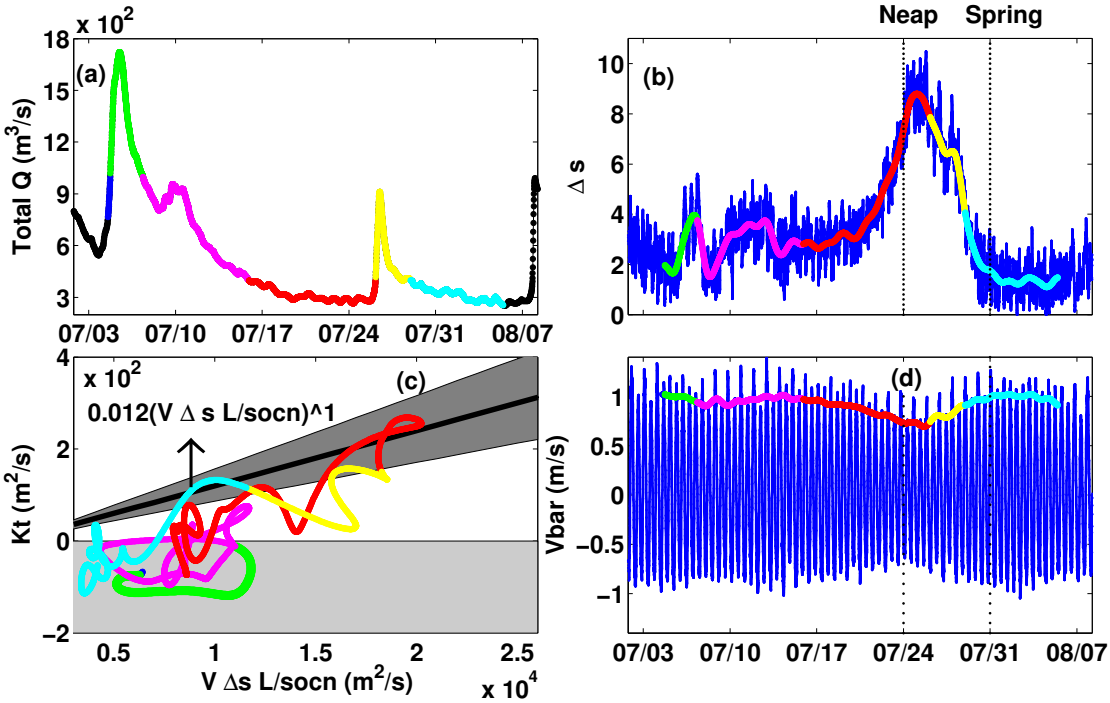

Figure 4.15: (a) Total river discharge into the system. The different colors represent different periods in the river discharge. (b) Time series of the bottom to surface salinity difference Δs (blue line) in the middle of the channel (region C4). The thick multi-color line is the low pass signal of Δs. (c) Comparison between the along-channel dispersion coefficient K_t from observations (multi-color line) and the proposed parameterization by Aristizábal and Chant (in press) (black line), expressed by the equation on the figure. (d) Time series of the depth average tidal velocity (blue line) and the amplitude of the M2 component (multi-color line).

Finally we compared our estimate for the along-channel dispersion coefficient, K_t, with a scaling presented in Aristizábal and Chant (in press) (Fig. 4.15 (c)),

$$K_t = 0.012(V\Delta sL/s_{ocn})^1, \tag{4.7}$$

where V is the magnitude of the depth average along-channel velocity (Fig. 4.15 (d)), Δs is the low pass of the bottom to surface salinity difference (Fig. 4.15 (b)), L is the length of the salt intrusion length, for which we have used a value of 100 km, and s_{ocn} is

the oceanic salinity set to 32. The constant of proportionality, 0.012, and the exponent, 1, are a result of fitting the output of six runs, each with a different river input that was kept constant through the duration of the run.

Our results for K_t have many negative values, as a result of a F_t that contributes with oceanward salt fluxes for about half of the deployment (Fig. 4.10). It is interesting to note that when river input increases sharply (green and yellow lines in Fig. 4.15 (a)), K_t falls off the parameterization. But, as the system approaches steady state when the river discharge relatively constant (red and blue lines in Fig. 4.15 (a)), the values of K_t are within the error bars. The fact that this parameterization was developed based on numerical simulations forced with constant river discharge, suggests that it is in those conditions where the comparison between the parameterization and experimental results is more relevant

In summary, these results show that the salt fluxes at tidal time scale not only can respond to changes in the magnitude of the tidal velocities, but also to the changes in stratification. The later tends to dominate because the variability of s_t far exceeds that of v_t. Finally, the parameterization for K_t developed with the numerical model results is consistent with the field estimates during times of steady river discharge.

4.6 Conclusions

The area-integrated, tidal-averaged advective component of the salt fluxes fluctuates between negative and strong positive values. This component dominates over the steady shear dispersion and tidal oscillatory salt flux. The reason for this, is that the advective salt flux is driven by changes in sea surface height due to passing storms at the 3-5 day time scale, and this variability overwhelms the seaward flux associated with river discharge.

The steady shear dispersion is always positive and presents a spring-neap variability, that is consistent with a two layer exchange flow, that brings more salt into the system for periods of high stratification.

The tidal oscillatory salt flux, F_t, oscillates between positive and negative values

during the first half of the deployment, but shows a clear increase around a strong neap tide, and eventually decreases becoming negative during the next spring tide. This subtidal variability is contrary to previous parameterizations for the along-channel dispersion coefficient (Banas *et al.* 2004; MacCready 2007), which predict an enhancement of the tidal oscillatory salt flux during spring tides, due to increased tidal currents.

The subtidal variability of Ft, in the individual regions of the cross-section, depends on the combined spring-neap variability of the tidal component of salinity s_t and the tidal component of velocity v_t. For example, for a positive flux when s_t is strengthen during neap, F_t is strengthen during neap tide as well. Otherwise, when s_t shows no variability or a decrease during neap tide, then F_t displays a spring-neap variability that is consistent with the fortnightly modulation of v_t.

In addition, there are regions in the cross-section that contribute with fluxes of opposite direction. The direction of the flux is positive (negative) when the phase between the along-channel velocity and salinity is less (larger) than quadrature. The along-channel velocity and salinity are driven out of quadrature by the lateral advection of salt by the cross-channel flows (Aristizábal and Chant, in press).

Finally, we compared our estimate of the along-channel dispersion coefficient with a proposed parameterization by Aristizábal and Chant (in press). The observational estimate agrees with this parameterization during periods when the river discharge is relatively constant.

Chapter 5

Conclusions

Delaware Bay can be characterized as a partially mixed estuary, with bottom to surface salinity difference exceeding 10 psu in the middle reach of the bay, for periods of high river discharge and neap tides. While the bay is weakly stratified during spring tide, particularly during low to moderate flow conditions (Garvine *et al.* 1992; Beardsley and Boicourt 1981). Periods of relatively strong stratification during neap tide conditions have significant influence on the salt flux and thus this work emphasizes the importance of stratification in Delaware Bay.

Results from numerical simulations show that the exchange flow, in the lower and middle bay, is laterally sheared in the flanks and vertically sheared in the main channel. This is consistent with observations and theoretical estimates (Wong 1994) that attribute this spatial structure to the cross-channel variations in depth. In the upper bay, where the channel significantly narrows, the subtidal circulation conforms to the classic two vertical layers exchange flow.

The subtidal salinity structure has similar characteristics as the exchange flow. In the wide part of the bay, the salinity field is laterally sheared with two fresher branches in the shallow flanks, in particular in the Delaware side where the river outflow behaves as a coastal current, and a salty bottom layer in the main channel. In the upper bay, the subtidal salt field is vertically segregated with fresher values at the surface and salty values at depth.

The area-integrated salt fluxes show that the steady shear dispersion (F_e) and tidal oscillatory salt flux (F_t) are of the same order of magnitude. Both fluxes are intensified during neap tide and diminished during spring tide, especially in the upper bay, and as a result, the system gains salt during neap and looses salt during spring tide.

This spring-neap variability of the tidal oscillatory salt flux is contrary to previous parameterizations (Banas *et al.* 2004; MacCready 2007), where an increased is expected during spring tide due to stronger tidal flows. The intensification of F_t during neap tides is caused by an enhancement of the intra-tidal variability in salinity (s_t) that is induced by the action of the cross-channel flows on the salinity field, and provides a mechanism that brings the along-channel velocity and salinity out of quadrature. Based on this mechanism, a scaling for the along-channel dispersion coefficient (K_t) is proposed, such that is proportional to both, the magnitude of the along channel velocity and the bottom to surface salinity difference.

The results for the area-integrated salt fluxes from observations present a slight more complex picture, although they are still consistent with the results from the numerical simulations. The advective salt flux dominates the salt fluxes and presents both strong positive (landward) and negative (seaward) values, that are correlated with changes in sea surface height due to passing storms. This contrasts with the results from the 3D model, which does not include meteorological forcing, where the advective salt flux is always negative corresponding to a flux driven solely by river discharge.

The steady shear dispersion is always a landward salt flux and has a subtidal variability that agrees with the numerical model. On the other hand, the tidal oscillatory salt flux fluctuates between positive and negative values, but it shows a clear increase in the landward flux during a neap tide period. The contribution to F_t from each individual region in the cross-sectional area, reveals that in the regions where F_t is enhanced around neap tide, the tidal component of salinity (s_t) is augmented on the same period. This is consistent with the mechanism proposed to explain the intensification of Ft during neap tides.

A comparison between the observational estimate for the along-channel dispersion coefficient and the proposed parameterization from the model results, shows that they only agree during periods where the river discharge has reached a relatively constant value. In fact, it is only during these periods that is meaningful to compare both estimates, given that the parameterization from the numerical simulations is obtained under constant river input.

Observations (Garvine *et al.* 1992) and the numerical simulations show that the salt field in Delaware Bay responds weakly to river discharge, when compared to the $Q^{-1/3}$ scaling predicted by the classic theory for exchange dominated systems. It is suggested, from the analysis of the numerical output, that this insensitivity is caused, in part, by the dependence of F_e and F_t with river discharge (Q) and the relative importance of F_t to total upstream salt flux (ν). For low river discharge ($\propto$ 350 m^3/s), F_e and F_t contribute almost equal to the landward salt fluxes, but as Q increases, Fe becomes the dominant mechanism. Meanwhile, the vertical eddy viscosity is also reduced with river discharge, due to an increase in stratification as suggested by Monismith *et al.* (2002), hindering vertical mixing and allowing the salt to travel further upstream via the exchange flow, ultimately stiffening the salt field. Bathymetry can also have a significant effect on the respond of the salt field with river discharge, as demonstrated in San Francisco Bay by Ralston *et al.* (2008). In Delaware Bay, bathymetry alone could not explain the insensitivity of L on Q but instead, the reduction of the vertical mixing with river discharge is playing a more evident role.

The cross-channel tidal surveys and mooring data affirm that bottom to surface salinity difference is larger towards the end of the flood and decreases towards the end of the ebb tide, during periods of high stratification. This tidal variability in stratification is opposite to the variability expected from the tidal straining mechanism in estuaries proposed by Simpson *et al.* (1990). It is concluded that there is competition between the straining caused by the cross-channel flows, which tend to stratify the water column during flood and de-stratify it during ebb, and the straining caused by the along-channel flows, that have the opposite effect.

The analysis of the cross-channel momentum balance reveals that the lateral flows are driven by the interplay between Coriolis and the cross-channel baroclinic pressure gradient. The Coriolis term is driven by the shear in the along-channel velocity, and causes the surface and bottom to flow on opposite directions, switching signs approximately around slack water.

On the other hand, the cross-channel baroclinic pressure gradient switch signs halfway through each tidal cycle. This is caused by a fluctuation in the cross-channel

density gradient, induced by the straining of the salinity field by the cross-channel flows during ebb and the subsequent readjustment during the flood tide. This indicates that the cross-channel baroclinic pressure gradient is itself modified by the lateral flows.

The results from this work demonstrate how the cross-channel flows modify the salt field, and in turn, this has important consequences for the stratification at tidal time scales and net salt transport by the tidal flows.

Bibliography

Abood, K. A. (1974). Circulation in the hudson estuary. *Annals of the New York Academy of Science*, **250**, 38111.

Adkins, J. (2012). State of the delaware estuary 2012. *Estuary News*, **22**(4).

Aristizábal, M. and Chant, R. (in press, 2013). A numerical study of salt fluxes in delaware bay estuary. *J. Phys. Oceanogr.*

Banas, N. S., Hickey, B. M., and MacCready, P. (2004). Dynamics of willapa bay, washington: a highly unsteady, partially mixed estuary. *J. Phys. Oceanogr.*, **34**, 2413–2427.

Beardsley, R. C. and Boicourt, W. C. (1981). *On estuarine and continental shelf circulation in the Middle Atlantic Bight*. MIT Press, Cambridge, Mass.

Bowen, M. M. (2000). *Mechanisms and variability of salt transport in partially stratified estuaries.* Ph.D. thesis, Woods Hole/Massachusetts Institute of Technology Joint Program in Physical Oceanography.

Burchard, H. and Hofmeister, R. (2008). A dynamic equation for the potential energy anomaly for analyzing mixing and stratification in estuaries and coastal seas. *Estuar. Coast. Shelf Sci.*, **77**, 679–687.

Chant, R. J. (2002). Secondary circulation in a region of flow curvature: Relationship with tidal forcing and river discharge. *J. Geophys. Res.-Oceans*, **107**(C9).

Chant, R. J. (2010). *Estuarine Secondary Circulation. In: Valle-Levison, A. (Ed.), Comtemporary Issues in Estuarine Physics*. Cambridge University Press.

Chant, R. J. and Stoner, A. W. (2001). Particle trapping in a stratified flood-dominated estuary. *J. Marine Res.*, **59**, 29–51.

Chant, R. J., Geyer, W. R., Houghton, R., Hunter, E., and Lerczak, J. (2007). Estuarine boundary layer mixing processes: insights from dye experiments. *J. Phys. Oceanogr.*, **37**, 1859–1877.

Chatwin, P. C. (1976). Some remarks on the maintenance of the salinity distribution in estuaries. *Estuar. Coast. Mar. Sci.*, **4**, 555–566.

Chen, S. N., Geyer, W. R., Ralston, D. K., and Lerczak, J. A. (2012). Estuarine exchange flow quantified with isohaline coordinates: Contrasting long and short estuaries. *J. Phys. Oceanogr.*, **42**, 748763.

Cheng, P., Wilson, R. E., Chant, R. J., Fugate, D. C., and Flood, R. G. (2009). Modeling influence of stratification on lateral circulation in a stratified estuary. *J. Phys. Oceanogr.*, **39**, 2324–2337.

Conomos, T. J. (1979). Properties and circulation of san francisco bay waters. Technical Report ISBN 0-934394-01-6, Pacific Division of the American Association for the Advancement of Science c/o California Academy of Sciences Golden Gate Park San Francisco, California 94118.

Cook, T. L., Sommerfield, C. K., and Wong, K. C. (2007). Observations of tidal and springtime sediment transport in the upper delaware estuary. *Estuar. Coast. Shelf Sci.*, **72**, 235–246.

Day, J. W., Rybczyk, J., Scarton, F., Rismondo, A., Are, D., and Cecconi, G. (1999). Soil accretionary dynamics, sea-level rise and the survival of wetlands in venice lagoon: A field and modelling approach. *Estuarine, Coastal and Shelf Science*, **49**(5), 607 – 628.

de Boer, G. J., Pietrzak, J. D., and Winterwerp, J. C. (2008). Using the potential energy anomaly equation to investigate tidal straining and advection of stratification in a region of freshwater influence. *Ocean Model.*, **22**, 1–11.

Deegan, L. A., Johnson, D. S., Warren, R. S., Peterson, B. J., Fleeger, J. W., Fagherazzi,

S., and Wollheim, W. M. (2012). Coastal eutrophication as a driver of salt marsh loss. *Nature*, **490**(7420), 388 – 392.

Fisher, H. B. (1972). Axial convergence in a well-mixed estuary. *Journal of fluid Mechanics*, **53**(4), 671 – 687.

Fisher, H. B., List, E. J., Koh, R. C. Y., Imberger, J., and Brooks, N. H. (1979). *Mixing in Inland and Coastal Waters*. New York Academy.

Galperin, B. and Mellor, G. L. (1990). Salinity intrusion and residual circulation in delaware bay during the drought of 1984. *Estuar. Coast. Shelf Sci.*, **38**, 469–480.

Garvine, R. W., McCarthy, R. K., and Wong, K. C. (1992). The axial salinity distribution in the delaware estuary and its weak response to river discharge. *Estuar. Coast. Shelf Scis.*, **35**, 157–165.

Geyer, W. R., Trowbridge, J. H., and Bowen, M. M. (2000). The dynamics of partially mixed estuaries. *J. Phys. Oceanogr.*, **30**, 2035–2048.

Hansen, D. V. and Rattray, M. (1965). Gravitational circulation in straits and estuaries. *J. Mar. Res.*, **23**, 104–122.

Hansen, D. V. and Rattray, M. (1966). New dimensions in estuary classification. *Limnol. Oceanogr.*, **3**, 319–326.

Hofmann, E., Bushek, D., Ford, S., Guo, X., Haidvogel, D., Hedgecock, D., Klinck, J., Milbury, C., Narvaez, D., Powell, E., Wang, Y., Wang, Z., Wilkin, J., and Zhang, L. (2009). Understanding how disease and environment combine to structure resistance in estuarine bivalve populations. *Oceanography*, **22(12)**, 212–231.

Jay, D. A. and Smith, J. D. (1990). Circulation, density distribution and neap-spring transitions in the columbia river estuary. *Prog. Oceanogr.*, **25**(14), 81 – 112.

Lacy, J., Stacey, M., Burau, J., and Monismith, S. (2003). Interaction of lateral baroclinic forcing and turbulance in an estuary. *J. Geophys. Res.*, **108 (C3)**, 34,1– 34,15.

Lerczak, J. A. and Geyer, W. R. (2004). Modeling the lateral circulation in straight, stratified estuaries. *J. Phys. Oceanogr.*, **34**, 1410.

Lerczak, J. A., Geyer, W. R., and Chant, R. J. (2006). Mechanisms driving the time dependent salt flux in a partially stratified estuary. *J. Phys. Oceanogr.*, **36**, 2296–2311.

MacCready, P. (1999). Estuarine adjustment to changes in river flow and tidal mixing. *J. Phys. Oceanogr.*, **29**, 708–726.

MacCready, P. (2004). Toward a unified theory of tidally-averaged estuarine salinity structure. *Estuaries*, **27, No 4**, 561–570.

MacCready, P. (2007). Estuarine adjustment. *J. Phys. Oceanogr.*, **37**, 2133–2145.

MacCready, P. (2011). Calculating estuarine exchange flow using isohaline coordinates. *J. Phys. Oceanogr.*, **41**, 1116–1124.

MacCready, P. and Geyer, W. R. (2010). Advances in estuarine physics. *Annu. Re. Marine Sci.*, **2**, 35–58.

McCarthy, R. K. (1991). *A two-dimensional analytical model of density-driven residual currents in tidally dominated, well-mixed estuaries.* Ph.D. thesis, University of Delaware.

Monismith, S. G., Kimmerer, W., Burau, J. R., and Stecey, M. T. (2002). Structure and flow-induced variability of subtidal salinity field in northern san francisco bay. *J. Phys. Oceanogr.*, **32**, 3003.

Mukai, A. Y., Westerink, J. J., Luettich, J., and Mark, D. (2002). *Eastcoast 2001, A Tidal Constituent Database for Western North Atlantic, Gulf of Mexico, and Caribbean Sea*. US Army Corp of engineers.

Nepf, H. M. and Geyer, W. R. (1996). Intratidal variations in stratification and mixing in the hudson estuary. *J. Geophys. Res.*, **101**(C5), 12,079–12,086.

Niles, L., Burger, J., and Dey, A. (2012). *Life Along the Delaware Bay*. Rutgers University Press.

Nunes, R. and Simpson, J. (1985). Axial convergence in a well-mixed estuary. *Estuarine, Coastal and Shelf Science*, **20**(5), 637 – 649.

Oey, L. Y. (1984). On steady salinity distribution and circulation in partially mixed and well mixed estuaries. *J. Phys. Oceanogr.*, **14**, 629–645.

Okubo, A. (1973). Effects of shoreline irregularities on streamwise dispersion in estuaries and other embayments. *Netherlands Journal of Sea Reasearch*, **6**(1), 213–224.

Paulson, R. W. (1970). Variations of the longitudinal dispersion coefficient in the delaware river estuary as a function of fresh water inflow. *Water Resour. Res.*, **6, No. 2**, 516.

Pringle, A. W. and Phillips, N. (1989). The history of dredging in cleveland bay, queensland and its effect on sediment movement and on the growth of mangroves, corals and seagrass. Technical report, Great Barrier Reef Marine Park Authority.

Pritchard, D. W. (1952). Estuarine hydrography. *Adv. Geophys.*, **1**, 243–280.

Pritchard, D. W. (1954). A study of the salt balance in a coastal plain estuary. *J. Mar. Res.*, **13**, 133–144.

Pritchard, D. W. (1956). The dynamic structure of a coastal plain estuary. *J. Mar. Res.*, **1**, 243–280.

Ralston, D. K., Geyer, W. R., and Lerczak, J. A. (2008). Subtidal salinity and velocity in the hudson river estuary: observations and modeling. *J. Phys. Oceanogr.*, **38**, 753–770.

Reed, D. J. (1995). The response of coastal marshes to sea-level rise: Survival or submergence? *Earth Surface Processes and Landforms*, **20**(1), 39–48.

Rippeth, T. P., Fisher, N. R., and Simpson, J. H. (2001). The cycle of turbulent dissipation in the presence of tidal straining. *J. Phys. Oceanogr.*, **31**, 2458–2471.

Scully, M. E. and Geyer, W. R. (2012). The role of advection, straining, and mixing on the tidal variability of estuarine stratification. *J. Phys. Oceanogr.*, **42**, 855–868.

Scully, M. E., Geyer, W. R., and Lerczak, J. A. (2009a). The influence of lateral advection on the residual circulation: a numerical study of the hudson river estuary. *J. Phys. Oceanogr.*, **39**, 107–124.

Scully, M. E., Geyer, W. R., and Lerczak, J. A. (2009b). The influence of lateral advection on the residual estuarine circulation: A numerical modeling study of the hudson river estuary. *J. Phys. Oceanogr.*, **39**(1), 107–124.

Sharple, J. and Simpson, J. (1995). Semi-diurnal and longer period stability cycles in the liverpool bay region of freshwater influence. *Cont. Shelf Res.*, **15, No. 2/3**, 295–313.

Sharples, J., Simpson, J. H., and Brubaker, J. M. (1994). Observations and modelling of periodic stratification in the upper york river estuary, virginia. *Estuar. Coast. Shelf Sci.*, **38**(3), 301 – 312.

Shchepetkin, A. F. and McWilliams, J. (2009). Computational kernel algorithms for fine-scale, multiprocess, longtime oceanic simulations. *Computational Methods for the Atmosphere and the Oceans*, **14**, 121–183.

Simpson, J. (1981). The shelf-sea fronts: implications of their existence and behaviour. *Philos. T. R. Soc. Lond. Series A*, **302**, 531– 546.

Simpson, J. and Bowers, D. (1981). Models of stratification and frontal movement in shelf seas. *Deep-Sea Res.*, **28**(7), 727 – 738.

Simpson, J. and Hunter, J. (1974). Fronts in the irish sea. *Nature*, **250 (August)**, 404 – 406.

Simpson, J. and Hunter, J. (1978). Fronts on the continental shelf. *J. Geophys. Res.*, **83 (C9)**, 4607–4614.

Simpson, J., Brown, J., Matthews, J., and Allen, G. (1990). Tidal straining, density currents and stirring in the control of estuarine stratification. *Estuaries*, **13, No. 2**, 125–132.

Simpson, J. H. and Souza, A. J. (1995). Semidiurnal switching of stratification in the region of freshwater influence of the rhine. *J. Geophys. Res.*, **100**(C4), 7037 – 7044.

Sommerfield, C. K. and Wong, K.-C. (2011). Mechanisms of sediment flux and turbidity maintenance in the delaware estuary. *J. Geophys. Res.-Oceans*, **116**(C1).

Souza, A. and Simpson, J. (1996). The modification of tidal ellipses by stratification in the rhine rofi. *Cont. Shelf Res.*, **16**(8), 997 – 1007.

Souza, A. J. and Simpson, J. H. (1995). A two-dimensional (x-z) model of tidal straining in the rhine rofi. *Cont. Shelf Res.*, **16**(7), 949 – 966.

Stacey, M. T., Monismith, S. G., and Burau, J. R. (1999). Observations of turbulence in a partially stratified estuary. *J. Phys. Oceanogr.*, **29**(8), 1950–1970.

Stommel, H. and Farmer, H. G. (1952). On the nature of estuarine circulation: part i (chapter 3 and 4). Technical report, Woods Hole Oceanographic Institute.

USACE (1974). The district. a history of the philadelphia district. http://140.194.76.129/publications/misc/un16/c-15.pdf.

USGS (2012). Delaware river at trenton nj.

van Wijnen, H. and Bakker, J. (2001). Long-term surface elevation change in salt marshes: a prediction of marsh response to future sea-level rise. *Estuarine, Coastal and Shelf Science*, **52**(3), 381 – 390.

Warner, J., Sherwood, C., Arango, H., and Signell, R. (2005). Performance of four turbulence closure models implemented using a generic length scale method. *Ocean Modelling*, **8**, 81–113.

Whitney, M. M. and Garvine, R. W. (2006). Simulating the delaware bay buoyant flow: Comparison with observations. *J. Phys. Oceanogr.*, **36**, 3–21.

Wong, K. C. (1995). On the relation between long-term salinity variations and river discharge in the middle reach of delaware bay. *J. Geohys. Res.*, **100, No. C10**, 20,705–20,713.

Wong, K. C. and Moses-Hall, J. E. (1998). The tidal and subtidal variations in the transverse salinity and current distribution across a coastal plain estuary. *J. Mar. Res.*, **56**, 489–517.

Wong, K. W. (1994). On the nature of transverse variability in a coastal plain estuary. *J. Geohys. Res.*, **99, No. C7**, 14,209–14,222.

Zahed, F., Etemad-Shahidi, A., and Jabbari, E. (2008). Modeling of salinity intrusion under different hydrological conditions in the arvand river estuary. *Can. J. Civil Eng.*, **35**, 1476–1480.

Zimmerman, J. (1986). The tidal whirlpool: a review of horizontal dispersion by tidal and residual currents. *Neth. J. Sea Res.*, **20 (2/3)**, 133–154.